Myelination diseases of the central nervous system: Artificial Axons as in vitro models of chemomechanical cues

By

Mingyu Yang

Bachelor of Science
Materials Science and Engineering; Cognitive Science
Johns Hopkins University, 2019

Submitted to the Harvard-MIT Program in Health Sciences and Technology in partial fulfillment of the requirements for the degree of

Doctor of Philosophy in Medical Engineering & Medical Physics
at the

MASSACHUSETTS INSTITUTE OF TECHNOLOGY
May 2024

Authored by: Mingyu Yang
Harvard-MIT Program in Health Sciences and Technology
May 16, 2024

Certified by: Krystyn J. Van Vliet, PhD
Vice President of Research and Innovation, Professor, Cornell University
Thesis Supervisor

Accepted by: Collin M. Stultz, PhD
Director, Harvard-MIT Program in Health Sciences and Technology
Nina T. and Robert H. Rubin Professor in Medical Engineering and Science
Professor of Electrical Engineering and Computer Science

Myelination diseases of the central nervous system: Artificial Axons as in vitro models of chemomechanical cues

By

Mingyu Yang

Submitted to Harvard-MIT Health Sciences and Technology in
partial fulfillment of the requirements for the degree of
Doctor of Philosophy in Medical Engineering & Medical Physics

Abstract

Myelination is a key biological process wherein glial cells such as oligodendrocytes wrap myelin around neuronal axons, forming an insulative sheath that accelerates signal propagation down the axon. A major obstacle to understanding myelination is the challenge of visualizing and reproducibly quantifying this inherently three-dimensional process *in vitro*. To this end, Van Vliet et al. previously developed Artificial Axons (AAs), a biocompatible platform consisting of 3D-printed axon mimics that can be ensheathed by oligodendrocytes *in vitro*. In this thesis, we advance and apply the Artificial Axon platform to create *in vitro* models of lesion-like environments to elucidate the mechanisms underlying myelination diseases.

First, we improve the existing AA platform to investigate how biophysical cues affect myelin wrapping by rat oligodendrocytes. We build a new high-resolution 3D printer (HR-3DP) that can fabricate AAs with sub-kilopascal elastic moduli and <2 μm diameters. These properties are clinically relevant as prior neuroimaging data from human patients show correlations between demyelinating diseases and changes in brain stiffness, axon diameter, and axon density. An open question is whether these biophysical changes simply act as correlative biomarkers or contribute directly to disease progression. We demonstrate that the extent of myelin ensheathment by rat oligodendrocytes is sensitive to the Young' modulus, diameter, and density of axons, indicating that each of these biophysical cues may play a causal role in influencing an oligodendrocyte's propensity to myelinate. We further

demonstrate that the responses of oligodendrocytes to pro-myelinating compounds are dependent on axon stiffness, and that the relative ranking of drug efficacies differs between stiff and compliant axons. These results reinforce the importance of studying myelination in mechanically representative environments, and highlight the importance of considering biophysical cues when conducting drug screening studies for pro-myelinating compounds.

Second, we demonstrate the promise of using AAs to model lesion-like environments using human oligodendrocytes. For example, multiple sclerosis (MS) is a demyelinating disease affecting over one million adults in the United States, characterized by the destruction of myelin through a range of immune-mediated mechanisms. The accumulation of myelin debris and inflammatory cytokines in the brains of MS patients is thought to contribute to a growth-inhibitory environment that impairs myelin repair. We used AAs to model the impact of myelin debris and microglia co-culture on myelin ensheathment, recapitulating *in vivo* results demonstrating a dose-dependent effect of myelin debris on myelin ensheathment. We further demonstrate the compatibility of the AAs with myelination by human oligodendrocytes derived from induced pluripotent stem cells (iPSCs). In particular, we explore the effect of the apolipoprotein (ApoE) genotype on myelin ensheathment, based on clinical data that individuals with the ApoE4 allele exhibit worsened MS prognosis compared to individuals with the ApoE3 allele. Finally, we demonstrate how targeted perturbations to cholesterol metabolism pathways differentially impact ApoE3 vs. ApoE4 human oligodendrocytes. In sum, these results demonstrate the potential of AAs to elucidate the cellular and molecular mechanisms of myelination in the context of human disease.

Thesis Supervisor: Krystyn J. Van Vliet
Thesis Co-Advisor: Aristide Gumyusenge
Thesis Committee Member: Kristin Galetta
Thesis Committee Chair: Darrell J. Irvine

Dedicated to my grandparents, 爷爷 *and* 奶奶

Acknowledgements

I am firstly grateful to my advisor Krystyn Van Vliet, who has fostered a wonderfully warm and nurturing group environment. I would frequently walk into Krystyn's office dismayed that yet another experiment had "failed", and Krystyn would always see the positives, helping me to decouple my scientific disappointment from any feelings of personal failure. Krystyn is also a fantastic communicator, and I have most enjoyed the meetings where we sit down for an hour to edit a paper together in real-time. I am also grateful to the members of my thesis committee, Aristide Gumyusenge, Darrell Irvine, and Kristin Galetta, each of whom has been a constant source of support and advocacy. When the lab moved, they frequently checked in on me to make sure I had a plan, offering their time and resources to keep me on track.

My labmates are simply wonderful. I couldn't have asked for a better friend, mentor, and scientific partner than Anna. Being in the lab together with Anna reminds me that research can be intensely *fun*, and we have always managed to find laughter out of our collective misfortune. Brandon has been a great source of both support and scientific scrutiny, and Cammie has helped me get through many a long night at the AFM, sitting with me as I slowly worked up the confidence to go at it alone. I will also miss working with our undergraduate researchers, Nia, Zheyao, and Calliope, and I feel truly proud to see the ways they've each flourished since moving on from the group. I've also benefited from great collaborators, in particular Kavin Kowsari, with whom I spent many weekends troubleshooting the HR-3DP, and the Tsai Lab, including Joel Blanchard, William Ralvenius, and Emre Agbas, for making Chapter 4 of this thesis possible. Finally, I am grateful to Daniela, who laid the foundations of my thesis, and to Alex, the lab elder statesman-turned-unexpected officemate.

In addition to my growth as a researcher, I've grown a great deal as a teacher. The team at MITxBio (Mary Ellen, Darcy, Caitlin, Moni) took me in during my first semester of grad

school (before I joined my actual research group!) and they've been a second academic family for me ever since. I've loved my time working with the team at CBI, especially Paul, Flora, and Betsy; I came for the fantastic people, and I stayed for the copious ice-cream they'd feed me every time I visited the office. I'm also thankful for Rohan from MIT's Office of Government and Community Relations, who has opened up uncountably many doors for me to do science outreach all around Cambridge (*everybody* knows Rohan). I leave every conversation with Rohan with a literal spring in my step, feeling excited to create ever bolder and wackier projects. Among those, a real highlight was cooking up science shows with the Kitchen Matters team (Cammie, Miranda, Jackie, Tao, Jessica, and unofficially but just as importantly, Allison and Kevin). Towards the end of grad school, I was fortunate to attend SABER and meet a delightful community of biology education researchers, including Crystal, Zack, Dina, Kate, and Bryan, all of whom set me on my current path.

I will also hold fond memories of teaching 3.091, together with a team of truly devoted and caring instructors. My students were kind, hardworking, and silly; my excitement to spend the afternoon with them was what powered me through many failed experiments in lab. Laura has the thankless task of keeping this 400-person train from veering off the rails, and she does so with great compassion, all the while acting as a fierce advocate for me and my fellow TAs. Finally, I am grateful for all the formal and informal teaching opportunities I had before grad school, in particular at Hopkins and through the MERIT Health Leadership Academy in Baltimore. It was at Hopkins where I first discovered that you could be a teaching-focused professor, and I am particularly indebted to Orla Wilson and Linda Gorman who paved this path for me to follow. Early on in grad school, I was embarrassed to admit that I'd come to MIT with aspirations of a teaching-focused career; but meeting people like the MITxBio team, like Kirk Kolenbrander, Orla, and Linda, has been so deeply validating. After graduating I will start a teaching professor position, and I feel truly, unreservedly proud to be able to say that.

I love my friends. I was lucky to join grad school with a truly brilliant cohort of HST classmates. I'm so grateful that we got to share this journey together, and I will always cherish those memories of commuting to Harvard Med and huddling together to do a crossword before class. I'm also lucky to have found an unofficial cohort through DMSE, where my friends have unlocked new sides of me (like *Party Ming* and relatedly, *Sleepy Margarita Ming*) of which I was previously unaware. I'm especially grateful for Alex Kossak and his extended family for offering me a place to stay during COVID, and in general, becoming an adoptive family for me over the past five years. I've stayed at his family home at least five times now, and I've probably broken twice as many glasses when I was there. Thank you for being a second family for me when I couldn't go home to see my own. Finally, this thesis is incomplete without acknowledging my housemates, Pablo and Kirby. I've had many low points in grad school, but each time, knowing that I'd come home to Kirby and Pablo has made every day worth it.

Above all, my family has been the bedrock of my entire life experience. I had a truly happy upbringing with two wonderfully supportive parents and brothers who nurtured my interests and put me onto this path. I am also especially grateful to my paternal grandparents, who were my primary guardians for the first few years of my life. They sadly didn't get the chance to see me finish grad school, but I know they would be proud no matter where I was and what I found myself doing. This thesis is dedicated to you, 爷爷 and 奶奶.

Table of Contents

1. Introduction

This thesis focuses on the role of biophysical cues on myelination, to better understand how myelination occurs developmentally, but also how this process becomes dysregulated in the context of disease. To lay the groundwork for those questions, this introduction defines myelination, demyelination, and dysmyelination, providing the biological framework for these questions.

1.1 Myelination, demyelination, and dysmyelination

Myelin is critical for the homeostatic function of mammalian nervous systems. Myelin is a lipid-rich material that ensheaths neuronal axons, forming a characteristic multilaminar structure consisting of concentric layers of fatty membrane[1] (**Figure 1A**). Myelin minimizes ion leakage across the axonal membrane, thereby accelerating the speed of electrical signal conduction along the axon[2,3]. The composition of myelin is approximately 70-80% lipids, and 20-30% proteins that contribute to myelin extrusion and compaction[2]. Myelinated axons contain periodic breaks in the myelin structure, termed the nodes of Ranvier, which allow ion flow and regeneration of the action potential (termed saltatory conduction). The destruction of myelin or the inability to form myelin during development can lead to reduced speeds of signal transmission within neurons, in turn giving rise to systemic nervous system deficits.

Oligodendrocytes (OLs) produce myelin in the central nervous system (CNS) and are fundamental to CNS development and myelin regeneration following injury[4,5]. Every oligodendrocyte sends out multiple cellular processes, each of which envelops a single segment of axon. These processes are direct extensions of the oligodendrocytes' plasma membrane, forming a spiral-like wrapping around the axon that eventually compacts into multilaminar myelin (**Figure 1B**).

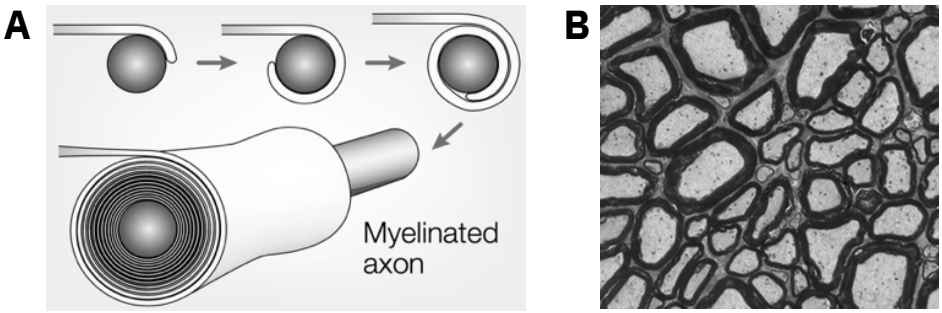

Figure 1 (A) Schematic of a single oligodendrocyte process ensheathing an axon[6], from Franklin (2002) (B) Transmission electron micrograph of multilaminar myelin structure[7], from Duncan and Radcliff (2016).

During development, oligodendrocytes derive from oligodendrocyte progenitor cells (OPCs)[1,8]. OPCs in turn derived from neuroepithelial cells, also termed neural stem cells (NSCs)[3]. In development, OPCs arise in characteristic temporal waves predominantly within the subventricular zone and the dorsal spinal cord[9,10]. OPCs subsequently migrate to developing axon tracts and differentiate into mature oligodendrocytes, a process guided by mitogens such as platelet derived growth factor (PDGF) in addition to developmental signaling pathways such as Wnt signaling[8]. Uniquely among neural stem cells, a large fraction of OPCs also stays undifferentiated and are maintained into adulthood in their progenitor state[11]. Adult OPCs retain the ability to differentiate into oligodendrocytes (OCs), in doing so playing a critical role in the nervous system's response to demyelinating diseases[12]. In the adult brain, OPCs have a stable proliferation rate to maintain a steady state homeostatic cell density[13]. Animal studies have shown that disrupting this baseline OPC turnover can have behavioral implications; in one study, inhibiting the formation of new adult oligodendrocytes in mice (without affecting any existing oligodendrocytes or structurally altering any existing myelin) prevented mice from learning new motor skills[14]. Although the precise mechanisms are unclear, it is now well established that the steady maintenance of OPCs in the adult brain plays a key role in homeostatic function.

At each stage of oligodendrocyte development and maturation, NPCs, OPCs, pre-OCs, and OCs are characterized by distinct developmental markers[8]. shown in **Figure 2**. OPCs

express DM-20, which is an isoform of proteolipid protein (PLP), in addition to PDGFR-α, the receptor for PDGF. As OPCs commit to the oligodendrocyte lineage, they start expressing linage-specific markers such as O4, in addition to proteins that form a structural component of myelin, including proteolipid protein (PLP) and myelin basic protein (MBP). In my thesis, we leverage commercially available antibodies against these markers to assay for different stages of OPC differentiation.

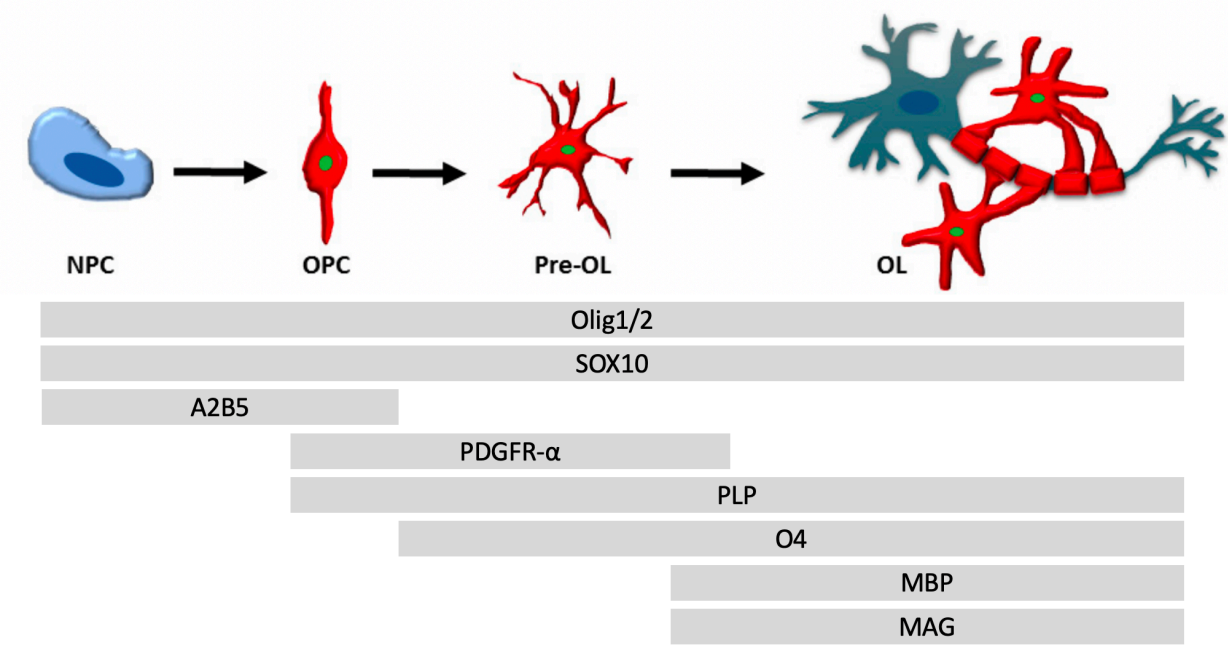

Figure 2 Oligodendrocyte lineage markers for different developmental stages. Each lineage marker is a protein that could be used as a target for immunohistochemistry. Olig1/2 and SOX10 are expressed in all cells in the neural progenitor cell (NPC) lineage. Adapted from Kuhn et al. (2019)

Oligodendrocytes belong to a broader family of cells called glial cells, which comprises all the non-neuronal cells in the central and peripheral nervous system[15]. Among them, Schwann cells are the principal myelinating cells of the peripheral nervous system[16]. Unlike oligodendrocytes, which can each ensheath multiple axons, each Schwann cell myelinates just a single axon. Other differences also exist in the myelin produced by Schwann cells; for example, the nodes of Ranvier in the peripheral nervous system are covered by the Schwann cell processes, whereas in the CNS, nodes of Ranvier are devoid of oligodendrocyte processes. Furthermore, the developmental signals that cause Schwann cell differentiation and migration are distinct from those that drive

oligodendrocyte formation. Although Schwann cells play a critical role in developmental myelination, they are outside the scope of this thesis. A separate population of glial cells are astrocytes, which have wide-ranging functions including the maintenance of the blood-brain barrier, regulation of extracellular potassium levels (critical for maintaining a neuron's appropriate resting membrane potential), in addition to playing key roles in neuronal signaling (including formation of 'tripartite synapses' with neurons)[17]. Finally, a third class of glia are microglial cells, the resident immune cells of the brain that contribute to responses following infection and injury, including phagocytosis of apoptotic debris[18].

The interaction between different types of glial cells, in addition to glial-neural interactions, are key to nervous system homeostasis and pathology. For example, microglia can secrete cues that recruit OPCs to sites of tissue injury[19]. Furthermore, astrocytes secrete soluble factors that can both promote and inhibit OPC differentiation and myelination. Astrocytes are critical for OPC survival and provide trophic support that maintain myelin integrity[20], however the polarization of astrocytes to an inflammatory phenotype can lead to myelin loss. In one study, OPCs were cultured in astrocyte-conditioned media (media collected from previously culturing astrocytes); when astrocytes were first activated into a reactive phenotype, they secreted inflammatory factors into the media, which in turn decreased myelin production by OPCs[21]. In sum, the three-way crosstalk between oligodendrocytes, astrocytes, and microglia can play both beneficial roles in CNS maintenance and repair in addition to detrimental roles in CNS injury.

Diseases that damage myelin or lead to the incomplete formation of myelin during development can have wide-ranging neurological effects. Myelin disorders can be broadly classified as dysmyelinating or demyelinating diseases. In dysmyelination, the myelin sheath fails to form properly during development. Dysmyelinating diseases, also termed hypomyelinating leukodystrophies, are often genetically inherited disorders that affect lipid metabolism pathways that ordinarily enable myelin synthesis[7,22–24]. Surprisingly, only a small number of leukodystrophies are caused by genes encoding

structural proteins that make up myelin; instead, many more mutations affect proteins that mediate lipid transport and synthesis[23]. Most patients present with leukodystrophies in infancy or early childhood, and genetic sequencing can provide a definitive diagnosis in 80-90% of cases.

One example of a hypomyelinating leukodystrophy is X-linked adrenoleukodystrophy (X-ALD), which is caused by mutations in the *ABCD1* gene. The *ABCD1* gene encodes the adrenoleukodystrophy protein (ALDP)[25]. ALDP is localized to the peroxisome membrane and transports very long chain fatty acids (VLCFAs) into the peroxisome lumen for degradation. Consequently, VLCFAs accumulate within cells, which is thought to lead to mitochondrial dysfunction and oxidative damage that causes oligodendrocyte apoptosis during development[26]. Since leukodystrophies are caused by germline mutations, other cell types beyond oligodendrocytes are affected as well. For example, the accumulation of VLCFAs in astrocytes was found to promote a more inflammatory astrocytic phenotype that led to myelin degradation[27]. An interesting aspect of X-ALD is that VLCFAs are actually a normal structural component to myelin, imparting rigidity to the myelin membrane and reinforcing the ion permeability barrier that is essential to myelin's insulative function[24,28]. The mechanism by which X-ALD drives hypomyelination indicates that there is a dose-dependence to how much VLCFAs a healthy oligodendrocyte can tolerate; a baseline amount of VLCFAs is required for myelin production, but too much can lead to oxidative stress and cell death.

More broadly, lipotoxicity is a general mechanism shared across many myelination diseases, where the accumulation of lipids or their metabolic precursors can reach levels that are toxic to oligodendrocytes. For example, the leukodystrophies cerebrotendinous xanthomatosis (CTX) and Tangier disease (TD) are both caused by accumulation of cholesterol precursors[24]. Similarly, another subclass of leukodystrophies involves the pathological accumulation of glycosphingolipids, a class of glycolipids found broadly in cell membranes and also in myelin, which leads to cytotoxicity to oligodendrocytes. Krabbe disease is caused by a mutation to the gene encoding the enzyme galactocerebroside β-galactosidase, which leads to the cytotoxic accumulation of

the lipid galactosylsphingosin[29–31]. Metachromatic leukodystrophy (MLD) is caused by a mutation in the gene encoding the enzyme arylsulfatase A (ARSA), which also leads to the accumulation of galactosylceramide-3-O- sulfate (sulfatide) in cells. These examples speak to the broader point that excess accumulation of lipids, including those that are normal constituents of healthy myelin, can lead to cytotoxicity, oligodendrocyte death, and developmental hypomyelination.

In contrast to dysmyelinating diseases, *de*myelinating diseases are characterized by the destruction of myelin that formed normally during development[32]. The most common demyelinating disease is multiple sclerosis (MS), which affects over one million adults in the United States[33]. The clinical manifestations of demyelinating diseases are highly heterogeneous, ranging from sensory loss to muscle weakness[23]. Multiple sclerosis is characterized by an inflammatory cascade wherein immune cells, including autoreactive T cells, B cells, and macrophages are recruited to the brain[34–36]. This leads to the destruction of myelin through a range of immune-mediated mechanisms, such as cytokine damage, oxidative injury and phagocytosis. In early stages of MS, patients typically present with relapse-remitting MS (RRMS), wherein periods of demyelination are followed by periods of remission. Disease severity may increase to a period of unremitting disease progression, called secondary progressive MS (SPMS). In some cases, patients progress directly to the progressive phase without any periods of remission, termed primary progressive MS (PPMS). The mechanisms underlying this heterogeneity in both patient presentation and progression still remain unclear.

Whereas there is a clear genetic cause to most hypomyelinating leukodystrophies, multiple sclerosis is a more complex, multifactorial disease. Although genetics are not the singular causal factor, MS does have a genetic component; for example, the risk of developing MS is increased between 100 and 190-fold if an identical twin also has the disease[32,37]. One genetic locus of interest is the gene encoding apolipoprotein (ApoE), which is involved in lipid transport and membrane repair. There are three isoforms of the ApoE protein, designated ApoE2, ApoE3, and ApoE4. Most healthy individuals express the ApoE3 isoform, however expression of ApoE4 is correlated with worsened

prognosis in MS patients[38]. An open question is whether there is in fact a causal relationship between the ApoE isoform expressed and the myelinating potential of oligodendrocytes. Interestingly, the *ApoE* gene also correlates with risk for Alzheimer's disease, where patients expressing the ApoE4 isoform carrying a greater risk for developing Alzheimer's disease compared to those with the ApoE3 isoform[39]. Although the connection between Alzheimer's disease and myelination is not well-studied, there is increasing interest in the potential role of demyelination in the pathogenesis of neurodegenerative diseases, including Alzheimer's disease. Non-heritable factors also play a key role in multiple sclerosis. A recent landmark study showed that there was a strong link between MS risk and prior environmental exposure to Epstein-Barr virus (EBV). In particular, a longitudinal epidemiological study showed that MS risk increased 30-fold following EBV infection[40]. One hypothesis is that the high antibody titer against EBV antigens leads to a concomitant increase in the risk for autoimmune attack found in MS.

Another underexplored area of myelination disease pathology is how the brain's mechanical properties change over the course of disease progression. Neuroimaging data from human patients show correlations between progressive MS and changes in the structural integrity and mechanical properties of brain tissue[41,42]. These findings are supported by murine models of demyelination, in which the Young's modulus *E* of brain parenchyma decreased in response to acute demyelination from 240 Pa to 120 Pa, signifying a stiffness reduction correlated with disease progression[43,44].

A growing body of evidence demonstrates that oligodendrocytes and OPCs are sensitive to external mechanical cues[45] including ECM stiffness (and more broadly the stiffness of the material to which OPCs adhere)[46–50], mechanical strain[51], macromolecular crowding, and physical confinement[52,53]. Therefore, an open question is whether these changes in brain parenchyma stiffness occur a secondary byproducts of myelination pathology, or whether they could play a causal role in changing the propensity of oligodendrocytes to myelinate, in turn affecting disease progression. For example, if stiffening brain parenchyma causes oligodendrocytes to myelinate less readily, could this

explain the failure to remyelinate and recover from injury? More broadly, these examples highlight that there is still much that is unknown about MS, highlighted by the absence of cures for any demyelinating diseases. There is a wide body of literature exploring many different mechanical cues (Young's elastic modulus, storage modulus, loss modulus), although in this thesis we will constrain our scope to how the Young's modulus of axons influences myelination.

The absence of any curative drugs for demyelination is due in part because the biological mechanisms that underlie myelination are still poorly understood[6]. Most available treatments for MS are disease-modifying drugs that can reduce or halt the autoimmune symptoms of the disease, but fail to reverse the potential long-term degeneration caused by myelin loss[54,55]. One promising strategy for discovering effective therapies and studying myelination mechanisms is to develop better tools to recapitulate this three-dimensional process *in vitro*.

1.2 *In vitro* models of myelination

To overcome the challenges of probing oligodendrocyte function *in vivo*, a wide range of *in vitro* models have been developed to recapitulate myelination using mammalian cells and tissues. The earliest *in vitro* models were dissociated CNS cultures, in which segments of spinal cord tissue were removed and dissociated by proteolysis[56]. Although these systems are relatively faithful recreations of the cell-cell interactions *in vivo*, they typically have low viability, inconsistent yield, and poor reproducibility between donors[57]. Furthermore, such models fail to recapitulate the full three-dimensional geometry of brain tissue. Another approach to *in vitro* modeling is to use slice cultures, where full tissue slices of rodent brain or spinal cord are cultured on a biocompatible substrate. In one study from the 1950s, researchers cultured brain slices from newborn rat and kitten cerebellum and demonstrated myelin formation over a 2-week period[58]. Although these slice cultures can recapitulate the 3D complexity of brain tissue and the complex intercellular crosstalk, it is difficult to isolate individual components of the system and establish causal relationships[57]. To better isolate

individual cell populations and the signaling events between them, oligodendrocyte-neuron co-culture systems have also been developed[59]. However, even these models have the potential for off-target signaling events that complicate the discovery of underlying mechanisms, in addition to challenges with obtaining and purifying cells that introduce further heterogeneity[57]. Furthermore, co-cultures have the same geometric constraint as dissociated cultures, wherein a flat 2D culture will fail to recapitulate the 3D complexity of brain tissue and of the myelination process. Instead, these 2D co-cultures typically measure myelination by using a more limited readout of quantifying myelin basic protein (MBP) production, which is a hallmark of differentiated myelinating oligodendrocytes (**Figure 2**).

More recent work has focused on using human cells to model myelination *in vitro*, in particular using human induced pluripotent stem cells (hiPSCs). hiPSCs are produced by treating adult human skin fibroblasts with a cocktail of transcription factors (Oct3/4, Sox2, Klf4, and c-Myc), which reprograms the fibroblasts into a pluripotent stem cell state[60]. Like the embryonic stem cells (ESCs) formed endogenously in development, these hiPSCs now have the potential to differentiate into any adult somatic cell type in the body. A variety of protocols have now been designed to drive hiPSCs to differentiate towards a neuronal/glial lineage[61,62], which also paves the way to creating brain disease models using patient-specific human cells[63]. In particular, Douvaras and Fossati developed a differentiation protocol that produces O4+ OPCs from a 75-day culture[62], which was shorter than all previously reported approaches. They validated the protocol across nine iPSC lines derived from different donors, finding that the efficiency of O4+ OPC production ranged from 28-80%.

hiPSCs have been used to create organoid models, which have been shown to exhibit similar gene expression profiles compared to neural and glial progenitor cells in the developing fetal brain[64]. In one study, researchers developed hiPSC-derived myelinating organoids, finding that OPCs differentiated into myelinating oligodendrocytes over a 60-day period[65]. Due to the technical challenges of differentiating hiPSCs into neural cells, very few organoid models of myelination have

been developed. Furthermore, although organoids can recapitulate full spatiotemporal signaling complexity of cells, it is difficult to isolate individual cell populations and tease apart causal relationships. iPSC-derived models also have significant batch-to-batch variability, both across different cell donors and also between separate differentiations of the same donor's cells[49]. Finally, visualizing and quantifying 3D myelination within an organoid context is challenging.

One promising avenue for *in vitro* myelination models is to develop axon-free systems. Taking this deliberately reductionist approach can enable a more tractable model, without the complex neuron-oligodendrocyte crosstalk that can make organoid models and slice cultures difficult to interpret. The simplest such model involves seeding purified OPCs directly on a tissue culture polystyrene (TCPS) plate and measuring myelin production in the absence of any neurons. In one study from the 1980s, monolayers of lamb oligodendrocytes synthesized membrane sheets that resembled myelin. Although these models are fairly reproducible, they lack biological fidelity and do not recapitulate the three dimensionality of myelination. More recently, groups have engineered axon-mimicking material that can be ensheathed by oligodendrocytes. The earliest such axon mimics were developed in 1990, consisting of glass microfibers with sub-micron diameters[66]. Transmission electron microscope (TEM) images showed that purified rat oligodendrocytes deposited myelin around the glass axon mimics, the first demonstration of its kind that dynamic axon signaling was not necessary for myelin wrapping. This observation was reinforced by subsequent studies where OPCs were seeded on axons fixed with paraformaldehyde – even though the axons were dead, just the physical presence of an axon-like structure was sufficient to induce myelin ensheathment by oligodendrocytes[52]. The study also found that OPCs *in vitro* must exceed a critical cell density before they differentiate into OCs and myelinate an axon-like structure. Increasing the density of seeded OPCs increased the extent of myelin wrapped; furthermore, adding inert polystyrene beads to the cell culture (while holding the number of OPCs constant) *also* increased the extent of myelin wrapping, suggesting that physical crowding is the driving factor for OPC differentiation in these systems.

Since the earliest glass models, many more engineered materials have been developed as synthetic axon mimics. Another common approach is to use electrospun polymer fibers[53,67,68], fabricated by extruding a thermoplastic polymer solution (commonly poly(ε-caprolactone) and poly(lactic acid)) through a needle at high voltages. The applied voltage causes the extruded polymer to deform into a fine jet stream; upon evaporation of the solvent, this process can generate solid polymer fibers with as low as nanoscale diameters[69]. One benefit to using electrospun fibers over glass microfibers is that the electrospun fiber diameter is easily adjustable through modification of the fabrication conditions, for example by adjusting the applied voltage or the gauge of the needle. In one study of electrospun fibers, researchers fabricated axon mimics of three diameter ranges: 0.5-1 μm, 1-2 μm, and 2-4 μm. When rat oligodendrocytes were seeded on these fibers, there was a direct relationship between the fiber diameter and the length of myelin sheaths produced by oligodendrocytes, indicating that cells are sensitive to axon diameter. In addition to diameter, the Young's elastic modulus of axons can be separately tuned. In a separate study using electrospun fibers, researchers varied the crystallinity of the poly(lactic acid) and poly(ε-caprolactone) material to modify the Young's elastic modulus of the solid fiber. This work showed that higher-crystallinity (and thus stiffer) fibers of the electrospun fiber led to a concomitant increase in the proportion of MBP+ oligodendrocytes depositing myelin around the fibers[67]. Although the tunability of electrospun fibers can offer significant advantages over glass formats, one limitation of electrospun fibers is that visualizing myelin wrapping is technically challenging. Studies using electrospun fibers typically quantify the proportion of MBP+ cells as a proxy for myelin wrapping, since the geometry of these fibers makes them difficult to image in three dimensions. Furthermore, even though electrospun fibers do recapitulate the sub-micron diameter of biological axons, their Young's modulus is typically in the kPa range, which is several orders of magnitude stiffer than brain tissue [53,67,68,70–72]. Since OPCs, like many other cell types, are mechanosensitive[46–50], the behavior of these cells on these stiff substrates may not necessarily be representative of their *in vivo* behavior. Therefore, an open question is still how the *3D* myelination by

oligodendrocytes responds to changes in diameter and stiffness *within the physiological range*.

To overcome the incompatibility of electrospun fibers with high-throughput imaging, researchers have also developed axon mimics from silica arrays, fabricated directly within multi-well plates[70]. The microarrays had a conical geometry, with a 50 μm-diameter base and a 2 μm-tip. After five days of culture, rat OPCs differentiated into oligodendrocytes that fully ensheathed the silica cones. This format of fabricating synthetic axon mimics within a multi-well plate is amenable to high-throughput imaging, which paves the way towards efficient drug screening for therapeutic discovery. Since electrospun fibers cannot be fabricated within multi-well plate formats, such high-throughput screening and imaging is not possible. Furthermore, the multi-well plate format is also amenable to 3D imaging via confocal microscopy, enabling visualization and quantification of myelin ensheathment instead of using proxy measures like MBP expression. However, like the electrospun fibers, a major weakness of these silica arrays is their high mechanical stiffness (on the order of gigapascals). Furthermore, the geometry and mechanical stiffness of silica cones are less tunable compared to electrospun polymers. Put together, these existing materials expose a gap in the material development space; our goal is to design a synthetic axon material that captures the tunability of electrospun fibers, is compatible with high-throughput imaging like the silica microarrays, and is also more mechanically compliant like biological tissue.

In summary, the design space of *in vitro* myelination models can be summarized by the trade-off between biological fidelity and reproducibility/scalability (**Figure 3**). Although organoid models and slice cultures have high biological fidelity, they are challenging to scale up, and reproducibility can be low because of heterogeneity in the cell population. Furthermore, having too much biological complexity can complicate interpretation of the results – if we observe elevated oligodendrocyte myelination compared to baseline, which feature of the model system was the driving causal factor? In contrast, seeding oligodendrocytes on TCPS plates represents the opposite end of the spectrum, with high technical scalability and reproducibility but extremely limited

biological fidelity. In our work, we seek to develop an *in vitro* axon-free model that can satisfy both criteria: high biological fidelity and also high reproducibility/technical scalability.

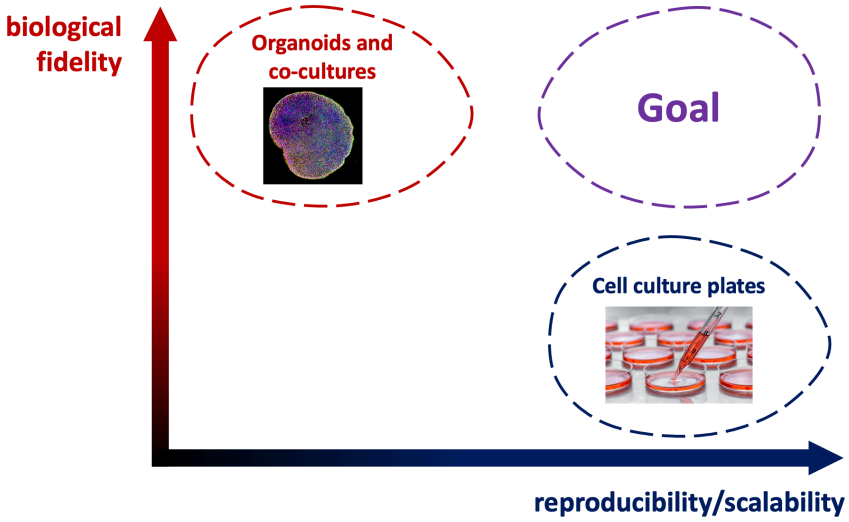

Figure 3 Trade-off between biological fidelity and reproducibility/scalability in the design of *in vitro* models of myelination

1.3 Prior work on Artificial Axons

Prior work in the Van Vliet Laboratory for Material Chemomechanics has developed Artificial Axons (AAs), which are 3D-printed hydrogel structures that mimic the sub-kilopascal stiffness and micrometer-scale diameter of biological axons[73–75]. Importantly, in this platform we can engineer properties of the axon arrays, such as stiffness, spacing, and diameter, enabling systematic studies of the influence of each cue on myelin wrapping.

Chapter 2 of this thesis focuses on the fabrication and characterization of Artificial Axons. In brief, we fabricate Artificial Axons using projection microstereolithography, a 3D-printing approach that uses UV light to polymerize micrometer-scale solid structures. Espinosa-Hoyos et al. previously developed a custom resin which is liquid when unpolymerized, but solidifies into a columnar geometry when exposed to UV light[73–75]. This enabled fabrication of AA arrays on individual 5 mm-diameter coverslips, illustrated by **Figure 4**. Each AA sample was then functionalized

with a surface ligand (typically laminin) to make the axons biocompatible for cell culture. Finally, each coverslip was placed in a separate well of a 96-well plate, and OPCs were seeded onto the AAs.

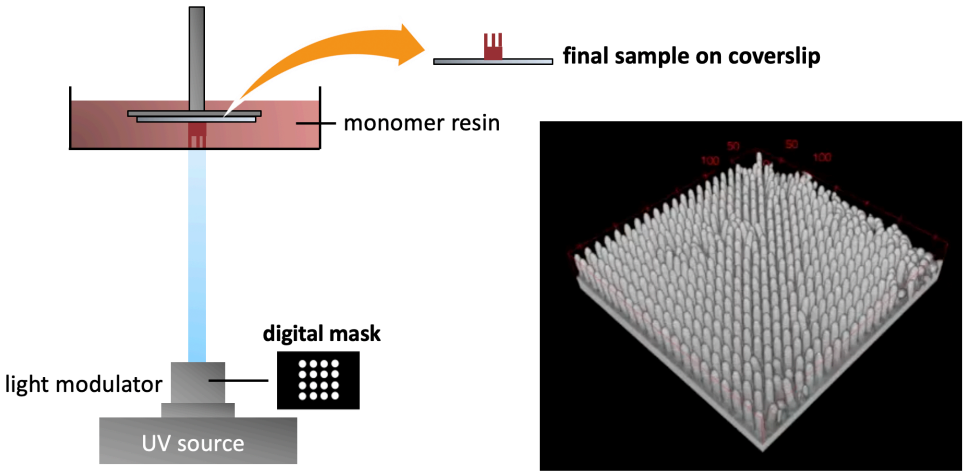

Figure 4 Schematic of set-up for fabricating Artificial Axons, previously reported by Espinosa-Hoyos et al. (2018). The scanning electron micrograph shows the 3D geometry of the axons; here, the axons have an average ~4 μm diameter.

Espinosa-Hoyos et al. previously demonstrated that AAs fabricated in this way were biocompatible with both rat primary OPCs and hiPSC-derived OPCs. Both rat and hiPSC-derived OPCs ensheathed myelin around the AAs after 7 days and ~48 days respectively, although the reproducibility of myelin wrapping by hiPSC-derived oligodendrocytes was low. We also developed an image analysis pipeline to quantify the 3D myelin ensheathment by oligodendrocytes along the length of the AA.

Previous work demonstrated that OPCs were sensitive to the Young's elastic modulus E, diameter, and surface coating of the AAs. For example, compared to AAs with E = 0.4 kPa, those with E = 140 kPa elicited a 2.5-fold increase in the number of AAs wrapped by oligodendrocytes. Furthermore, axons with diameters of 10 μm elicited a 2-fold increase in myelin wrapping by oligodendrocytes compared to those with 20 μm diameter. Finally, there was approximately a 3-fold increase in myelin when AAs were coated with laminin (a common ligand in oligodendrocyte biology) compared to poly-*d*-lysine (a non-specific cell adhesion molecule). These results speak to the promise of

having a tunable materials system for fabricating AAs, which enables exploration of biological variables like surface protein coating. By varying these chemomechanical cues, we can attempt to replicate the oligodendrocyte microenvironment, and elucidate potential causal relationships between these biophysical cues and the extent myelin ensheathment by oligodendrocytes.

While the AAs reported previously were a demonstrated proof of concept, there were some technical challenges that limited the scalability of the system. Firstly, printing on individual 5 mm-diameter coverslips was slow, and it would take at least two weeks to create sufficient samples to fill a 96-well plate. Furthermore, the yield was low, since the delicate sample handling requirements resulted in disproportionate damage of delicate AAs with lower diameter (<10 μm) and lower stiffness (<1 kPa). Put together, these limited the number of conditions that could be feasibly tested, which is why only two stiffness, diameter, and surface functionalization conditions were previously explored. These conditions were also limited in their biological fidelity; for example, 10 μm and 20 μm are non-physiologically large diameters for human axons, however it was technically difficult to reproducibly make smaller-diameter axons with consistent yield. In addition, the coverslip format introduced additional obstacles with imaging for myelin wrapping. Since the AA-containing coverslips were individually placed into 96-well plates, the coverslips were all slightly off alignment with respect to one other. Therefore, there was no way to automate image acquisition across all the wells at once, since it was necessary to travel through each well individually and realign the microscope to the coverslip inside. Therefore, this method of producing AAs would not be compatible with any high-throughput screen or drug discovery application.

In this thesis, I made progress towards advancing the Artificial Axon platform to increase the throughput and yield of AA fabrication. Doing so provides additional flexibility to explore two levers: First, how can we more precisely tune the axon stiffness, diameter, and interaxonal spacing by modifying the physicochemical conditions during polymer fabrication? Since AA fabrication was previously so slow, it was not practical to comprehensively probe how different fabrication conditions could change the axon's

shape and mechanical properties. By increasing production throughput, we were able to adjust and interrogate these fabrication levers in a more fine-grained fashion. Secondly, we leveraged this increased throughput and tunability to explore more granularly how changing these biophysical properties can affect myelin wrapping by OPCs. For example, within the physiological stiffness range, is there a causal relationship between the Young's modulus of AAs and the extent of myelin ensheathment around them?

1.4 Thesis goals and organization

Chapter 2 focuses on advancing the Artificial Axon platform to increase production throughput. We built a new high-resolution 3D printer (HR-3DP) that is amenable to fabricating AAs with custom geometries directly within a multi-well plate. To streamline the production process, we designed a LabView program to automate 3D-printing across multiple wells in one session, eliminating the need to handle delicate coverslips and reset the printer between samples. As a result, the time required to fill a 96-well plate with AAs decreased from 2 weeks to 1 hour. We then examined how modifying the fabrication conditions, including the UV exposure time and intensity, can fine-tune the geometry of AAs, examining a comprehensive suite of conditions that had previously been impractical to fully explore. Finally, we validated that AAs fabricated on the new HR-3DP are biocompatible with primary rat OPCs, using immunofluorescence microscopy to verify the presence of 3D myelin ensheathment. The chapter concludes with our attempts to visualize the ultrastructure of myelin using transmission electron microscopy (TEM) to explore whether our model system recapitulates the multilaminar myelin structure found *in vivo*.

Chapter 3 leverages the tunability of the HR-3DP to examine how features of the oligodendrocyte microenvironment influence myelination. We fabricated AAs with tunable Young's elastic moduli, diameters, and interaxonal spacings to investigate how each factor affected myelin ensheathment by primary rat OPCs. The increased fabrication throughput of the HR-3DP allowed us to expand upon the conditions previously tested to more physiological ranges. The biological relevance of this work is

twofold: first, previous studies demonstrate that during early development, OPCs are sensitive to axon stiffness and diameter[68]. Therefore, demonstrating that we can recapitulate the trends observed in developmental myelination can validate the AA platform as an *in vitro* myelination model. Second, we sought to model lesion-like environments to explore why remyelination may fail in some MS patients. Although our work does not explicitly address the question of *re*myelination following injury, our results can inform hypotheses about how changes to the oligodendrocyte microenvironment can either increase or decrease an oligodendrocyte's propensity to myelinate. We also drew inspiration from the lesion environment of multiple sclerosis to explore how exogenous myelin debris and microglia co-culture influence myelin ensheathment by OPCs.

Chapter 4 extends our work to hiPSC-derived oligodendrocytes, paving the way towards personalized disease models derived from individual patients' cells. First, we adapted the protocol to increase the reproducibility of deriving oligodendroglial cells from hiPSCs. Second, we explored how hiPSC-derived OPCs and rat primary OPCs differ in their myelination behavior, with a particular emphasis on their differential responses to pro-myelination drugs. Thirdly, we leveraged the hiPSC-derived oligodendrocytes to probe deeper into disease mechanisms, focusing on the role of APOE3/4 protein isoforms on myelination. We differentiated oligodendrocytes from APOE3 and APOE4 hiPSCs and quantified their myelin wrapping in the presence of different pro-myelination drugs. In particular, we observed that APOE3 and APOE4 oligodendrocytes differed in their intrinsic myelination potential, and also responded differentially to drugs affecting cholesterol metabolism pathways. These results demonstrated the potential of using AAs to elucidate disease mechanisms and uncover potential therapeutic targets for drugs to treat demyelinating diseases.

Finally, Chapter 5 distils key conclusions from this thesis and proposes future work, in particular to dig deeper into the biological mechanisms underlying the results obtained in this work.

1.5 References

1. Baumann, N. & Pham-Dinh, D. *Biology of Oligodendrocyte and Myelin in the Mammalian Central Nervous System*. http://physrev.physiology.org (2001).
2. Poitelon, Y., Kopec, A. M. & Belin, S. Myelin Fat Facts: An Overview of Lipids and Fatty Acid Metabolism. *Cells* **9**, 812 (2020).
3. Bradl, M. & Lassmann, H. Oligodendrocytes: Biology and pathology. *Acta Neuropathologica* vol. 119 37–53 (2010).
4. Franklin, R. J. M. & Ffrench-Constant, C. Regenerating CNS myelin - From mechanisms to experimental medicines. *Nat. Rev. Neurosci.* **18**, 753–769 (2017).
5. Nave, K. A. Myelination and support of axonal integrity by glia. *Nature* **468**, 244–252 (2010).
6. Franklin, R. J. M. Why does remyelination fail in multiple sclerosis? *Nature Reviews Neuroscience* vol. 3 705–714 (2002).
7. Duncan, I. D. & Radcliff, A. B. Inherited and acquired disorders of myelin: The underlying myelin pathology. *Experimental Neurology* vol. 283 452–475 (2016).
8. Kuhn, S., Gritti, L., Crooks, D. & Dombrowski, Y. Oligodendrocytes in Development, Myelin Generation and Beyond. *Cells* vol. 8 (2019).
9. Warf, B. C., Fok-Seang, J. & Miller, R. H. Evidence for the ventral origin of oligodendrocyte precursors in the rat spinal cord. *J. Neurosci.* **11**, 2477–2488 (1991).
10. Timsit, S. *et al.* Oligodendrocytes originate in a restricted zone of the embryonic ventral neural tube defined by DM-20 mRNA expression. *J. Neurosci.* **15**, 1012–1024 (1995).
11. Beiter, R. M. *et al.* Evidence for oligodendrocyte progenitor cell heterogeneity in the adult mouse brain. *Sci. Rep.* **12**, 1–15 (2022).
12. Fancy, S. P. J., Chan, J. R., Baranzini, S. E., Franklin, R. J. M. & Rowitch, D. H. Myelin regeneration: A recapitulation of development? *Annu. Rev. Neurosci.* **34**, 21–43 (2011).
13. Hughes, E. G., Kang, S. H., Fukaya, M. & Bergles, D. E. Oligodendrocyte progenitors balance growth with self-repulsion to achieve homeostasis in the adult brain. *Nat. Neurosci.* **16**, 668–676 (2013).
14. McKenzie, I. A. *et al.* Motor skill learning requires active central myelination. *Science (80-.).* **346**, 318–322 (2014).
15. Jäkel, S. & Dimou, L. Glial cells and their function in the adult brain: A journey through the history of their ablation. *Front. Cell. Neurosci.* **11**, 1–17 (2017).

16. Jessen, K. R., Mirsky, R. & Lloyd, A. C. Schwann cells: Development and role in nerve repair. *Cold Spring Harb. Perspect. Biol.* **7**, 1–15 (2015).
17. Gradisnik, L. & Velnar, T. Astrocytes in the central nervous system and their functions in health and disease: A review. *World J. Clin. Cases* **11**, 3385–3394 (2023).
18. Augusto-Oliveira, M. *et al.* What do microglia really do in healthy adult brain? *Cells* **8**, 1–17 (2019).
19. Potter, G. B. & Petryniak, M. A. Neuroimmune mechanisms in Krabbe's disease. *J. Neurosci. Res.* **94**, 1341–1348 (2016).
20. Willis, C. M. *et al.* Astrocyte Support for Oligodendrocyte Differentiation can be Conveyed via Extracellular Vesicles but Diminishes with Age. *Sci. Rep.* **10**, 1–14 (2020).
21. Ransom, B. R. & Ransom, C. B. *Astrocytes: Multitalented stars of the central nervous system. Methods in Molecular Biology* vol. 814 (2012).
22. Helman, G. *et al.* Disease Specific Therapies in Leukodystrophies and Leukoencephalopathies on behalf of the GLIA Consortium HHS Public Access Author manuscript. *Mol Genet Metab* **114**, 527–536 (2015).
23. Wolf, N. I., ffrench-Constant, C. & van der Knaap, M. S. Hypomyelinating leukodystrophies — unravelling myelin biology. *Nature Reviews Neurology* (2020) doi:10.1038/s41582-020-00432-1.
24. Chrast, R., Saher, G., Nave, K. A. & Verheijen, M. H. G. Lipid metabolism in myelinating glial cells: Lessons from human inherited disorders and mouse models. *Journal of Lipid Research* vol. 52 419–434 (2011).
25. Moser, H. W., Mahmood, A. & Raymond, G. V. X-linked adrenoleukodystrophy. *Nat. Clin. Pract. Neurol.* **3**, 140–151 (2007).
26. Zhu, J. *et al.* The Changing Face of Adrenoleukodystrophy. *Endocrine Reviews* vol. 41 (2020).
27. Singh, I. & Pujol, A. Pathomechanisms underlying X-adrenoleukodystrophy: A three-hit hypothesis. in *Brain Pathology* vol. 20 838–844 (Blackwell Publishing Ltd, 2010).
28. Ho, J. K., Moser, H., Kishimoto, Y. & Hamilton, J. A. *Interactions of a Very Long Chain Fatty Acid with Model Membranes and Serum Albumin Implications for the Pathogenesis of Adrenoleukodystrophy Key words: lipid bilayers * lipid metabolism * inborn errors * nuclear mag-netic resonance * calorimetry * differential scanning * serum albumin * bovine. J. Clin. Invest* vol. 96 (1995).
29. Giri, S., Khan, M., Rattan, R., Singh, I. & Singh, A. K. Krabbe disease: Psychosine-mediated

activation of phospholipase A2 in oligodendrocyte cell death. *J. Lipid Res.* **4**7, 1478–1492 (2006).

30. Lee, W. C. *et al.* Enzyme replacement therapy results in substantial improvements in early clinical phenotype in a mouse model of globoid cell leukodystrophy. *FASEB J.* **19**, 1549–1551 (2005).
31. Wenger, D. A. Murine, canine and non-human primate models of Krabbe disease. *Mol. Med. Today* **6**, 449–451 (2000).
32. Love, S. Demyelinating diseases. *Journal of Clinical Pathology* vol. 59 1151–1159 (2006).
33. Wallin, M. T. *et al.* The prevalence of MS in the United States: A population-based estimate using health claims data. *Neurology* **92**, E1029–E1040 (2019).
34. Frohman, E. M., Racke, M. K. & Raine, C. S. *Medical Progress Multiple Sclerosis-The Plaque and Its Pathogenesis*. www.nejm.org (2006).
35. Lassmann, H., Brück, W. & Lucchinetti, C. Heterogeneity of multiple sclerosis pathogenesis: Implications for diagnosis and therapy. *Trends in Molecular Medicine* vol. 7 115–121 (2001).
36. Ghasemi, N., Razavi, S. & Nikzad, E. *Multiple Sclerosis: Pathogenesis, Symptoms, Diagnoses and Cell-Based Therapy Citation: Ghasemi N, Razavi Sh, Nikzad E. Multiple sclerosis: pathogenesis, symptoms, diagnoses and cell-based therapy*. *CELL JOURNAL(Yakhteh)* vol. 19.
37. Ingelfinger, F. *et al.* Twin study reveals non-heritable immune perturbations in multiple sclerosis. *Nature* **603**, 152–158 (2022).
38. Masterman, T. *et al.* APOE genotypes and disease severity in multiple sclerosis. *Mult. Scler.* **8**, 98–103 (2002).
39. Yamazaki, Y., Zhao, N., Caulfield, T. R., Liu, C. C. & Bu, G. Apolipoprotein E and Alzheimer disease: pathobiology and targeting strategies. *Nat. Rev. Neurol.* **15**, 501–518 (2019).
40. Bjornevik, K., Münz, C., Cohen, J. I. & Ascherio, A. Epstein–Barr virus as a leading cause of multiple sclerosis: mechanisms and implications. *Nat. Rev. Neurol.* **19**, 160–171 (2023).
41. Wuerfel, J. *et al.* MR-elastography reveals degradation of tissue integrity in multiple sclerosis. *Neuroimage* **49**, 2520–2525 (2010).
42. Streitberger, K.-J. *et al.* Brain Viscoelasticity Alteration in Chronic-Progressive Multiple Sclerosis. doi:10.1371/journal.pone.0029888.
43. Schregel, K. *et al.* Demyelination reduces brain parenchymal stiffness quantified in vivo by magnetic resonance elastography. doi:10.1073/pnas.1200151109.
44. Riek, K. *et al.* Magnetic resonance elastography reveals altered brain viscoelasticity in

experimental autoimmune encephalomyelitis ☆. *YNICL* **1**, 81–90 (2012).

45. Makhija, E. P., Espinosa-Hoyos, D., Jagielska, A. & Van Vliet, K. J. Mechanical regulation of oligodendrocyte biology. *Neurosci. Lett.* **717**, (2020).
46. Lourenço, T. *et al.* Modulation of oligodendrocyte differentiation and maturation by combined biochemical and mechanical cues. *Sci. Rep.* **6**, (2016).
47. Urbanski, M. M., Brendel, M. B. & Melendez-Vasquez, C. V. Acute and chronic demyelinated CNs lesions exhibit opposite elastic properties. doi:10.1038/s41598-018-37745-7.
48. Segel, M. *et al.* Niche stiffness underlies the ageing of central nervous system progenitor cells. *Nature* **573**, 130–134 (2019).
49. Espinosa-Hoyos, D. *et al.* Mechanosensitivity of Human Oligodendrocytes. *Front. Cell. Neurosci.* (2020) doi:10.3389/fncel.2020.00222.
50. Jagielska, A. *et al.* Mechanical environment modulates biological properties of oligodendrocyte progenitor cells. *Stem Cells Dev.* **21**, 2905–2914 (2012).
51. Jagielska, A. *et al.* Mechanical strain promotes oligodendrocyte differentiation by global changes of gene expression. *Front. Cell. Neurosci.* **11**, 1–16 (2017).
52. Rosenberg, S. S., Kelland, E. E., Tokar, E., De La Torre, A. R. & Chan, J. R. The geometric and spatial constraints of the microenvironment induce oligodendrocyte differentiation. *Proc. Natl. Acad. Sci. U. S. A.* **105**, 14662–14667 (2008).
53. Lee, S. *et al.* A culture system to study oligodendrocyte myelination processes using engineered nanofibers. **9**, (2012).
54. Lubetzki, C., Zalc, B., Williams, A., Stadelmann, C. & Stankoff, B. Remyelination in multiple sclerosis: from basic science to clinical translation. *Lancet Neurol.* **19**, 678–688 (2020).
55. Melchor, G. S., Khan, T., Reger, J. F. & Huang, J. K. Remyelination Pharmacotherapy Investigations Highlight Diverse Mechanisms Underlying Multiple Sclerosis Progression. (2019) doi:10.1021/acsptsci.9b00068.
56. Kim, S. U. Formation of synapses and myelin sheaths in cultures of dissociated chick embryonic spinal cord. **73**, 528–530 (1972).
57. Jarjour, A. A., Zhang, H., Bauer, N., ffrench-Constant, C. & Williams, A. In vitro modeling of central nervous system myelination and remyelination. *Glia* **60**, 1–12 (2012).
58. Bornstein, M. B. & Murray, M. R. Serial observations on patterns of growth, myelin formation, maintenance and degeneration in cultures of new-born rat and kitten cerebellum. *J. Biophys. Biochem. Cytol.* **4**, 499–504 (1958).

59. Wood, P., Okada, E. & Bunge, R. The use of networks of dissociated rat dorsal root ganglion neurons to induce myelination by oligodendrocytes in culture. **196**, 247–252 (1980).
60. Takahashi, K. *et al.* Induction of Pluripotent Stem Cells from Adult Human Fibroblasts by Defined Factors. *Cell* **131**, 861–872 (2007).
61. Douvaras, P. *et al.* Efficient generation of myelinating oligodendrocytes from primary progressive multiple sclerosis patients by induced pluripotent stem cells. *Stem Cell Reports* **3**, 250–259 (2014).
62. Douvaras, P. & Fossati, V. Generation and isolation of oligodendrocyte progenitor cells from human pluripotent stem cells. *Nature Protocols* vol. 10 1143–1154.
63. Karanika, S., Karantanos, T., Li, L., Corn, P. G. & Timothy, C. Current Challenges of iPSC-Based Disease Modelling and Therapeutic Implications. **34**, 2815–2822 (2015).
64. Kelava, I. & Lancaster, M. A. Dishing out mini-brains: Current progress and future prospects in brain organoid research. *Developmental Biology* vol. 420 199–209 (2016).
65. James, O. G. *et al.* iPSC-derived myelinoids to study myelin biology of humans. *Dev. Cell* **56**, 1346-1358.e6 (2021).
66. Bullock, P. N. & Rome, L. H. Glass micro-fibers: A model system for study of early events in myelination. *J. Neurosci. Res.* **27**, 383–393 (1990).
67. Ong, W. *et al.* Biomimicking Fiber Platform with Tunable Stiffness to Study Mechanotransduction Reveals Stiffness Enhances Oligodendrocyte Differentiation but Impedes Myelination through YAP-Dependent Regulation. *Small* **16**, (2020).
68. Bechler, M. E., Byrne, L. & Ffrench-Constant, C. CNS Myelin Sheath Lengths Are an Intrinsic Property of Oligodendrocytes. *Curr. Biol.* **25**, 2411–2416 (2015).
69. Xue, J. *et al.* Nihms-Electrospinning and Electrospun Nanofibers: Methods, Materials, and Applications. *Chem Rev* **119**, 5298–5415 (2019).
70. Mei, F. *et al.* Micropillar arrays as a high-throughput screening platform for therapeutics in multiple sclerosis. *Nat. Med.* **20**, 954–960 (2014).
71. Merolli, A., Mao, Y. & Kohn, J. A suspended carbon fiber culture to model myelination by human Schwann cells. *J. Mater. Sci. Mater. Med. 2017 284* **28**, 1–8 (2017).
72. Howe, C. L. Coated Glass and Vicryl Microfibers as Artificial Axons. **55905**, 180–194 (2006).
73. Espinosa-Hoyos, D. *et al.* Engineered 3D-printed artificial axons. *Sci. Rep.* **8**, 1–13 (2018).
74. Espinosa-Hoyos, D., Du, H., Fang, N. X. & Van Vliet, K. J. Poly(HDDA)-Based Polymers for Microfabrication and Mechanobiology. *MRS Adv.* **2**, 1315–1321 (2017).

75. Yang, M. *et al.* Additive manufacturing of high aspect-ratio structures with self-focusing photopolymerization. *Light Adv. Manuf.* **3**, 542 (2022).

2. Advancing the Artificial Axon (AA) platform

Excerpts from Section 2.2 of this chapter are reproduced from Yang, Kowsari et al. (2022): Additive manufacturing of high aspect-ratio structures with self-focusing photopolymerization, published in Light: Advanced Manufacturing, DOI 10.37188/lam.2022.032

2.1 Projection microstereolithography

3D printing offers a promising approach to fabricate compliant biomaterials with customizable geometry and mechanical properties[1]. Most 3D printing methods assemble the target structure in a layer-by-layer manner. For example, in fused deposition modelling (FDM), a molten thermoplastic is extruded through a nozzle, where it deposits onto and fuses with the layer beneath it[2]. FDM was first invented in 1989 by Scott Crump, however recent studies have found that the viscous flow limits the resolution of FDM-fabricated structures to approximately 200 μm[3]. An alternative 3D printing approach is projection microstereolithography, in which a UV curable monomer resin is photopolymerized, typically also in a layer-by-layer manner[4]. In projection microstereolithography, a UV beam is sent through a dynamic photomask, which patterns the beam into the appropriate shape. When the beam is incident upon the sample, the regions that are exposed will rapidly polymerize into a solid structure. Since PμSL does not depend on rapid solidification from the melt (relying instead on the rapid *de novo* synthesis of the polymer), micron-level printing resolutions have been reported for stiff materials ($E > 10^6$ Pa)[5].

The chemical basis of projection microstereolithography is the formation of crosslinked polymer networks through free-radical chain-growth polymerization. In this process, a photoinitiator molecule first undergoes homolytic fission to generate a pair of free radicals. These active radicals then react with monomers containing a C=C double bond, endowing these monomers with a free radical. After this chain initiation step, the activated monomer can react with other available C=C bonds on other monomers to

facilitate chain growth, with each step regenerating the reactive free radical on the end of each chain. This propagation step involves the successive addition of new monomers to the growing chain, concluding in polymer formation. Importantly, if the monomer is multifunctional and contains multiple branchpoints for potential chain elongation, then the resultant structure comprises a solid polymer network.

Projection stereolithography has been used for a number of 3D fabrication applications, including microfluidic devices[6–8], miniature actuators[9], biotechnologies[10], and optical devices[11]. Many groups have leveraged the micron-scale resolution of projection microstereolithography to print biomimetic structures. For example, one group used the technique to fabricate bioinspired structures including an artificial abalone shell, mantis shrimp, and cortical bone, reinforcing each structure with magnetic nanoparticles to recapitulate the biomineralization of each structure[12]. Another common use case is to design superhydrophobic surfaces, which are found across nature in structures like lotus leaves and rose petals. One group used projection microstereolithography to design a textured, superhydrophobic surface with micron-level features, mimicking analogous hydrophobic structures found in nature[13].

In addition to fabricating diverse spatial features, projection microstereolithography is also compatible with a wide range of polymer chemistries, including printing biocompatible polymers. One group used projection microstereolithography to generate 3D villi-like microstructures on poly(ethylene glycol)-based hydrogels for intestinal tissue models. The hydrogel micro-scaffolds were easily integrated within standard cell characterization techniques, such as a commercial Transwell® system to support the growth of epithelial cells and to evaluate the barrier properties of the biomimetic intestinal epithelium formed. This example highlights the potential to leverage both the micron-scale geometries and the polymer biocompatibility to use projection microstereolithography as an *in vitro* biological model[14].

Previous work in our lab has used projection microstereolithography to fabricate Artificial Axons (AAs), free-standing pillars of around 4+ μm diameter that can be ensheathed by oligodendrocyte progenitor cells (OPCs). Espinosa-Hoyos et al. previously

reported on a custom polymer chemistry consisting of 4-arm PEG acrylate (starPEG) and 1,6-hexanediol diacrylate (HDDA), shown in **Figure 5.** When starPEG, HDDA, and a photoinitiator species are exposed to UV light, the incident UV light causes the photoinitiator to produce free radicals, which can activate any of the C=C double bonds in starPEG or HDDA to initiate polymer chain propagation. Since starPEG is multifunctional and contains 4 C=C groups, each has the potential to be initiated with a free radical. Therefore, free radical polymerization gives rise to a network polymer structure, which is responsible for the solidification of the polymer from its liquid resin.

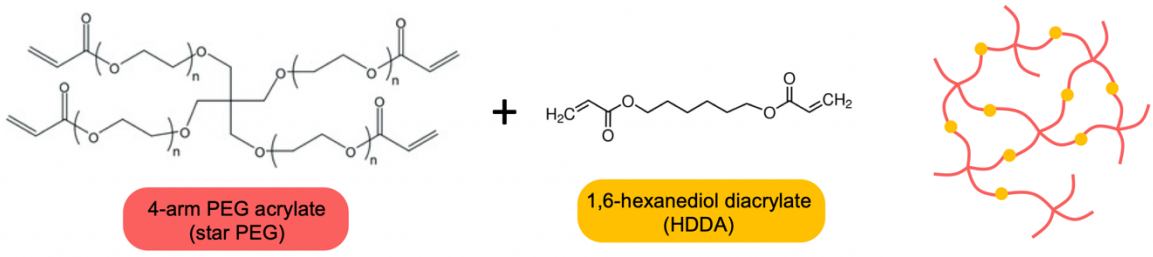

Figure 5 Structures of 4-arm PEG acrylate and 1,6-hexanediol diacrylate, used to fabricate Artificial Axons (AAs)

Prior to our work in the lab, the use of HDDA has been widely documented for projection microstereolithography applications[15,16]. However, structures fabricated from poly(HDDA) alone have low biocompatibility; for example, Espinosa-Hoyos et al. found that poly(HDDA) substrates hinder the differentiation and survival of primary rat OPCs[4] compared to a tissue control polystyrene (TCPS) control. Furthermore, the Young's elastic modulus of poly(HDDA) materials is typically on the order of MPa, which is significantly stiffer than brain tissue[17]. Our group and others have demonstrated that oligodendrocytes and OPCs are sensitive to external mechanical cues such as ECM stiffness[18–22], therefore the behavior of oligodendrocytes on pure poly(HDDA) materials may not accurately reflect their *in vivo* behavior. Incorporating starPEG into the copolymer enables the fabrication of more compliant axon-mimicking materials, thus enabling further studies into oligodendrocyte mechanobiology within a more physiologically representative range. Furthermore, Espinosa-Hoyos et al. found that

adding starPEG was beneficial for biocompatibility, leading to increased OPC survival and differentiation compared to the poly(HDDA) homopolymer substrate.

2.2 Self-propagating polymer waveguides

Projection microstereolithography can be further augmented by capitalizing on the phenomena of light self-trapping and self-propagation. In brief, incident light causes the monomer resin to undergo local photopolymerization, thereby producing a spatially localized increase in refractive index. As the light beam continues propagating through the medium, the refractive index change causes a self-focusing of light along its propagation path. Self-focusing is initiated when an incident Gaussian light beam induces a refractive index change in the medium through which it travels. Initially, before the onset of polymerization, the incident beam can diffract freely through the liquid resin. Over time, the exposed regions will undergo photopolymerization and solidify, which locally increases the index of refraction. The changes in refractive index contribute to the formation of a quasilens at the tip of this waveguide that focuses the light (i.e., self-focusing)[23]. These changes overcome the natural diffraction of the beam, causing the beam to taper and become trapped along the propagation axis. This self-focusing phenomena counteracts the natural tendency of light to diverge along its propagation path. Consequently, the light beam continues propagating divergence-free, within its own self-induced waveguide[24]. The resultant material and the associated phenomenon are termed a self-propagating polymer waveguide (SPPW). Through the strategic self-trapping and self-focusing of light in a photosensitive medium—primarily photopolymers—SPPW prototyping can be used to produce fiber-like nano and microstructures at unprecedented throughputs[25]. Leveraging SPPW can enable the fabrication of high aspect-ratio (up to 1:75), cylindrical architectures such as axon mimics.

The extent to which photopolymers densify depends on the structure of the monomer and the presence of diluents in the resin. In one study, researchers compared the extent of volume shrinkage between different difunctional ether acrylate resins.

Resins with higher molecular weight were found to exhibit less volumetric shrinkage and reduced index change upon polymerization (**Figure 6A**). In addition, volume shrinkage was higher with aliphatic molecules compared to bulkier aromatic monomers (**Figure 6B**)[26]. Furthermore, addition of the diluent poly(propylene glycol) diacrylate (PPGDA) increased the index augmentation achieved during polymerization (**Figure 6C**). For example, Δn_D of bisphenol A epoxy diacrylate in the absence of diluent was 0.0204, whereas Δn_D in the presence TPGDA diluent was 0.0219. The effect of the diluent can be explained as follows. Firstly, the diluent lowers the initial refractive index of the pre-polymerized resin by increasing the effective intermolecular spacing. Secondly, such diluents lower the glass transition temperature T_g of the sample, which enhances the polymerization conversion and ultimately increases the amount of network shrinkage attainable. Therefore, researchers hypothesized that diluents enhance index change via two mutually cooperative mechanisms: reducing the initial density of the pre-polymerized resin, and increasing the change in density (i.e., greater shrinkage) after polymerization. Other diluents, such as ethylene glycol vinyl ether (EGVE) diluent, have also been deployed for fabricating polyurethane diacrylate waveguides[27]. Finally, the number of functional groups also plays an important role in determining network shrinkage. Zhang et al. studied self-trapping in organosiloxanes with had varying concentrations of methacrylate groups in the monomer. They found that monomers with more methacrylate groups resulted in increased index modulation and increased self-trapping efficiency[28].

A major barrier to achieving the refractive index change is that vinyl monomers exhibit a decrease in polarizability during polymerization. One approach to counteract this effect is to incorporate a photoactive species that exhibits a polarizability *increase* upon irradiation. Tolstik et al. reported on the use of a photoactive dopant, phenanthrenequinone (PQ), for the fabrication of poly(methyl methacrylate) (PMMA) waveguides. Before polymerization, the monomer (methyl methacrylate) solution is doped with PQ molecules. During polymerization, UV light induces the irradiated PQ molecules to undergo a photoattachment reaction to the growing polymer chains (**Figure**

6D)[29,30]. UV-Vis spectroscopy data indicate that the molecular structure of PQ becomes less conjugated during photoattachment, giving rise to an increase in refractive index within the irradiated region[31]. Consequently, the irradiated regions undergoing photopolymerization experience an index increase from PQ photoattachment, whereas the non-irradiated regions exhibited no such index augmentation. Since the PQ dye is only a minor fraction of the material composition (<0.7 wt %), the structure of the overall polymer matrix is unaffected by the presence of the dopant[32]. Tolstik et al. used the PQ-doped system to fabricate waveguides using light self-trapping, with higher concentrations of PQ dopant producing greater index modulation. Tolstik et al. found index changes of around 10^{-4} with this photoattachment mechanism, which is lower than those achieved through network shrinkage. However, even these changes were sufficient for waveguide formation, suggesting that index changes on the order of 10^{-4} are sufficient for SPPW formation[29,30].

Many photopolymer systems have been developed using the inclusion of photoactive dopants. Becker et al. fabricated optical waveguides using polystyrene doped with *p*-nitroaniline derivatives[33]. Becker et al. hypothesized that the dispersion of the phenyl-containing dopants increased the electron density of the polymer matrix, which enhanced the index modulation. In a similar vein, Kudo et al. reported large refractive index changes before/after the irradiation of poly(methyl methacrylate) containing 2-phenyl-2,5-norbornadiene. UV-Vis spectroscopy data verified that the 2-phenyl-2,5-norbornadiene moieties were photosensitive and underwent photochemical isomerization upon irradiation, which mediated the index augmentation[34]. Index changes were on the order of 0.05 to 0.1 with varying chemistries, which suggests these photoactive dopants hold promise in SPPW fabrication.

In addition to photoactive species added to the reaction mixture, the photoactive groups can be directly conjugated to the polymer backbone (**Figure 6E**). Poly(methyl methacrylate) with pendant anthracene groups also produced index modulation, and this system was used to fabricate waveguides[35]. The anthracene moieties were also found to be photosensitive, undergoing an analogous photoisomerization reaction upon

irradiation. Morim et al. synthesized a poly(acrylamide-*co*-acrylic acid) (p[AAm-*co*-Aac]) hydrogel containing covalently attached SP chromophores. Upon irradiation with visible light, the chromophore undergoes a photoisomerization reaction from an open-ring form to a closed-ring form. Not only does the photoisomerization induce a local increase in refractive index, it also increases the hydrophobicity of the hydrogel, which triggers the expulsion of water and local network shrinkage of the hydrogel[36].

Another strategy to locally increase the refractive index of the polymerizing region is to induce a structural change in the polymer itself. Kleine et al. developed an index-changing polymer system consisting of *t*-BOC-protected poly(4-hydroxystyrene), which was doped with photoacid generators (PAGs) in the reaction mixture. During photolithography, UV irradiation causes the PAGs to undergo a photocatalytic deprotection reaction that replaces hydroxyl groups in the *t*-BOC sidechain with thiol groups. Since thiol moieties have higher intrinsic refractivity than hydroxy groups, this deprotection reaction increased the overall refractive index of the material (by an order of 10^{-2}), which was subsequently used to fabricate waveguides[37]. This example elucidates a novel approach for index modulation by directly modifying the structure of the repeat unit, swapping out low-refractivity moieties for high-refractivity moieties (**Figure 6F**). All of the processes described above take place within the irradiated area, which localizes the index augmentation to the photopolymerizing region.

Since we fabricate AAs with a similar free-radical crosslinking chemistry, our starPEG/HDDA copolymers also exhibit network shrinkage and refractive index change during photopolymerization[38]. Therefore, we can draw from this wide body of work to polymerize high aspect-ratio AAs within a single round of UV projection; this paves the way to replacing the current (and slower) layer-by-layer approach to fabricate the desired columnar geometries, with a faster one-shot approach.

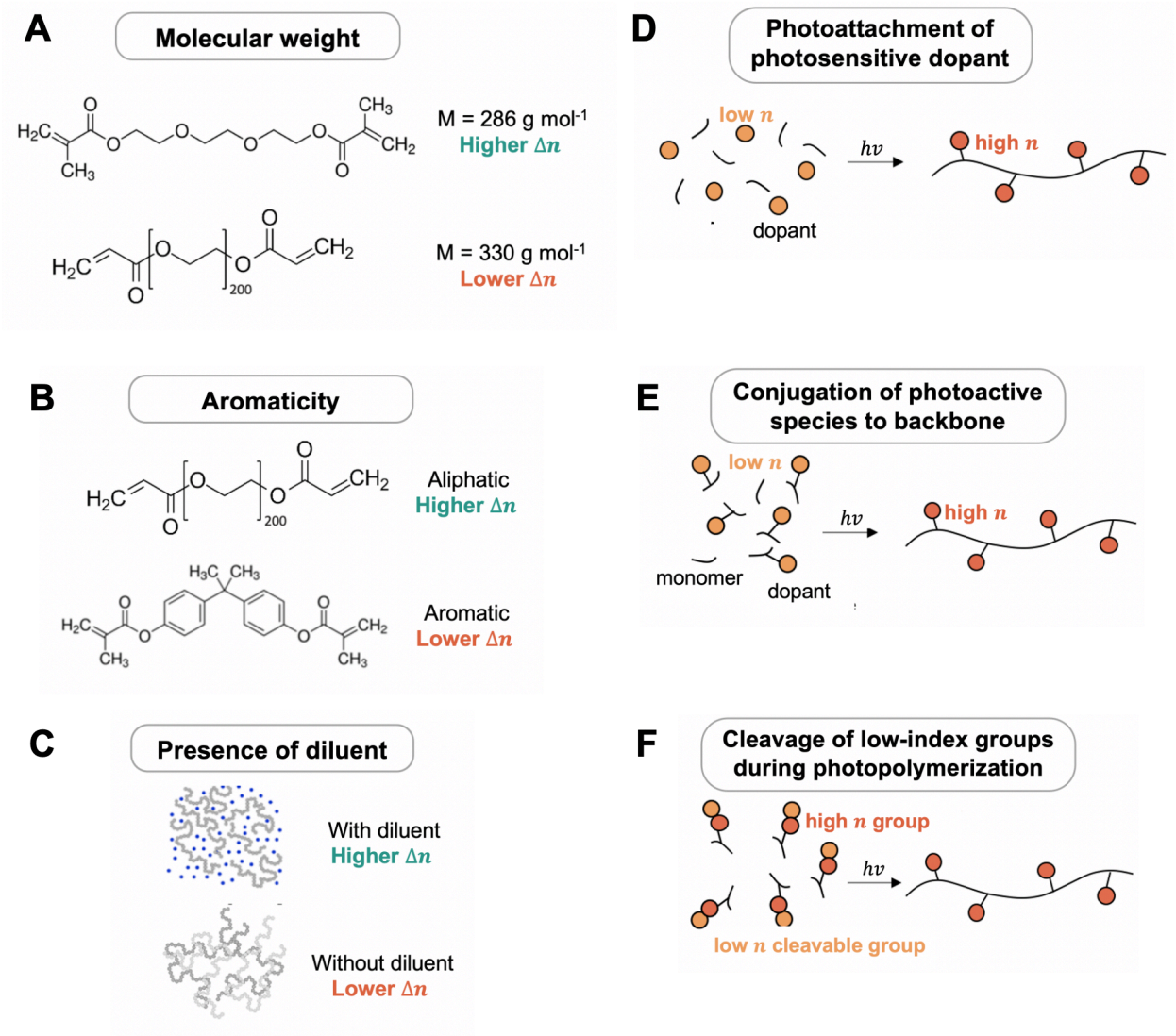

Figure 6 Materials approaches for achieving index modulation for SPPW, using (A) molecular weight monomers[26], (B) aliphatic monomers[26] and (C) an inert diluent[26]. Achieving spatial control over refractive index change via (E) a photoattachment reaction of a photosensitive dopant to the monomer during polymerization[39], (F) a photoactive molecule that is directly conjugated to the monomer[34], or (G) a photoactivated cleavage reaction of low-index groups during polymerization[37]. Figure adapted from Yang, Kowsari et al. (2022)[40]

2.3 Building a high-resolution 3D printer

In Chapter 1, we introduced prior work on developing a custom 3D-printing setup for fabricating Artificial Axons (AAs), shown in **Figure 7 A**. When the liquid starPEG/HDDA resin is exposed to UV light, it polymerizes into a solid structure onto a glass coverslip. Then, the glass coverslip is raised, and photopolymerization proceeds in

a layer-by-layer fashion until the entire 3D structure is formed. However, production throughput was low, typically taking over 2 weeks to generate sufficient coverslips to fill a 96-well plate. This problem was exacerbated by the low sample yield, because the delicate sample handling requirements led to disproportionate damage to the low-stiffness and low-diameter AAs. In my thesis, we sought to overcome these challenges by building a new high-resolution 3D printer (HR-3DP) set-up illustrated in **Figure 7 B**.

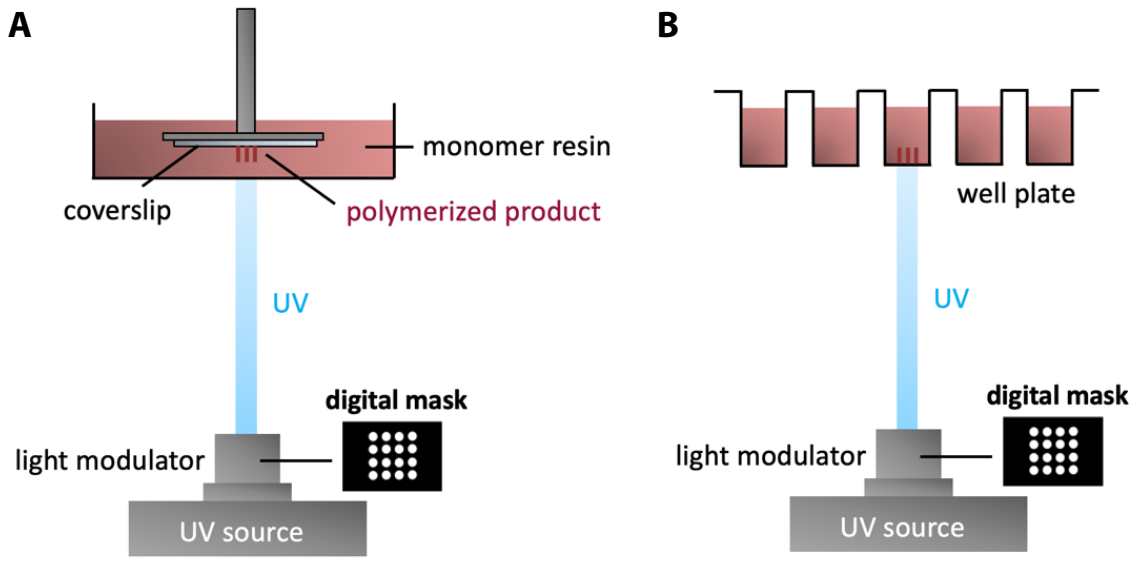

Figure 7 (A) Schematic of previous 3D printing set-up, with fabrication onto a coverslip. (B) Schematic of new 3D printing set-up, with fabrication directly into well plate.

In collaboration with Anna Jagielska and Kavin Kowsari, we designed the HR-3DP to be compatible with the HDDA/starPEG chemistry previously used to make AAs. However, the HR-3DP set-up had some significant changes from the previous 3D printer, outlined below.

First, axons were fabricated directly within well plates instead of on coverslips. To adhere the solid AAs to the bottom surface of the well plate, we functionalized the glass well with 3-(trimethoxysilyl)propyl methacrylate (TMSPMA). The functionalization protocol was adapted from that previously used to functionalize the glass coverslips. First, we exposed well plates to air plasma to endow the well surface with hydroxyl (OH)

groups. Then, we added a solution containing TMSPMA to the well plate to endow the surface with acrylate groups, shown in **Figure 8**. During polymerization, the free-radical activated growing chains can covalently attach to the acrylate groups, thus adhering the base of the AA to the well plate.

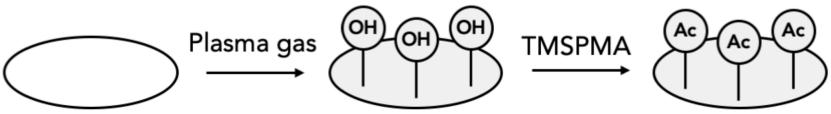

Figure 8 Chemical functionalization of the glass well plate surface to facilitate AA adhesion during 3D printing

If the well plate is incompletely functionalized, the AAs fail to stay upright after being photopolymerized, which is easily observable via brightfield microscopy (**Figure 9**). Fabricating AAs directly within well plates eliminated all the problems we previously encountered with low sample yield. Previously, it was common to only have one usable sample in every 10-20 prints; in contrast, now the yield is approximately 100%, and virtually every AA that is printed within the well plate is usable for downstream experiments.

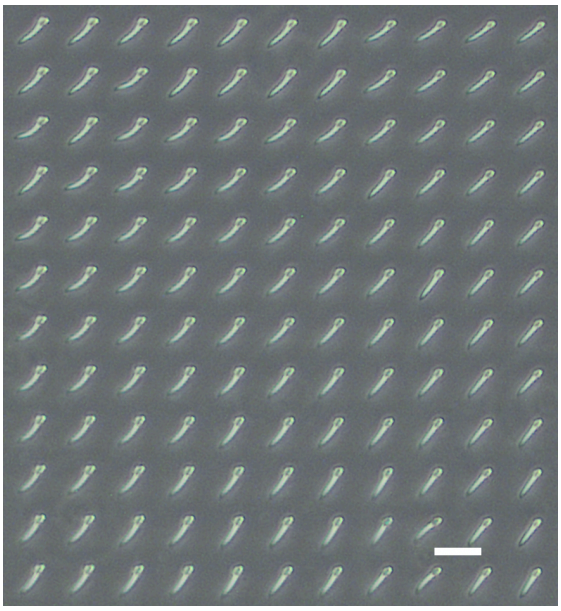

Figure 9 Plan view from brightfield microscope of AAs that toppled over after fabrication due to incomplete plate functionalization. Scale bar is 30 μm. Confocal micrographs of non-toppled pillars are shown in **Figure 11**.

The second major change was to eliminate the layer-by-layer fabrication approach. Instead, we leveraged the fact that the SPPW phenomena was compatible with photopolymerizing solids with columnar geometries. Therefore, we now polymerize the AAs in a single, low-intensity exposure by projecting an array of circular dots corresponding to the geometric pattern of the AAs. After ~1-5s of exposure to the UV pattern, the base of the resin initially photopolymerizes, causing a local change in refractive index which self-focuses the UV light to continue propagating upwards through the resin. As the UV light continues propagating upwards, the resin through which it propagates continues to solidify. In this way, the solidifying resin acts as an 'optical fiber' that self-focuses the light, continuing until the final columnar structure is formed. Removing the need to polymerize layer-by-layer also increased the production speed. Whereas previously it took over two weeks to generate enough AA-filled coverslips to populate a 96-well plate, now it takes approximately an hour to 3D-print AAs in a full well plate.

Figure 10 shows a photograph of the high-resolution 3D-printer in operation. The set-up contains two independently moving pieces. First, we placed the multi-well plate onto a stationary plate holder, positioned above the UV light source. Fixing the position of the well plate ensured that it was permanently level with the table surface, and also provided a fixed coordinate axis for positioning the UV light source. Secondly, we mounted the UV light source and a camera onto the same motorized stage. The light source and motorized stage were both connected to a PC, allowing the operator to move the light source towards a target well and project a specific pattern into that well. Fixing the camera onto the same motorized stage ensured that the camera constantly tracked the projection from the UV source.

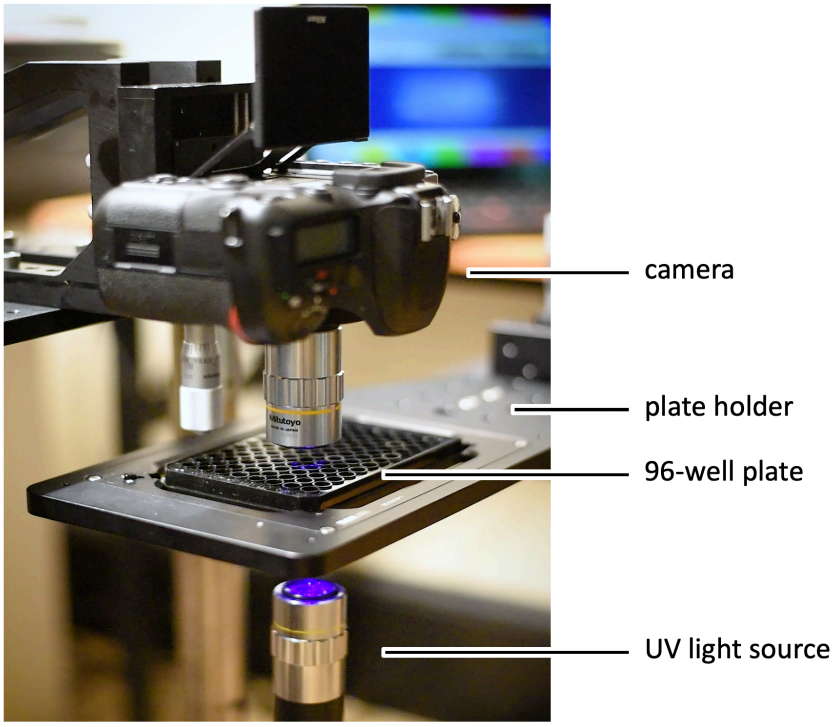

Figure 10 Photograph of high-resolution 3D printer (HR-3DP)

To automate the printing process, we designed a LabView program with embedded graphical user interface (GUI), in which users can select *which* wells to project light into and *what* patterns to project into each well. Therefore, the overall workflow for fabricating AAs with the new HR-3DP is as follows:

(a) Functionalize the well plate using air plasma and TMSPMA.

(b) Use Photoshop to create a 'digital mask', consisting of a set of white dots on a black background. This corresponds to the UV pattern to be projected, which will solidify the resin into columnar pillars whose geometries correspond to the mask.

(c) Pipette liquid HDDA/starPEG resin the wells for printing, and mount the well plate onto the plate holder.

(d) Use the GUI embedded within the LabView code to specify which well to print in, and what mask to project in that well. At this stage, the user can also specify the projection conditions, including the exposure time and intensity of the UV light.

The field of projection of the UV source is smaller than the total surface area of the well. Therefore, to fully cover each well with arrays of AAs, we typically project a 3x3 grid of AAs. Each component of the 3x3 grid is itself an array of AA pillars; after all 9 projections are stitched together, they form a complete array of AAs that fills the center of each well. In sum, the new HR-3DP provides significantly greater throughput and user flexibility, by offering many knobs the user can adjust – which well to project in, what masks and how many to project in each well, and under what UV conditions each projection should be made.

We used confocal microscopy to visualize the 3D morphology of the printed AAs. To do this, we incorporated a fluorescent dye rhodamine B into the resin, alongside the starPEG and HDDA components. After the axons are printed in each well, the contents of the well are washed ~5 times with 70% ethanol, to remove excess unpolymerized resin. After replacing the ethanol with phosphate buffered saline (PBS) solution, which reduces fluorescence background, the AAs can then be imaged using confocal microscopy, which enables a 3D volume reconstruction of the axons. **Figure 11** shows a representative confocal micrograph of one set of AAs printed using the HR-3DP.

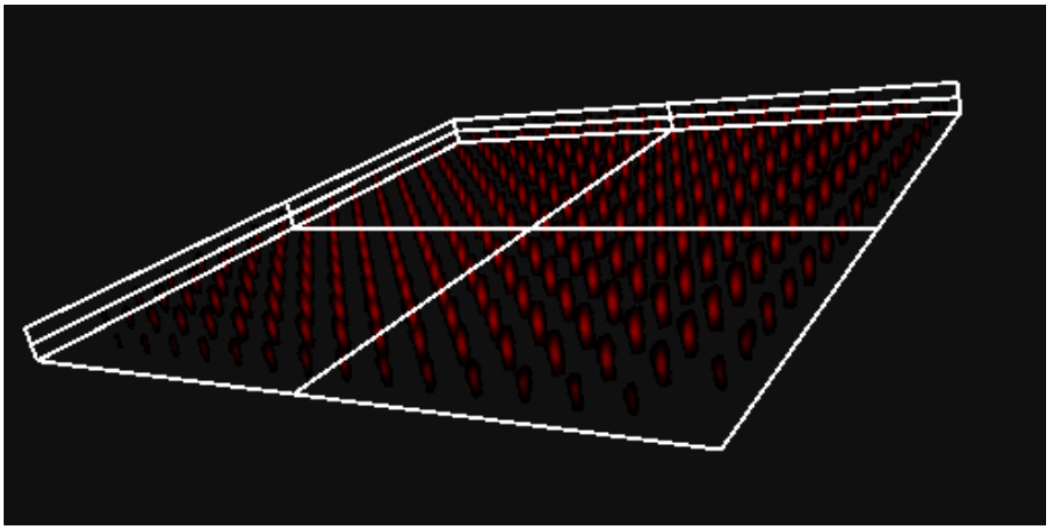

Figure 11 Example confocal microscope volume reconstruction of an AA array, printed using the HR-3DP. Axons are 30 μm apart and have 3 μm diameter.

During the initial troubleshooting phase to build the HR-3DP, we found that it was extremely important to have all mechanics firmly anchored onto a mechanical breadboard. decoupled from all other equipment in the laboratory space. During early phases of printing on the HR-3DP, we found that the UV projection exhibited a baseline level of vibration, which resulted in all axons exhibiting a swollen morphology (**Figure 12**). When we bolted all components onto a mechanical breadboard, vibrations stopped, and AAs more closely resembled those in **Figure 11**. Furthermore, it was essential to isolate the HR-3DP on a vibration isolation table. In contrast, when the HR-3DP was mounted on a non-isolated (e.g., non-damped) surface, vibrations from individuals walking around the table were propagated to the HR-3DP and also exacerbated vibrations in the UV projection.

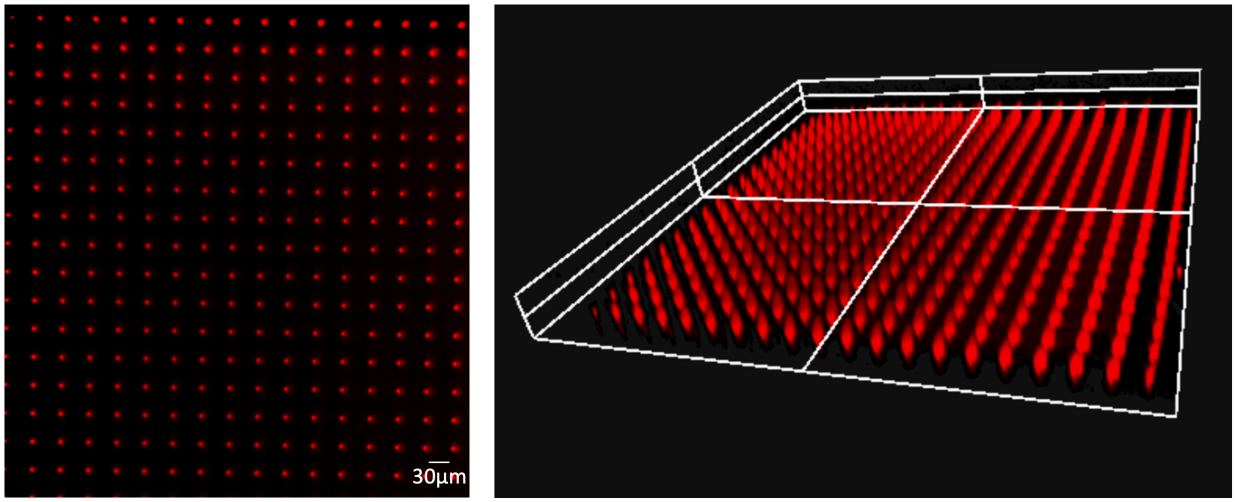

Figure 12 Swollen AA morphology during early phases of testing due to unresolved vibration issues

2.4 Photochemical control of axon geometry

A key advantage of the AA platform is the ability to tune the mechanical properties and geometry of the axons. This allows us to probe biological questions about how cells respond to chemomechanical cues in their microenvironment; for example, to what extent axon stiffness, diameter, and interaxonal spacing may affect oligodendrocytes' propensity to myelinate. A necessary prerequisite to answering these questions is being able to fabricate axons with precisely controlled geometries.

The first adjustable lever is the digital mask itself. By projecting a different array of white dots, different axon densities and diameters can be achieved. **Figure 13** shows an example of the geometric variation possible by changing just the digital mask alone. We started with AAs that of diameter 4 µm and had interaxonal spacings of 30 µm. By varying the design of the digital mask, we could independently vary the diameter and interaxonal spacing. In one condition, we spaced out the white dots in the digital mask, which increased the interaxonal spacing to 50 µm while preserving the diameter. In the other case, we preserved the interaxonal spacing, but increased the pixel width of each axon, which increased the diameter to 9 µm.

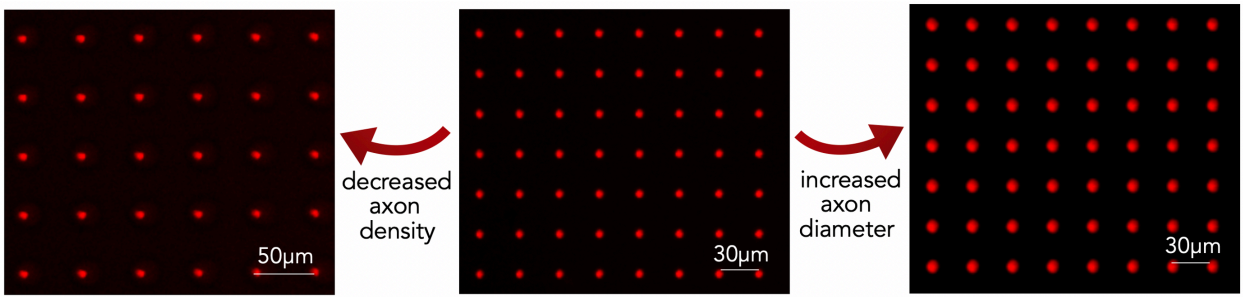

Figure 13 Variation in axon density and diameter achievable by modifying the digital mask

Although changes to axon geometry are achievable by varying the digital mask, just varying this parameter alone is not sufficient to achieve fine-grained changes at the micrometer-resolution level. For instance, increasing the axon diameter in the digital mask from 1 pixel to 2 pixels corresponded to a ~5 μm increase in the physical AA diameter. To achieve more fine-grained variation in diameter, we varied the physicochemical conditions during photopolymerization, namely the UV exposure time and duration. We leveraged the increased fabrication throughput achievable by the HR-3DP to test a more comprehensive suite of exposure conditions than was previously achievable with the first-generation 3DP.

To investigate the role of UV exposure time and intensity on AA diameter, we produced a digital photomask comprising an array of single-pixel white dots on a black background, spaced apart by 30 pixels. We projected a UV beam of this mask to polymerize a resin with 3:1 HDDA:starPEG ratio across a range of exposure times (0.5s – 2s) and light intensities (100-250, measured on an arbitrary scale of 0-255). Finally, we used confocal microscopy and ImageJ[41] to quantify the distribution of resultant AA diameters. As expected, increasing both the UV exposure time and light intensity produced a concomitant increase in axon diameter, shown in **Figure 14**. This is consistent with the free-radical mediated polymerization mechanism through which the AAs form. UV exposure initiates polymerization by imparting reactive free radicals onto the monomer species. Increasing the light intensity increases the quantity of free radicals produced, thereby causing more monomers to react and producing higher-diameter

axons from the same 1-pixel digital mask. A similar argument holds for increasing the exposure duration. Furthermore, we found that UV exposure duration and intensity both had to exceed a critical threshold for polymerization (i.e., in order for any AAs to form). In sum, adjusting the exposure conditions enables fine control over axon diameter, thus paving the way to investigate how this parameter may influence myelination by oligodendrocytes.

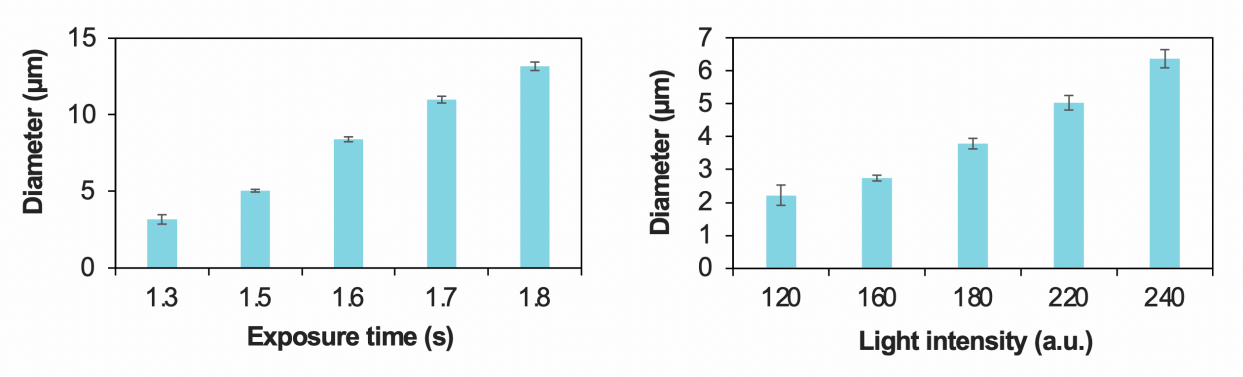

Figure 14 Effect of UV exposure time and light intensity on average AA diameter. Light intensity is measured on a unitless scale of 0 to 255. Error bars are the standard errors of the mean, averaged across all AAs in the field of view.

These results were promising as they indicated the potential for fine-grained diameter control by varying both exposure time and light intensity. We next asked what was the lowest achievable axon diameter, since biological axons can reach single-micrometer diameters. In **Figure 14**, we found that the lowest possible exposure time for polymerizing AAs is 1.3 s, and the lowest light intensity for polymerizing AAs is 120 (on a pixel intensity scale from 0 to 255). Since the lowest-diameter axon would be achieved at the lowest possible light intensity and shortest exposure time, we fixed the exposure time at 1.3 s, and lowered the light intensity from 255 to 0. Then, we did the analogous experiment with fixing light intensity at 120 and lowering the exposure time from 5 s to 1 s.

We found that at the lowest possible exposure time and intensity limit, the AA diameters were on average 2.5 μm. Interestingly, the very outermost perimeter of AAs

had an average diameter of 1.5 μm, but it was not possible to find a set of exposure conditions that would allow the bulk of the array to all be single-micron axons. One possible explanation is that the UV projection contains an unavoidable baseline degree of UV background light, even in regions where the digital mask was black. Therefore, we hypothesize that off-target generation of free radicals from this background light may have contributed to the widening of axons to >2.5 μm in the center. In contrast, in the outermost perimeter, where comparatively fewer free radicals were generated, the AAs retained their 1.5 μm diameters. These results showed that making AAs close to 1 μm wide is theoretically possible, despite current hardware limitations preventing us from generating a full array of single-micron axons in the bulk of the array. Future work could explore whether a UV projector with enhanced contrast between foreground and background could pave the way towards reproducibly generating single-diameter axons.

2.5 Biocompatibility of AAs with murine oligodendrocytes

To verify that the AAs made by the HR-3DP were biocompatible for OPC culture, we printed a set of AAs into ten wells of a 96-well plate. We used an AA diameter of 5 μm and an interaxonal spacing of 30 μm. Immediately after printing, we washed each well five times with ethanol to remove excess, undissolved resin, which is cytotoxic. After removing the ethanol, we then incubated the AA with poly(ornithine) and then natural mouse laminin[10].

We seeded each AA-containing well with primary rat OPCs and cultured for seven days. The culture medium contained 1 μM of the pro-myelinating compound T3 (triiodo-L-thyronine), consistent with previous work in our lab that used T3 as a positive control for myelin wrapping. After culture, the cells were fixed and stained for myelin basic protein (MBP), and imaged using confocal microscopy. **Figure 15** shows a plan view confocal micrograph of MBP+ oligodendrocytes ensheathing the AAs. Chapter 3 will discuss how we quantified this myelin wrapping in three dimensions.

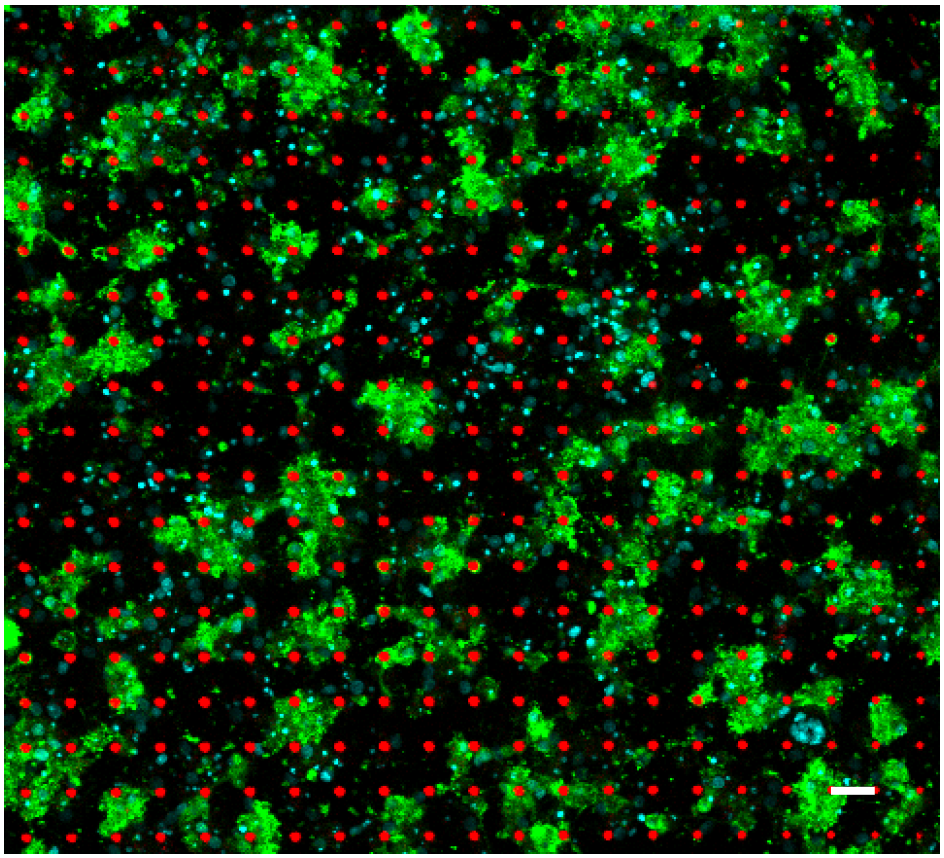

Figure 15 Plan view confocal micrograph of rat oligodendrocytes depositing MBP+ myelin around AAs. Scale bar is 30 μm.

These data confirmed that the AAs fabricated by the HR-3DP were indeed biocompatible, and were amenable to OPC differentiation and myelin ensheathment. Another significant benefit of the HR-3DP is the compatibility with automated image collection by the confocal microscope. Previously, when AAs were fabricated on coverslips, each coverslip was individually lowered into a well, which led to subtle misalignment between each coverslip. As a result, automating the image collection was not possible, because it was necessary to realign the microscope to each coverslip's focal plane. Now that every single AA is printed directly into the well plate, it is now possible to automate the confocal microscope to collect images from every single well within a single imaging session.

2.6 Determination of myelin ultrastructure around AAs

Myelin *in vivo* has a characteristic multilaminar structure, often termed compact myelin[42]. We sought to verify whether the myelin ensheathed around AAs also exhibited this compact multilaminar morphology. Transmission electron microscopy (TEM) is a powerful imaging modality that can achieve Angstrom-level resolution[43], and is now the standard method of imaging compact myelin. To prepare a sample for TEM, it must be first embedded within a liquid epoxy resin which is then baked in a furnace to solidify. Then, the epoxy-embedded sample is sectioned into thin sheets to image. **Figure 16** shows a schematic of the sample preparation process.

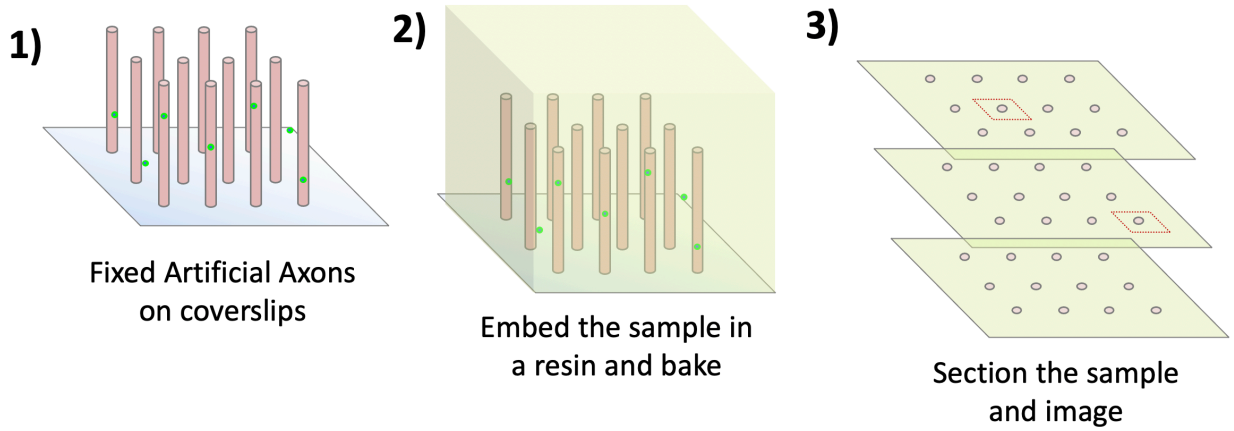

Figure 16 Schematic of sample preparation process for transmission electron microscopy (TEM)

Notably, the resin embedding process is not conducive to samples in a well plate format, since it is not possible to bake the resin within a well. Therefore, we printed AAs on a functionalized glass coverslip, using the same printing conditions as outlined above to generate 3 µm samples with 30 µm spacing. Importantly, we began by using a hydrophobic pen to draw a square barrier on the coverslip to contain the resin, acting as de facto walls (**Figure 17**). This hydrophobic barrier also served the additional purpose downstream of helping to contain the culture media for the cells.

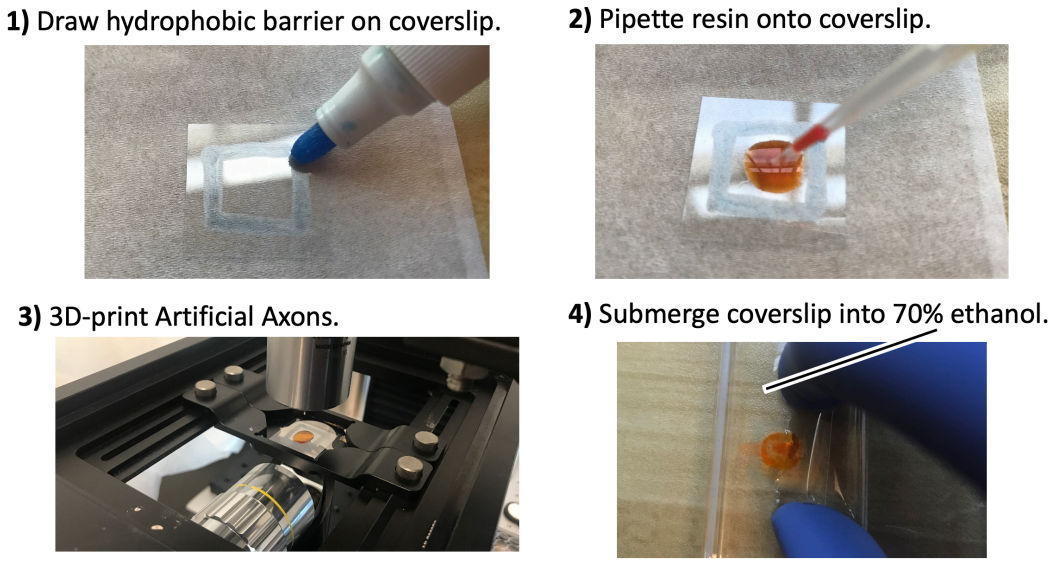

Figure 17 Process of fabricating AAs on functionalized glass coverslips for TEM analysis

After fabricating the AAs, we placed each coverslip into a well of a 6-well plate and washed the AAs in serial dilutions of ethanol in distilled water. This process was to remove any residual unreacted resin, which would be cytotoxic to cells. We found that it was critically important to securely adhere the coverslip to the bottom of the 6-well plate using vacuum grease. If the coverslips are not attached to the bottom of the well, during the washes, the coverslips would float on the ethanol solution. The unstable bobbing of the coverslip on the solution surface led to AAs toppling over, like shown in **Figure 9**. When the coverslips are correctly adhered, the AAs look as shown in **Figure 11**. The washed AAs were then functionalized with poly(ornithine) and natural mouse laminin prior to seeding with primary rat OPCs.

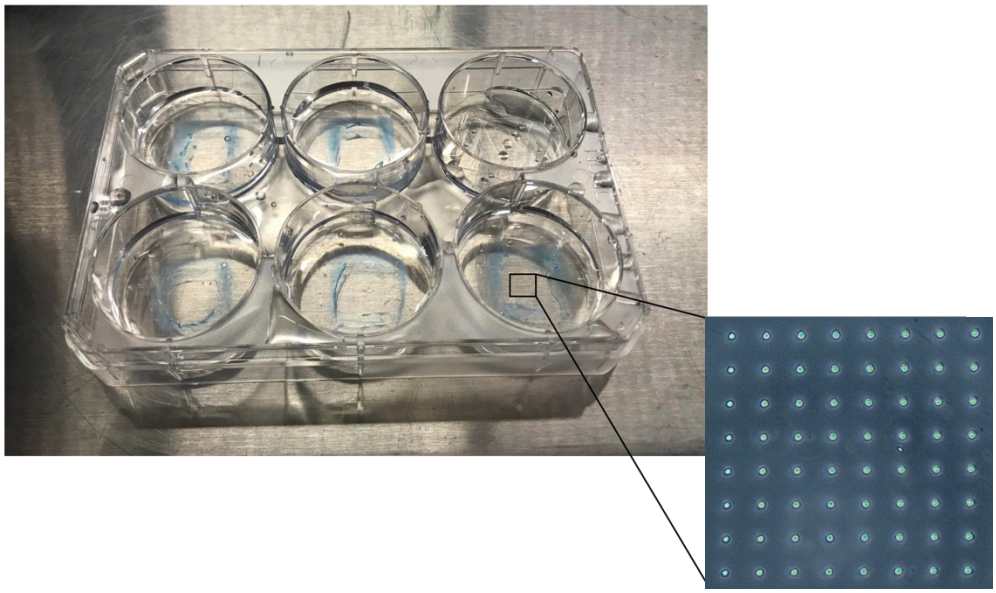

Figure 18 Washing AA-containing coverslips in serial dilutions of ethanol in distilled water after. The blue ring on each coverslip is the hydrophobic barrier drawn before printing.

Figure 19(A) shows the coverslips seeded with primary rat OPCs. Before adding OPCs, we reinforced the hydrophobic barrier to ensure the media would stay contained. After suspending the rat OPCs in media, we pipetted ~50 µL of the OPC-containing media onto each coverslip. We found it was critically important to avoid overfilling the coverslip; if the media began to leak out of the hydrophobic barrier, the surface tension from the water made the leak impossible to mend. As shown in **Figure 19(B)**, a common problem we initially encountered was poor cell viability. In a brightfield micrograph, axons should look like solid continuous lines; instead, when they look frayed and patchy like in **Figure 19(B)**, this is a sign of cell death. We found that this problem was a result of inadequate washing of the AAs after printing to remove unreacted resin – when the number of wash steps was increased from five to ten, we no longer observed this patchy axonal morphology. Therefore, there exists a trade-off between minimizing washing steps to prevent accidental AA toppling, but having sufficient washing so that the OPCs are still viable when plated.

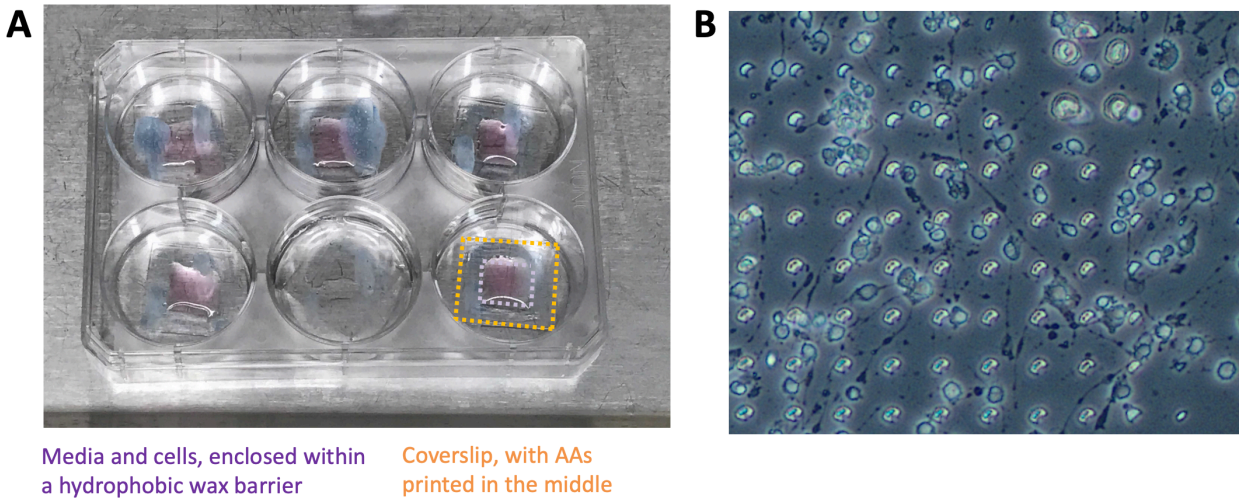

Figure 19 (A) Photograph of AAs on coverslips after being seeded with primary rat OPCs (B) Brightfield microscope image of cell death, indicative of insufficient AA washes after printing

After the AA washing and cell seeding steps were optimized, we cultured rat OPCs for seven days (which was a standard culture duration for all rat OPC studies), after which we fixed the cells and prepared the samples for TEM imaging. A key limitation of TEM is that its high resolution comes at the expense of having a narrow field of view. As shown in **Figure 20**, a given array of AAs had approximately 10000 vertical pillars, spanning a total area of 4 mm x 4 mm. However, the TEM field of view is approximately 15 µm x 15 µm, necessitating that we only take pictures of a very narrow subset of AAs.

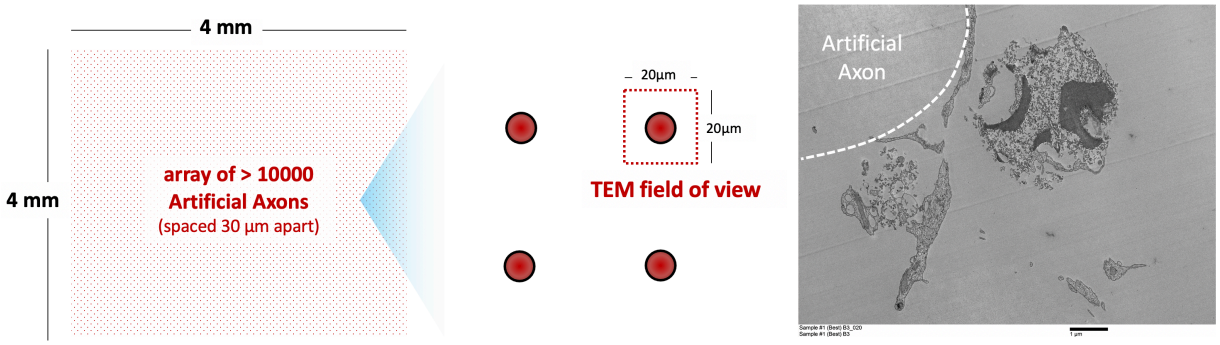

Figure 20 Mismatch between AA dimensions and the field of view of TEM image. Scale bar underneath the TEM image is 1 µm.

Our initial approach was to sample a random subset of 20 AAs and take images of any myelin around those pillars. However, a major limitation was that approximately half of all AAs are not ensheathed with any myelin at all (see **Figure 15**). Therefore, this random sampling approach typically resulted in TEM images like shown in **Figure 20**, where we would observe patches of membrane deposits that were not associated with any particular AA. Note that because the AAs were not conductive, they did not appear on the TEM image (although a possible solution is to embed metallic nanoparticles in the resin during printing, which *would* make the AAs visible in the future).

A common solution in TEM to mitigate this random search approach is to incorporate fiducial markers (henceforth called 'landmarks') into the sample. This way, one could *first* identify exactly which well-myelinated AAs to image, and then use those landmarks to navigate to those specific axons. Therefore, we printed AAs containing landmarks, resulting in the configuration shown in **Figure 21**. Instead of having a single homogeneous array of 10,000 axons, we printed the axons in a spaced-out, 3x3 arrangement. The top left tile of the 3x3 grid was left empty to orient the viewer. Each tile of the 3x3 grid had a landmark on the bottom-left corner, indicated by a pattern of large dots (numbered 2-8).

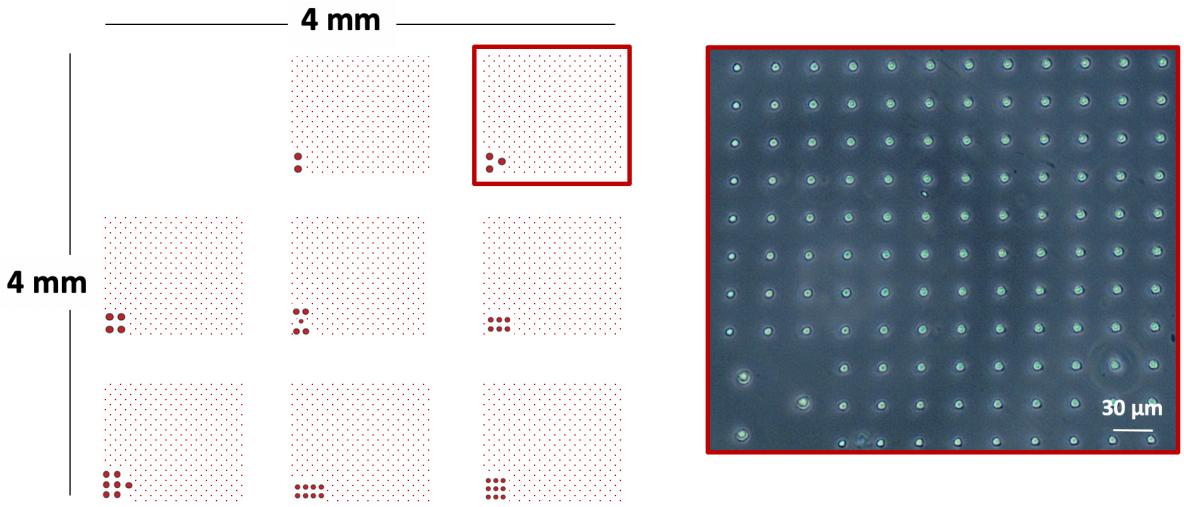

Figure 21 Schematic and brightfield micrograph of AA with fiducial marker

We then repeated the process as described above to wash and functionalize the AAs, and then seeded them with primary rat OPCs for seven days. On the seventh day, we fixed all cells, then we tested two approaches for imaging the AAs to pre-identify areas of promising myelin ensheathment. The first approach was to our standard method of confocal microscopy to identify regions of well-wrapped axons. Although this was a robust and reproducible method to find MBP+ regions, a potential downside is that preparing samples for immunofluorescence microscopy could potentially damage the membrane structure. Fluorescence microscopy requires that samples are first permeabilized in a detergent (e.g., Triton-X) to make the cell membranes permeable to antibodies. Therefore, although fluorescence microscopy will identify well-wrapped myelin, it is possible that the myelin will be degraded once visualized on TEM. The alternative approach to identifying well-wrapped AAs is to use phase contrast brightfield microscopy. However, myelin ensheathment is much harder to identify on phase contrast microscopy, therefore preserving membrane integrity comes at the expense of a more subjective approach to identify well-wrapped AAs. **Figure 22** summarizes the two alternative workflows for identifying regions of interest (ROIs) for transmission electron microscopy.

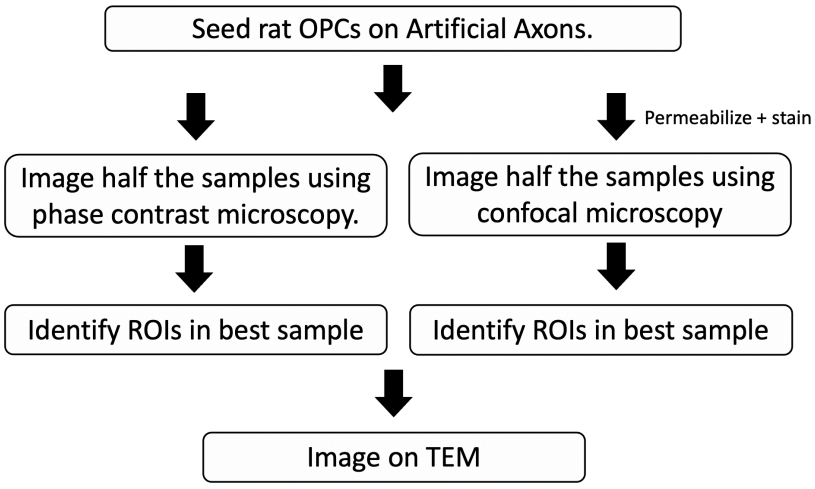

Figure 22 Two alternative workflows for identifying regions of interest (ROIs) for transmission electron microscopy (TEM)

As expected, confocal microscopy was a reliable approach for selecting ROIs. **Figure 23** shows an example confocal micrograph provided to the TEM imaging core. Each image has the landmark clearly in view, in addition to the exact position of which AA to image.

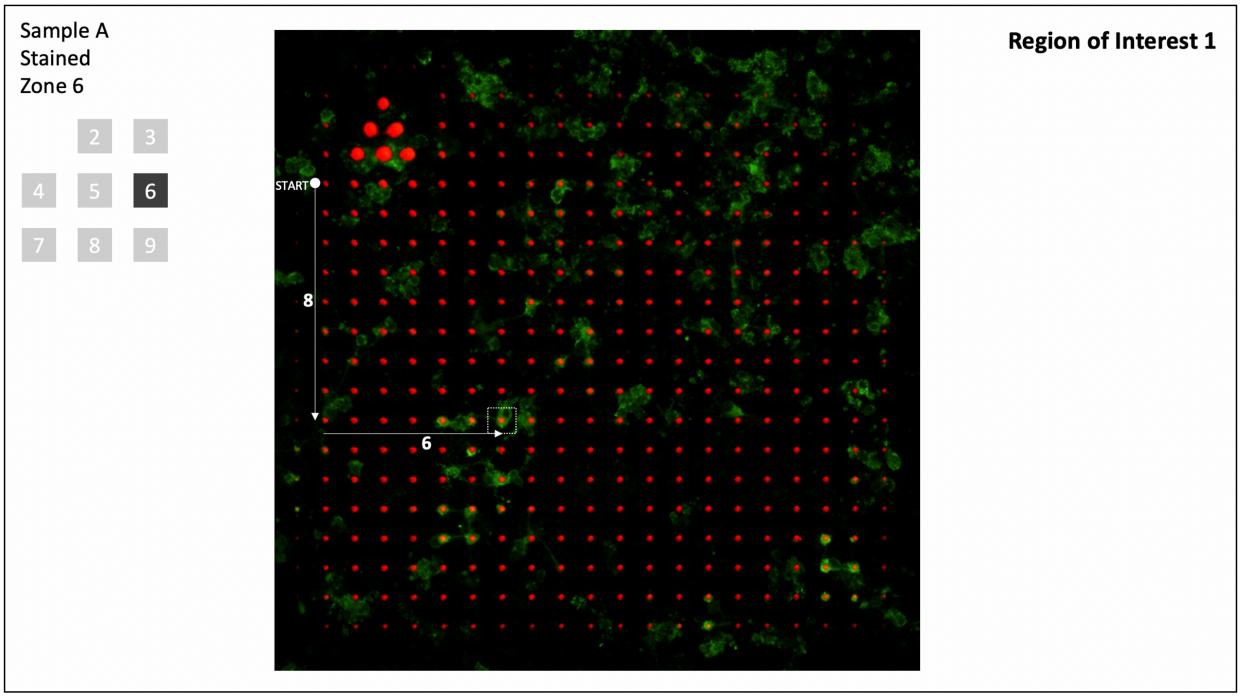

Figure 23 Example ROIs provided to transmission electron microscopy (TEM) core facilities

After identifying the ROIs on confocal microscopy, we used phase contrast microscopy to image the same samples to identify whether any visual patterns could help to distinguish the well-myelinated regions. Unfortunately, it was challenging to identify any compelling visual signatures, apart from a subjective thickening of the AA border wall. **Figure 24** shows a representative phase contrast micrograph and two hypothesized regions of well-wrapped AAs, illustrating the challenge of using this approach to identify AAs.

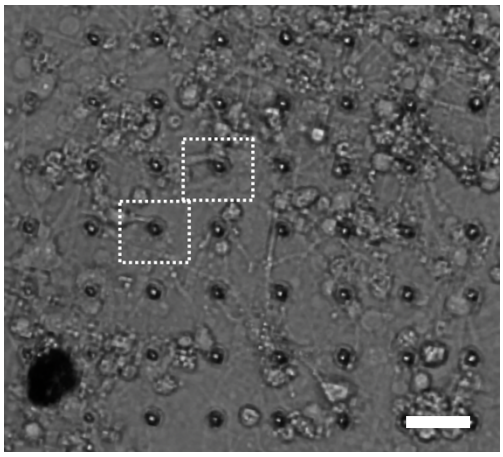

Figure 24 Representative phase contrast micrograph of AAs. The highlighted boxes indicate attempts to subjectively identify regions of well-wrapped AAs. Scale bar is 30 μm.

We identified 10 ROIs using both approaches and imaged on TEM. We found that phase contrast microscopy was ultimately unsuccessful in identifying ROIs. A representative TEM image is shown in **Figure 25**, showing no discernible myelin wrapping around any structure. Also, there is a surprising amount of apoptotic 'blebbing' in these images, which suggests that the fixation process may have been too harsh and damaged cell morphology. However, these images do show that the cell membrane was mostly preserved, indicated by the solid lines on the perimeter of each structure.

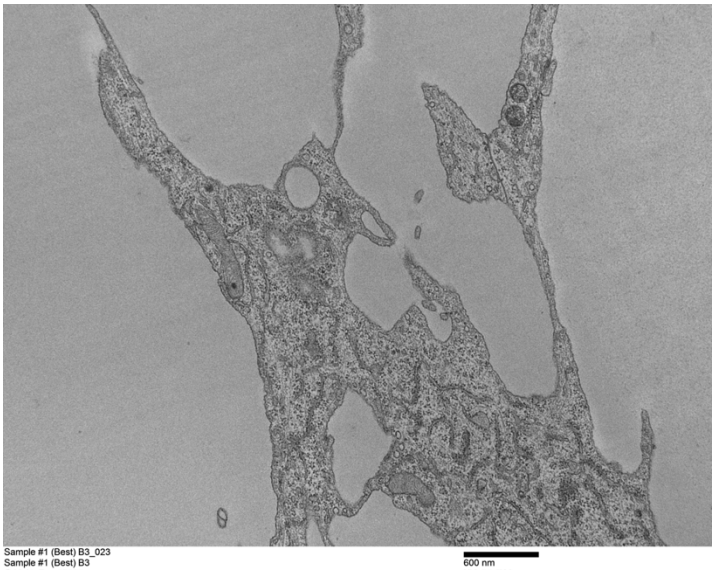

Figure 25 Transmission electron micrograph of a ROI identified by phase contrast microscopy. Scale bar is 600 nm.

In contrast, the ROIs identified on confocal microscopy were more promising, and indicated membrane segments were wrapped around a circular structure (**Figure 26**). Although these images did not show evidence of myelin compaction, they did display the microtubular bundles in oligodendrocytes that were ensheathed around the AAs. These images also indicated that membrane structure was indeed compromised by permeabilization, evident in the dotted outlines around the cell circumference, and the overall patchy appearance of the cells compared to in **Figure 25**.

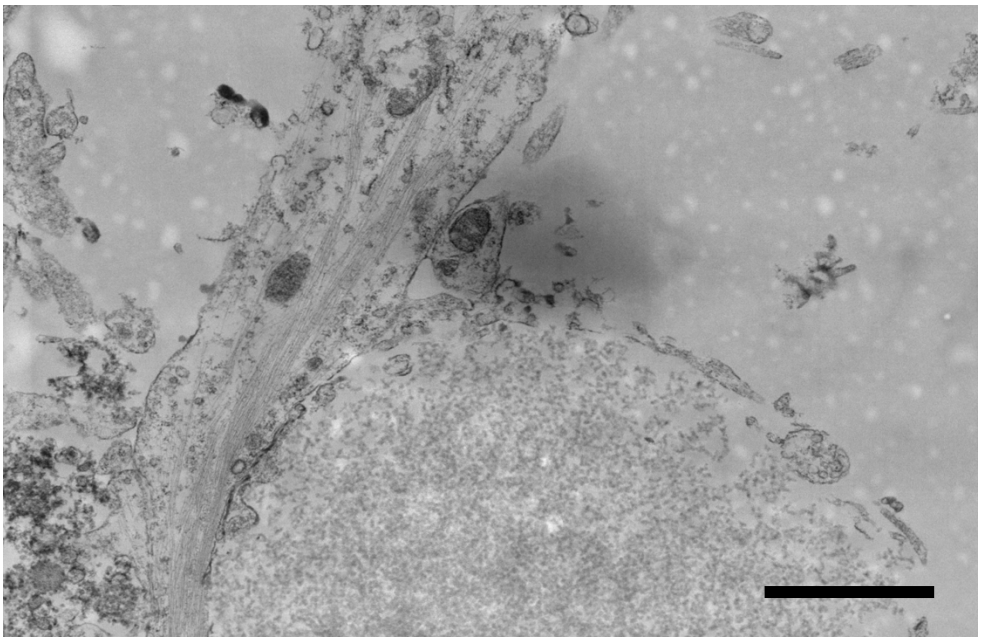

Figure 26 Transmission electron micrograph of a ROI identified by confocal microscopy. Scale bar is 600 nm.

In sum, we made incremental progress towards using transmission electron microscopy to image myelin ultrastructure, although at present there is no evidence of compact myelin. Here, we propose some future steps for using TEM to image. First, we propose culturing the cells in chamber slides, which have removable walls that are specifically designed for resin embedding. This can mitigate some of the challenging sample handling of using individual coverslips, such as coverslip floating (leading to AA collapse) and the hydrophobic seal breaking. The HR-3DP is also amenable to printing directly into the bottom of a functionalized glass chamber slide. Second, we recommend

seeding the OPCs for longer than seven days. It is possible that myelin compaction *could* eventually be observed if left over a longer time span. Finally, these results indicated that phase contrast microscopy does preserve membrane integrity, while confocal microscopy is indeed better at identifying ROIs. One approach could be to use genetically engineered OPCs that express a fluorescent MBP reporter – therefore, fluorescence can be observed in the absence of any cell permeabilization steps. Another promising avenue is to explore fluorescent labels like Fluoromyelin, which can bind to myelin directly without the requirement for permeabilization. Overall, TEM combined with the fiduciary markers still represents a promising approach for observing the potential of compact myelin around AAs, although no such evidence was found in these experiments.

2.7 Materials and Methods

Fabrication of Artificial Axons (AAs)

Artificial axons were fabricated directly in 96-well plates, using a projection microstereolithography setup. To vary axon stiffness (material Young's modulus) the resins were prepared with varying ratios of 1,6-hexanediol diacrylate (HDDA) (Sigma-Aldrich) and 4-arm PEG acrylate (starPEG) (JenKem) monomers, at mass ratios of 3:1, 2:1, and 1:1. Fabrication details are in the appendix. The resins were pipetted into the wells of 96-well plates and exposed to UV light using our custom made projection microstereolithography setup[4]. Projecting the UV light onto the resin through the digital mask caused the liquid monomer resin to polymerize into solid vertical pillars that match the geometric pattern of the mask. The shape of the mask, the composition of the resin, the UV exposure duration, and the UV exposure intensity could all be modified to independently tune the Young's modulus, diameter, and spacing of the axons. Prior to introduction of rat oligodendrocyte progenitor cells, the AAs were functionalized with poly-D-ornithine (Sigma-Aldrich) (50 μg/mL) followed by incubation with laminin (Gibco) (20 μg/mL) to facilitate cell adhesion. The completed AA plates were stored in PBS at 4°C and warmed to 37°C the day of OPC seeding.

Immunostaining

Cells were fixed with 4% paraformaldehyde (Electron Microscopy Sciences), washed three times with PBS, and permeabilized with 0.1% v/v Triton X-100 and 5% v/v goat serum in PBS for 10 minutes at room temperature. Then, cells were washed three times in PBS and blocked for 1 hour in 5% v/v goat serum in PBS for 1 hour at room temperature. Cells were incubated in primary antibody (rat anti-MBP, BioRad, 1:200 dilution) for 24 hours at 4°C. Next, cells were washed three times in PBS and incubated with secondary antibody (Alexa-Fluor-647 goat anti-rat, Thermo Fisher, 1:200 dilution) for 1 hour at room temperature. Cells were then washed three times in PBS and incubated with DAPI (Thermo Fisher, 1:1000) dilution for 5 minutes. Finally, cells were washed once more and stored in PBS at 4°C.

Fluorescence imaging

Stained samples were imaged under three fluorescent channels (Alex-Fluor 647 for MBP+ myelin, rhodamine for AAs, DAPI for nuclei) using a confocal microscope (Olympus, FluoView 3000) at 20x

air lens. For each well of the 96-well plate, eight fields of view were imaged; at each one, a confocal stack image was taken consisting of 8 *z*-slices separated by a step size of 2 μm. Collectively, ~1 million AAs were imaged and analyzed per well. Image analysis scripts are provided in the Appendices.

2.8 References

1. Chia, H. N. & Wu, B. M. Recent advances in 3D printing of biomaterials. 1–14 (2015) doi:10.1186/s13036-015-0001-4.
2. Zein, I., Hutmacher, D. W., Tan, K. C. & Teoh, S. H. Fused deposition modeling of novel scaffold architectures for tissue engineering applications. *Biomaterials* **23**, 1169–1185 (2002).
3. Byun, D. 3D printing of high-resolution PLA-based structures by hybrid electrohydrodynamic and fused deposition modeling techniques. (2016) doi:10.1088/0960-1317/26/2/025015.
4. Espinosa-Hoyos, D., Du, H., Fang, N. X. & Van Vliet, K. J. Poly(HDDA)-Based Polymers for Microfabrication and Mechanobiology. *MRS Adv.* **2**, 1315–1321 (2017).
5. Bertsch, A., Jiguet, S., Bernhard', P. & Renaud, P. *Microstereolithography: a Review*. *Mat. Res. Soc. Symp. Proc* vol. 758 (2003).
6. Gong, H., Beauchamp, M., Perry, S., Woolley, A. T. & Nordin, G. P. Optical approach to resin formulation for 3D printed microfluidics. *RSC Adv.* **5**, 106621–106632 (2015).
7. Gong, H., Bickham, B. P., Woolley, A. T. & Nordin, G. P. Custom 3D printer and resin for 18 μm × 20 μm microfluidic flow channels. *Lab Chip* **17**, 2899–2909 (2017).
8. Miri, A. K. *et al.* Microfluidics-Enabled Multimaterial Maskless Stereolithographic Bioprinting. *Adv. Mater.* **30**, (2018).
9. Zhang, Y. F. *et al.* Miniature Pneumatic Actuators for Soft Robots by High-Resolution Multimaterial 3D Printing. *Adv. Mater. Technol.* **4**, (2019).
10. Espinosa-Hoyos, D. *et al.* Engineered 3D-printed artificial axons. *Sci. Rep.* **8**, 1–13 (2018).
11. Yuan, C. *et al.* Ultrafast Three-Dimensional Printing of Optically Smooth Microlens Arrays by Oscillation-Assisted Digital Light Processing. *ACS Appl. Mater. Interfaces* **11**, 40662–40668 (2019).
12. Martin, J. J., Fiore, B. E. & Erb, R. M. Designing bioinspired composite reinforcement architectures via 3D magnetic printing. *Nat. Commun.* **6**, 1–7 (2015).
13. Yang, Y. *et al.* 3D-Printed Biomimetic Super-Hydrophobic Structure for Microdroplet Manipulation and Oil/Water Separation. *Adv. Mater.* **30**, 1–11 (2018).
14. Kim, W. J. & Kim, G. H. An intestinal model with a finger-like villus structure fabricated using a bioprinting process and collagen/SIS-based cell-laden bioink. *Theranostics* **10**, 2495–

2508 (2020).

15. Sun, C., Fang, N., Wu, D. M. & Zhang, X. Projection micro-stereolithography using digital micro-mirror dynamic mask. *Sensors Actuators, A Phys.* **121**, 113–120 (2005).
16. Zheng, X. *et al.* Ultralight, ultrastiff mechanical metamaterials. *Science (80-.).* **344**, 1373–1377 (2014).
17. Segel, M. *et al.* Niche stiffness underlies the ageing of central nervous system progenitor cells. *Nature* **573**, 130–134 (2019).
18. Lourenço, T. *et al.* Modulation of oligodendrocyte differentiation and maturation by combined biochemical and mechanical cues. *Sci. Rep.* **6**, (2016).
19. Urbanski, M. M., Brendel, M. B. & Melendez-Vasquez, C. V. Acute and chronic demyelinated CNs lesions exhibit opposite elastic properties. doi:10.1038/s41598-018-37745-7.
20. Segel, M. *et al.* Niche stiffness underlies the ageing of central nervous system progenitor cells. *Nature* **573**, 130–134 (2019).
21. Espinosa-Hoyos, D. *et al.* Mechanosensitivity of Human Oligodendrocytes. *Front. Cell. Neurosci.* (2020) doi:10.3389/fncel.2020.00222.
22. Jagielska, A. *et al.* Mechanical environment modulates biological properties of oligodendrocyte progenitor cells. *Stem Cells Dev.* **21**, 2905–2914 (2012).
23. Kagami, M., Yamashita, T. & Ito, H. Light-induced self-written three-dimensional optical waveguide. *Appl. Phys. Lett.* **79**, 1079–1081 (2001).
24. Kewitsch, A. S. & Yariv, A. Nonlinear optical properties of photoresists for projection lithography. *Appl. Phys. Lett.* **68**, 455–457 (1996).
25. Miwa, M., Juodkazis, S., Kawakami, T., Matsuo, S. & Misawa, H. Femtosecond two-photon stereo-lithography. *Appl. Phys. A Mater. Sci. Process.* **566**, 561–566 (2001).
26. Aloui, F., Lecamp, L., Lebaudy, P. & Burel, F. Refractive index evolution of various commercial acrylic resins during photopolymerization. *Express Polym. Lett.* **12**, 966–971 (2018).
27. Samusjew, A. *et al.* Inkjet Printing of Soft, Stretchable Optical Waveguides through the Photopolymerization of High-Profile Linear Patterns. *ACS Appl. Mater. Interfaces* **9**, 4941–4947 (2017).
28. Zhang, J. & Saravanamuttu, K. The dynamics of self-trapped beams of incoherent white light in a free-radical photopolymerizable medium. *J. Am. Chem. Soc.* **128**, 14913–14923 (2006).

29. Tolstik, E., Romanov, O., Matusevich, V. Y., Tolstik, A. L. & Kowarschik, R. M. Self-trapping waveguiding structures in nonlinear photorefractive media based on Plexiglas with phenanthrenequinone molecules. *Opt. Model. Des. II* **8429**, 84290W (2012).
30. Tolstik, E., Romanov, O., Matusevich, V., Tolstik, A. & Kowarschik, R. Formation of self-trapping waveguides in bulk PMMA media doped with Phenanthrenequinone. *Opt. Express* **22**, 3228 (2014).
31. Hsiao, Y.-N. Analyses on physical mechanism of holographic recording in phenanthrenequinone-doped poly(methyl methacrylate) hybrid materials. *Opt. Eng.* **43**, 1993 (2004).
32. Lin, S. H. Experimental characterization of phenanthrenequinone-doped poly(methyl methacrylate) photopolymer for volume holographic storage. *Opt. Eng.* **42**, 1390 (2003).
33. Becker, M. R. *et al.* Waveguide optical properties of polystyrene doped with p-nitroaniline derivatives. *Opt. Mater. (Amst).* **32**, 1526–1531 (2010).
34. Kudo, H., Yamamoto, M., Nishikubo, T. & Moriya, O. Novel materials for large change in refractive index: Synthesis and photochemical reaction of the ladderlike poly(silsesquioxane) containing norbornadiene, azobenzene, and anthracene groups in the side chains. *Macromolecules* **39**, 1759–1765 (2006).
35. Paul, S. *et al.* Channel Waveguide Applications. *Texte - Rev. Crit. Theor. Litt.* **288**, 150–154 (1996).
36. Morim, D. R. *et al.* Opto-chemo-mechanical transduction in photoresponsive gels elicits switchable self-trapped beams with remote interactions. *Proc. Natl. Acad. Sci. U. S. A.* **117**, 3953–3959 (2020).
37. Kleine, T. S. *et al.* Refractive Index Contrast Polymers: Photoresponsive Systems with Spatial Modulation of Refractive Index for Photonics. *ACS Macro Lett.* **9**, 416–421 (2020).
38. Espinosa-Hoyos, D., Jagielska, A., Du, H., Fang, N. X. & Van Vliet, K. J. Engineered 3D-Printed Artificial Axons. vol. 1 (2018).
39. Tolstik, E., Kashin, O., Matusevich, V. & Kowarschik, R. Broadening of the light self-trapping due to thermal defocusing in PQ-PMMA polymeric layers. *Opt. Express* **19**, 2739 (2011).
40. Yang, M. *et al.* Additive manufacturing of high aspect-ratio structures with self-focusing photopolymerization. *Light Adv. Manuf.* **3**, 542 (2022).
41. Schneider, C. A., Rasband, W. S. & Eliceiri, K. W. *NIH Image to ImageJ: 25 years of Image Analysis HHS Public Access. Nat Methods* vol. 9 (2012).

42. Baumann, N. & Pham-Dinh, D. *Biology of Oligodendrocyte and Myelin in the Mammalian Central Nervous System*. http://physrev.physiology.org (2001).
43. Pennycook, S. J. Transmission Electron Microscopy: Overview and Challenges. 627–633 (2003) doi:10.1063/1.1622537.

3. Modeling how the biological microenvironment influences myelin ensheathment

3.1 Mechanosensitivity of oligodendrocytes

A growing body of evidence demonstrates that oligodendrocytes and OPCs are sensitive to external mechanical cues[1] including ECM stiffness (and more broadly the stiffness of the material to which OPCs adhere)[2–6], mechanical strain[7], macromolecular crowding, and physical confinement[8,9].

In a prior study by Jagielska et al., primary rat OPCs were cultured on polyacrylamide (PAA) gels, with Young's moduli ranging from E = 0.1 to 70 kPa, as measured by atomic force microscopy-enabled indentation. OPC death was lowest at stiffnesses in the physiological range (E = 0.7 kPa), and viability was decreased at stiffnesses above and below this physiological level (**Figure 27 A**). Similar to viability, proliferation was highest on gels of E = 0.7 kPa and was lower at all other substrata stiffnesses (**Figure 27 B**). Together, these results show that OPCs survival and proliferation are both maximized at intermediate stiffness values that closely resemble the *in vivo* environment. Similarly, OPC migration was also maximized at intermediate substratum stiffness.

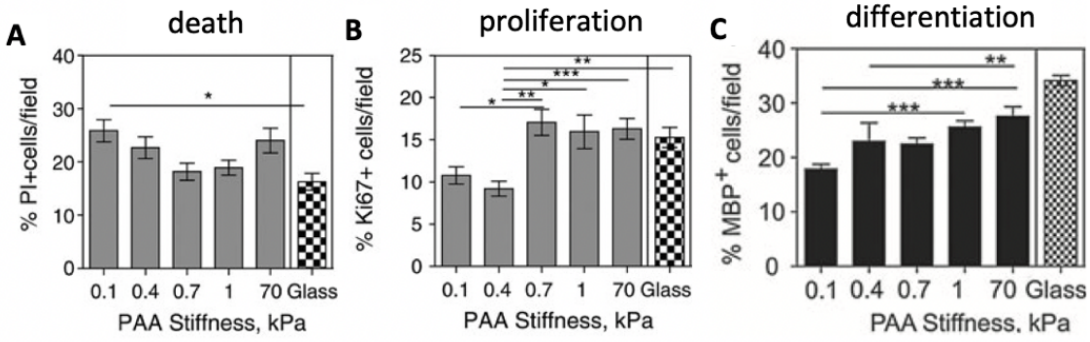

Figure 27 Primary rat OPC (a) cell death, (b) proliferation, and (c) differ enation are affected by the Young's elastic moduli of the PAA substrata[6]. Adapted from Jagielska et al. (2012)

In terms of how tissue stiffness can affect OPC differentiation, different studies have yielded contradictory results. Some groups report that stiffer substrata enhance OPC differentiation[2,4,10], whereas others report the opposite effect[6,11]. One possible explanation for this conflict is that each group studied very different ranges of elastic modulus, in most cases using materials that were significantly stiffer than brain tissue. It is possible that OPCs respond non-monotonically to tissue stiffness[12,13], and that capturing their 'true' behavior will require probing OPCs under more mechanically representative environments. Furthermore, most existing studies probe how biophysical cues influence differentiation, using MBP expression as a surrogate for OPC maturation. However, differentiation is only a prerequisite to myelination; therefore, our work aims to explore how biophysical cues influence not only OPC differentiation but also their myelination potential.

Other work by Jagielska et al. has shown that mechanical strain in the culture substrata can lead to global changes in gene expression[7]. Specifically, OPCs show upregulated expression of genes associated with OPC differentiation, in addition to genes associated with axon-oligodendrocyte interactions. In addition, oligodendrocytes are sensitive to axon geometry, selecting specifically for axons with diameters above 0.2 μm before depositing myelin[14]. In one study, researchers fabricated axon mimics of varying diameters using electrospun polymer fibers. OPCs seeded on the lowest-diameter axons (0.5-1 μm) generally formed fewer sheaths than those on higher-diameter axons (1-2 μm or 2-4 μm). Interestingly, across all fiber diameters, spinal cord oligodendrocytes formed longer sheath lengths than cortical oligodendrocytes, which suggests that myelin sheath length is both an intrinsic property of oligodendrocytes but is also subject to modulation by environmental cues. In other words, based on their *in vivo* origin, different oligodendrocytes may have different propensities to form long or short myelin sheaths, but this behavior is plastic and can be modified by cues like axon diameter.

Oligodendrocyte mechanosensitivity is likely mediated by integrin interactions with the extracellular matrix[15,16], which can be transduced to the nucleus through the

linker of nucleoskeleton and cytoskeleton (LINC) complex[17]. The complex is composed of two protein domains, one that spans the inner nuclear membrane, and one that spans the outer nuclear membrane. When the cytoskeleton experiences mechanical forces from the extracellular environment (e.g., through changes to integrin binding), those forces can be directly transmitted through the LINC complex to physically alter chromatin structure, in turn affecting gene regulation and chromosome organization. This represents a general mechanism by which many cell types, not just oligodendrocytes, transduce signals from their extracellular environment.

3.2 Biophysical changes in myelin lesions

The sensitivity of OPCs to biophysical cues may play important roles in myelin pathology and neurodegenerative diseases. For example, neuroimaging data from human patients show correlations between neurological disease states, such as progressive multiple sclerosis (MS), and changes in the structural integrity and mechanical properties of brain tissue[18,19]. These findings are supported by murine models of demyelination, in which the Young's modulus *E* of brain parenchyma decreased in response to acute demyelination from 240 Pa to 120 Pa, signifying a stiffness reduction correlated with disease progression[20,21]. These studies used a standard cuprizone model to induce acute demyelination. Cuprizone is an orally administered drug that induces oligodendrocyte apoptosis and activates both microglia and astrocytes. After 12 weeks of cuprizone administration, magnetic resonance elastography (MRE) maps of the brain showed significantly decreased brain stiffness. This raises the question of whether decreased brain stiffness may actually play a causal role in myelination diseases.

In additional to tissue stiffness, other biophysical cues such as axon diameter and spacing may play important roles in oligodendrocyte biology and pathology. Under healthy conditions, axon diameter in the CNS can vary in diameter from 0.1-5.0 μm[22,23]. Magnetic resonance imaging (MRI) data has shown axon swelling to be a major

pathological feature in chronic MS[24], and a similar case of increased axonal diameter was reported for amyotrophic lateral sclerosis (ALS)[25]. Furthermore, axonal injury and loss of axon density (number of axons per unit area or volume) is a hallmark of progressive MS[26], especially for chronically demyelinated axons. An open question is whether these biophysical changes simply act as correlative biomarkers or contribute to disease progression. In other words, do changes in axon diameter and brain parenchyma stiffness occur as secondary byproducts of myelination pathology, or do they actually change the propensity of oligodendrocytes to myelinate?

3.3 Fabrication and characterization of AAs with tunable Young's moduli

AAs provide a promising platform for investigating these questions about causality vs. correlation, since the diameter, stiffness, and interaxonal spacing of AAs can be independently tuned. Chapter 2 described how axon geometry (including diameter and density) can be independently varied by changing the digital mask and the fabrication conditions (e.g., light intensity, and exposure time).

Here, we also varied the Young's elastic moduli of the AAs by changing the ratio of 4-arm PEG acrylate (starPEG) and 1,6-hexanediol diacrylate (HDDA). As discussed previously, AAs are fabricated via free-radical chain growth polymerization. When a photoinitiating species in the resin is exposed to UV light, it undergoes homolytic fission to produce a radical (unpaired electron-containing) product. This free radical can activate any of the C=C bonds in starPEG or HDDA to initiate polymer chain propagation. During polymerization, HDDA can act as a crosslinker between adjacent starPEG units. Therefore, increasing the ratio of HDDA:starPEG increases the crosslinking density of the resultant polymer (**Figure 28**), which should in turn increase the Young's elastic modulus *E* of the AA.

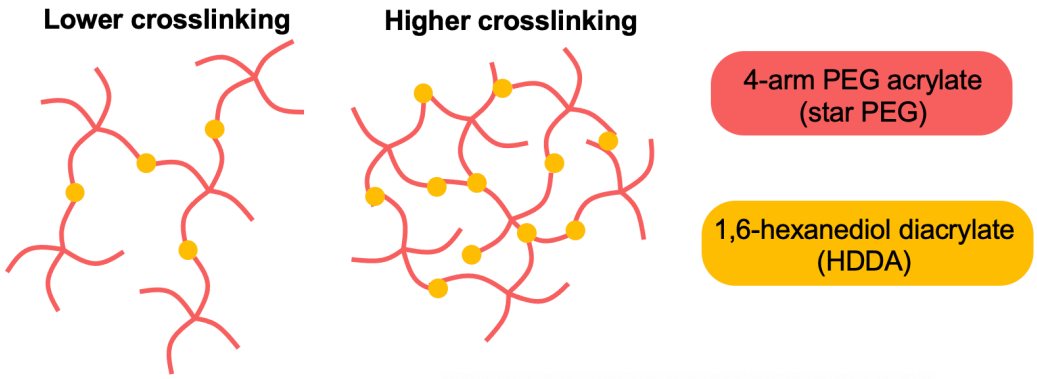

Figure 28 Schematic of polymer network structure formed from different starting ratios of starPEG vs. HDDA. Increasing the HDDA:starPEG ratio increases the crosslinking density of the resultant network.

We characterized the Young's elastic moduli of the resultant AAs using atomic force microscopy (AFM)-enabled indentation. In brief, an atomic force microscopy consists of a sharp tip mounted at the end of a compliant cantilever. The cantilever and the tip are slowly lowered over a sample until it just makes contact. As the tip is further lowered into the sample, the cantilever will deflect, which is measured as a voltage change in the detector. An important part of AFM calibration is setting the correspondence between the deflection of the cantilever and the electrical signal measured by the detector. After the cantilever deflects to a predetermined set point, it is retracted, and the deflection of the cantilever is measured as a function of its vertical *z* position (for which the raw data is the piezoelectric signal from the cantilever). The raw data collected at this stage can be visualized as a graph of cantilever deflection vs. *z* position.

To infer the stiffness of the sample being indented, the deflection of the cantilever is converted to a force measurement. Modeling the cantilever as an elastic beam, we can assume that the force exerted by the sample onto the cantilever is proportional to the cantilever deflection[27,28]. Therefore, the deflection vs. position graph can be converted into a force vs. position graph. Finally, the force vs. position data can be fitted to a Hertz elastic model to calculate the Young's elastic modulus of the sample being indented[28],

using an analysis script adapted from Farruggio et al in the Van Vliet Group for Material Chemomechanics.

We fabricated AAs at three different HDDA:starPEG mass ratios, namely 3:1, 2:1, and 1:1. For each resin chemistry, we 3D-printed AAs onto functionalized glass coverslips (following the process described in Chapter 2. We used coverslips instead of printing into well plates because the walls of the well plate would have impeded access to the AAs by the AFM tip and cantilever. Each sample consisted of an array of approximately 10,000 AAs, each with 7 μm diameter and 50 μm interaxonal spacing. We used 7 μm-diameter axons (instead of a lower diameter) to minimize the role of edge effects in atomic force microscopy. Here, we also note that the sample yield during 3D printing was 100%. In contrast, previous attempts to fabricate AAs with a 1:1 HDDA: starPEG (using the first-generation printer described in Chapter 2) was untenable, because almost all the samples would be damaged during the delicate handling process. After printing, we washed the AAs in ethanol and submerged them in PBS for 48 hours. Since the AA material contains hydrophilic starPEG, the AA behaves as a hydrogel and can absorb water (although the physical dimensions of the AAs do not change significantly after water absorption). Since the OPCs are in contact with hydrated AAs, it was important to also hydrate the AAs to ensure that the stiffness measured by AFM was representative of that experienced by the cells.

For each sample, we indented between 30 and 40 separate AAs and collected force-depth curves for each one. In order of descending HDDA:starPEG ratio, the E of the three materials were found to be 13,000 Pa ± 64 Pa, 780 Pa ± 11 Pa, 98 Pa ± 5 Pa respectively. This trend was consistent with predictions since HDDA functions as a crosslinker between the much larger starPEG molecules in the polymer network. Therefore, increasing the HDDA:starPEG ratio represents an increase in crosslinking density and therefore a stiffer polymerized AA material.

Material	HDDA	:	starPEG
X	3	:	1
Y	2	:	1
Z	1	:	1

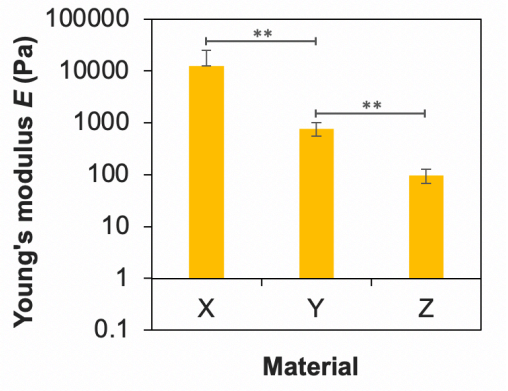

Figure 29 Young's elastic modulus *E* measured for AAs with HDDA:starPEG ratios of 3:1, 2:1, and 1:1. Asterisks indicate $p < 0.01$.

3.4 3D quantification of myelin wrapping around AAs

The work presented thus far in this thesis demonstrates that we can use the high-resolution 3D printer (HR-3DP) to fabricate AAs with independently tunable diameter, interaxonal spacing, and Young's elastic modulus. This provides a platform for investigating whether each of these variables could play a causal role in affecting an oligodendrocyte's propensity to myelinate. The standard approach to quantify 'myelination' from *in vitro* models is to quantify MBP expression as a proxy for myelin ensheathment. However, the differentiation of OPCs into MBP+ oligodendrocytes alone is necessary but not sufficient for myelin ensheathment. Here, we present an image analysis algorithm for quantifying myelin ensheathment in 3D.

First, we incorporate a fluorescent dye (rhodamine inner salt) in the AA resin so that each axon is fluorescent. After staining the oligodendrocytes for MBP, we image the AAs using confocal microscopy, which collects the fluorescence image across multiple vertical *z*-stacks. At each *z*-stack, we generated a binary mask for the rhodamine-stained AA and the myelin channel. For each AA mask, we traced a 1 pixel-thick outline around each AA. We then generated an 'overlap mask' by comparing the AA outline tracing with the corresponding pixels in the myelin mask (**Figure 30**).

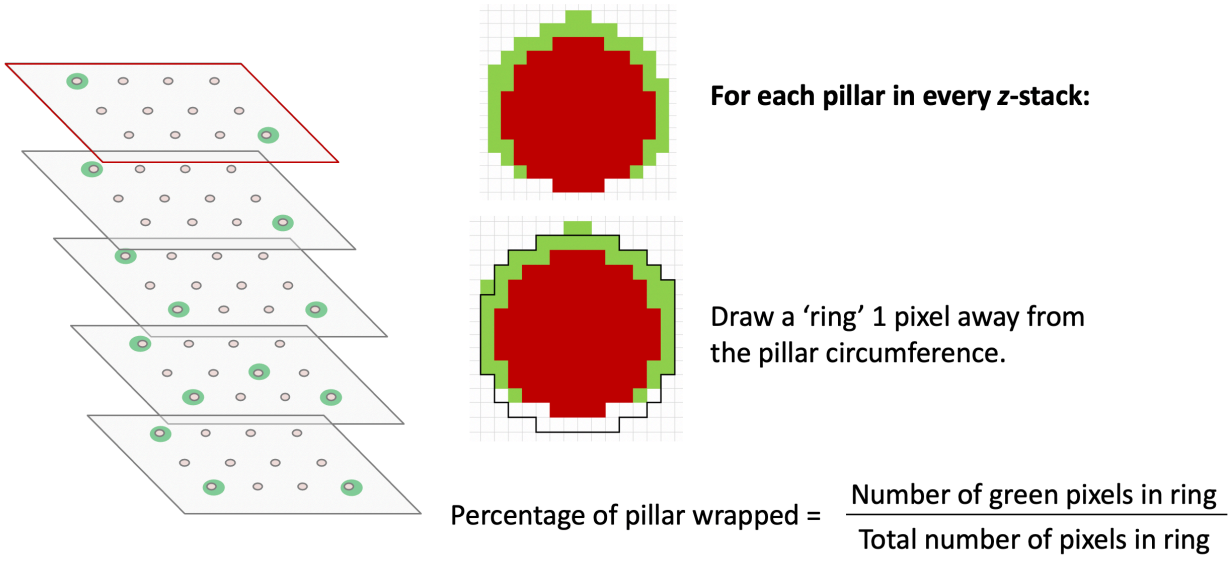

Figure 30 Schematic of generating an 'overlap mask' by tracing a 1 pixel-thick outline around each AA and identifying regions of pixel overlap with the MBP channel

Pixels in the outline that were also myelin-positive were assigned a value of 255 in the overlap mask, and outline pixels with no corresponding myelin were assigned a value of 0 in the overlap mask. Therefore, the overlap mask is a binary image that captures the fractional circumference of each AA with myelin membrane around it. Finally, we compared the overlap masks across all *z*-stacks, thus aggregating the myelin coverage of each discrete ensheathed segment along the length of each AA (**Figure 31**).

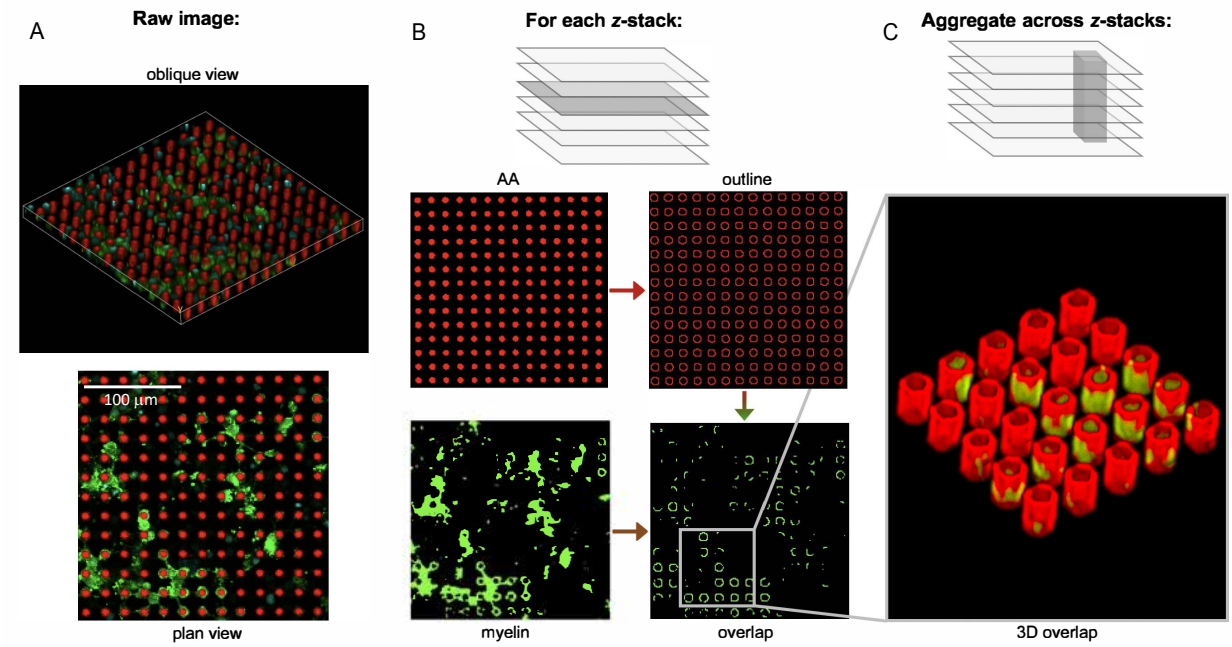

Figure 31 (A) Confocal micrograph of myelin basic protein (green) wrapped around artificial axons (red) (B) Top-down binary mask generated for each *z*-stacks, used to generate an overlap mask between the pillar and myelin channels (C) Aggregated overlap masks across all *z*-stacks to quantify wrapping across the three-dimensional extent of each axon.

Figure 32 shows the underlying data structure used to accomplish this analysis. Every pillar is given a unique numerical identifier to trace which red circle in each *z*-stack corresponds to which AA. Then, at each *z*-stack, we tracked whether each pixel in the circumference contains myelin (coded as the value 255) or not (coded as the value 0).

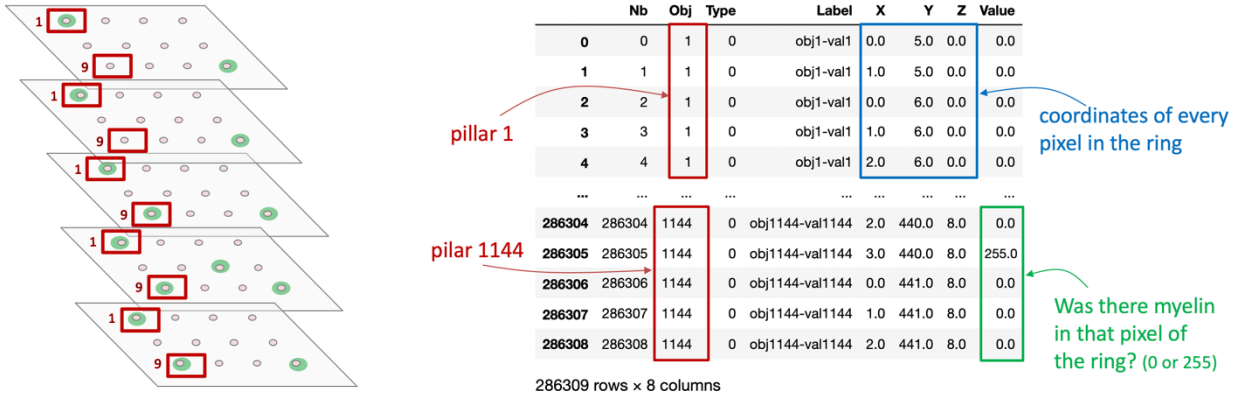

	Nb	Obj	Type	Label	X	Y	Z	Value
0	0	1	0	obj1-val1	0.0	5.0	0.0	0.0
1	1	1	0	obj1-val1	1.0	5.0	0.0	0.0
2	2	1	0	obj1-val1	0.0	6.0	0.0	0.0
3	3	1	0	obj1-val1	1.0	6.0	0.0	0.0
4	4	1	0	obj1-val1	2.0	6.0	0.0	0.0
...	...	...	...	...	...	...	...	...
286304	286304	1144	0	obj1144-val1144	2.0	440.0	8.0	0.0
286305	286305	1144	0	obj1144-val1144	3.0	440.0	8.0	255.0
286306	286306	1144	0	obj1144-val1144	0.0	441.0	8.0	0.0
286307	286307	1144	0	obj1144-val1144	1.0	441.0	8.0	0.0
286308	286308	1144	0	obj1144-val1144	2.0	441.0	8.0	0.0

Figure 32 Underlying data structure of the image analysis algorithm, where each AA pillar is assigned a unique identifier. Around the circumference of each axon, we track whether each pixel contains MBP+ wrapping or not (255 vs. 0).

We defined an AA as being 'fully wrapped' if there was a contiguous >6 µm ensheathed segment length in which the AA was >80% wrapped in all of those *z*-stacks. This image analysis pipeline uniquely enabled us to obtain 3D readouts of myelin wrapping. We defined a 'wrapping index' parameter, which was the number of AAs exhibiting at least one fully wrapped segment, divided by the total number of cells in the field of view. We determined the total oligodendrocyte number by counting the number of DAPI+ nuclei observed. Normalizing by cell number in this way accounted for subtle variations in cell density between different regions of the well. Whereas wrapping index is a measure of the *number* of AAs, we also quantified the *length* of myelin sheaths on those wrapped AAs.

3.5 How axon stiffness, diameter, and spacing affect myelin wrapping

We fabricated AAs of three different magnitudes of stiffness, of diameter, and of spacing, and quantified the resulting myelin ensheathment by rat oligodendrocytes as a parameter we termed wrapping index, WI. OPCs were isolated from neonatal rat brains and seeded on AAs within 96-well plates for 14 days with differentiation induced by T3 at concentration 1 µM, after which we fixed and stained for myelin basic protein (MBP), a marker of differentiated oligodendrocytes and also a major component of myelin itself.

Figure 33 show the variation of myelin wrapping by oligodendrocytes as a function of AA stiffness, diameter, or spacing. Importantly, we measured two attributes of myelin wrapping. The first is the previously defined WI, which indicates the *number* of AAs wrapped. We also separately quantified the *length* of the imaged myelin sheaths, calculated by determining the number of adjacent *z*-stacks with >80% wrapping.

Figure 33 B shows that increasing axon stiffness led to an increase in the WI, meaning that on average more AAs are being wrapped per OPC (left panel). The average length of myelin segment shows slightly decreasing trend with the increasing stiffness, although the differences between the individual tested conditions were not statistically significant (right panel). This raises the possibility that the decrease in stiffness local to OPCs or oligodendrocytes in demyelinating contexts[18,20]could possibly decrease the intrinsic propensity of oligodendrocytes to myelinate axons. Based on these data alone, this is still just a speculative hypothesis; furthermore, an important caveat is that in this experiment we vary stiffness on an *axon*, whereas previous data report on more global changes in stiffness of the brain *tissue* in demyelinating lesions, without capacity for delineating stiffness at the individual cell or axon level.

Figure 33 C shows that increasing AA diameter led to a decrease in WI. Furthermore, the myelin that *was* wrapped on the higher-diameter AAs on average had shorter lengths. We note that the data reported in literature for biological axons or axon mimicking fibers with diameters below 2μm demonstrates that within that range the larger-caliber axons are preferentially myelinated[29], whereas our data consider axon mimics with diameters larger than 3 μm, which can model swollen axons in the inflammatory demyelinating lesions (and are also relevant to the PNS axon diameters). We continue further refining of our platform to capture sub-2μm axon diameter variation, closer to the biological range of the CNS axon diameters. **Figure 33 D** shows that increasing the mean separation between axons (in other words, reducing the axon density), which can model decreased axon density in chronic lesions, also decreased the WI, although with minimal effect on sheath length. In summary, these data show that AA stiffness, diameter, and spacing can all influence myelin wrapping by oligodendrocytes

principally by affecting the *number* of AAs wrapped (captured by the WI), although axon stiffness and diameter can also influence the *lengths* of the myelin sheaths deposited on the AAs by maturing oligodendrocytes.

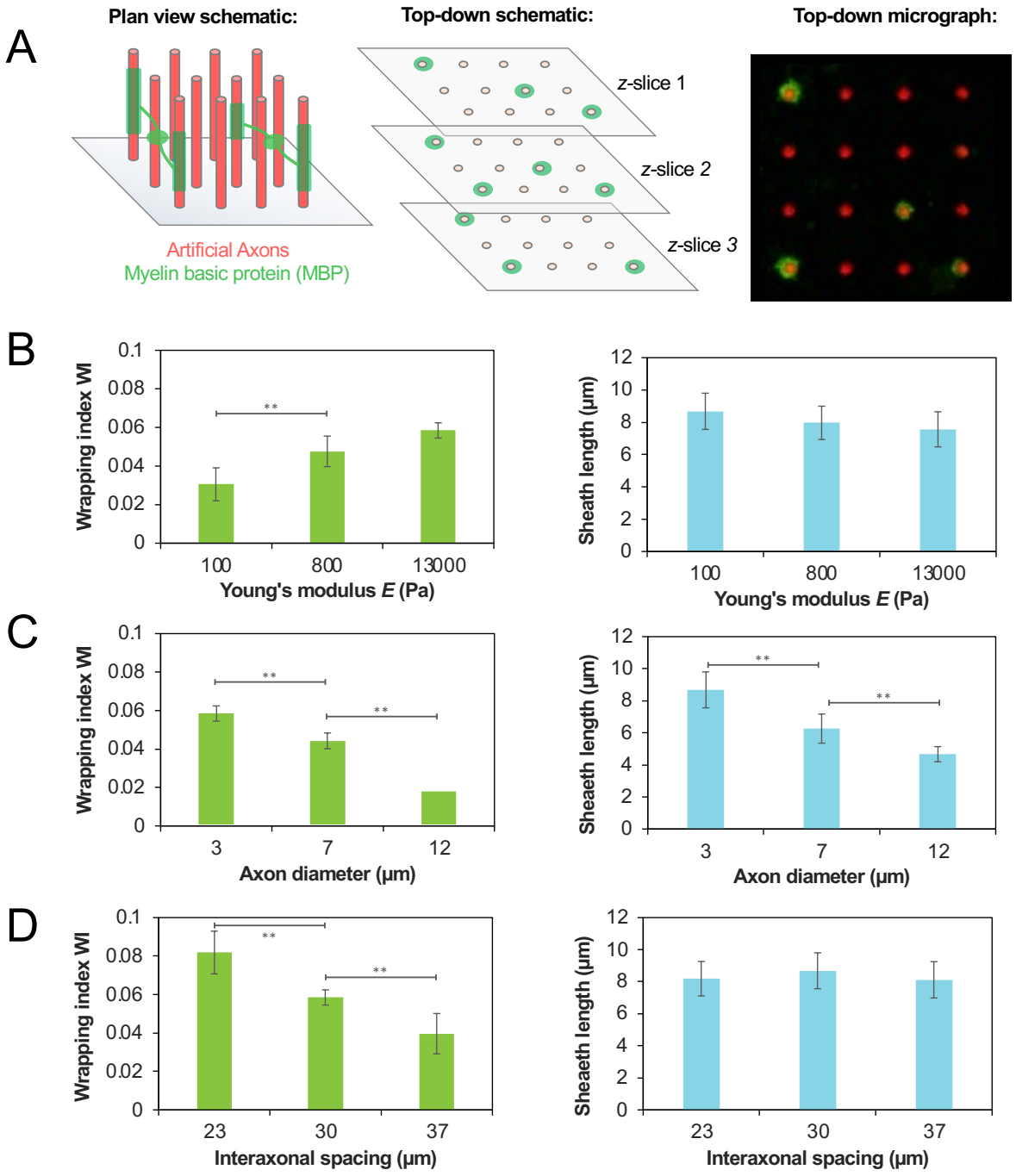

Figure 33 (A) Schematic of oligodendrocytes depositing myelin basic protein (MBP)-containing myelin on AAs. These are visualized through top-down confocal micrographs taken across multiple *z*-stacks. Scalebar in micrograph is 30 µm. Variation of oligodendrocyte myelin wrapping with (B) Young's modulus, (C) diameter, and (D) density. The left graph shows wrapping index WI, a measure of the *number* of AAs wrapped. The right graph shows the distribution of myelin sheath lengths on AAs. The data for panels C and D are for the E = 13000 Pa axons. Error bars represent standard error of the mean.

Based on the observed influence of axon stiffness on myelin wrapping (**Figure 33**), we hypothesized that the responses of oligodendrocytes to pro-myelinating compounds may also depend on axon stiffness. To test this hypothesis, we conducted myelin wrapping assays in the presence of several pro-myelinating compounds acting on various ligands and signaling pathways, on axons with two distinct stiffnesses, 13 kPa (material X) and 0.8 kPa (material Y), with the AAs of lower stiffness corresponding approximately to that of biological axons[30]. Rat oligodendrocytes where cultured for 7 days and dosed every other day with a compound at concentrations of 3 mM (ketoconazole, clemastine, benztropine, quetiapine, clobetasol, fasudil and miconazole) or 100 nM (tasin-1, tamoxifen, amorolfine, bazedoxifene, and T3). The chosen drug concentrations corresponded to the maximum efficacy (measured as wrapping index) in our previously conducted experiments on material X. At day 8, we fixed the cells and immunostained for MBP. We performed two independent experiments, each in triplicate.

Figure 34 shows that for many but not all tested compounds, the wrapping index (WI) differed in magnitude on axons with different stiffness. We observed higher WI on stiffer axons upon oligodendrocyte exposure to ketoconazole, T3, quetiapine, clemastine, and benztropine. By contrast, responses for bazedoxifene and amorolfine were weaker (i.e., lower WI) on stiffer axons compared to those corresponding to physiological stiffness of axons. We did not observe statistically significant differences as a function of AA stiffness in responses to tasin-1 and tamoxifen, or for clobetasol, fasudil and miconazole for which WI was low overall and did not exceed the levels for the DMSO negative control condition. Notably, oligodendrocyte responses to amorolfine included WI significantly exceeding the DMSO response for axons of physiological stiffness, but insignificant wrapping above the negative control on stiffer axons. Conversely, several compounds inducing significant wrapping activity on stiffer axons (clemastine, benztropine, miconazole) showed negligeable activity on more compliant axons.

A

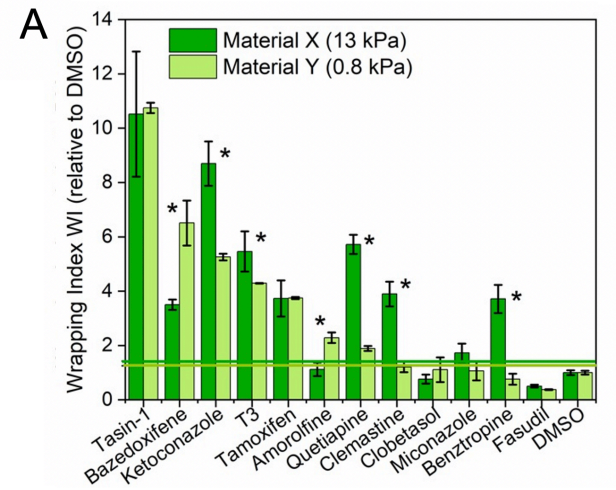

B

Compound	Rank - Material Y (0.8 kPa)	Rank - Material X (13 kPa)
Tasin-1	1	1
Bazedoxifene	2	3
Ketoconazole	3	1
T3	4	2
Tamoxifen	5	3
Amorolfine	6	Below control
Quetiapine	6	2
Clemastine	Below control	3
Clobetasol	Below control	Below control
Miconazole	Below control	4
Benztropine	Below control	3
Fasudil	Below control	Below control

Figure 34 (A) Effect of stiffness on promyelinating activity of compounds. (A) Wrapping index WI for compounds scaled by control (WI for DMSO) on stiffer (Young's modulus 13 kPa, dark green) and more compliant axons (Young's modulus 0.8 kPa, light green). Error bars are standard error of the mean. (*) statistically significant difference between responses on materials X and Y, $p < 0.05$. Horizontal lines denote 2 standard deviations above the respective DMSO controls. (B) Rank order of WI for compounds can differ on more compliant (0.8 kPa) and stiffer (13 kPa) axons. Materials X and Y are HDDA-starPEG hydrogels differing in extent of crosslinking resulting in different material stiffness.

Additionally, the relative ranking of WI among these compounds differed when assessed on stiffer compared to compliant axons (**Figure 34 B**). While the compound eliciting the highest WI under these dosages and conditions was the same for both AA stiffnesses (tasin-1), the compounds ranked second and lower varied and could only be distinguished statistically for the more compliant axons. This indicates that using this assay with highly stiff AAs could result in either over- or underestimating of compounds efficacy, and also potentially missing some promising compounds. This supports the concept that evaluation of pro-myelinating potential should include assays with mechanical stiffness representative of the target environment. We note that the above results reflect specific combinations of biophysical and biochemical environment (specific axon coating, axon stiffness range, concentrations of compounds, cell batch), and we do not claim generalizable results for all conditions or compounds. Rather, we consider this example a proof-of-concept of the importance of a more mechanically

matched environment for drug screening. The data from **Figure 34** represent an average of two biological replicates; the deindividuated data are shown in **Figure 35**.

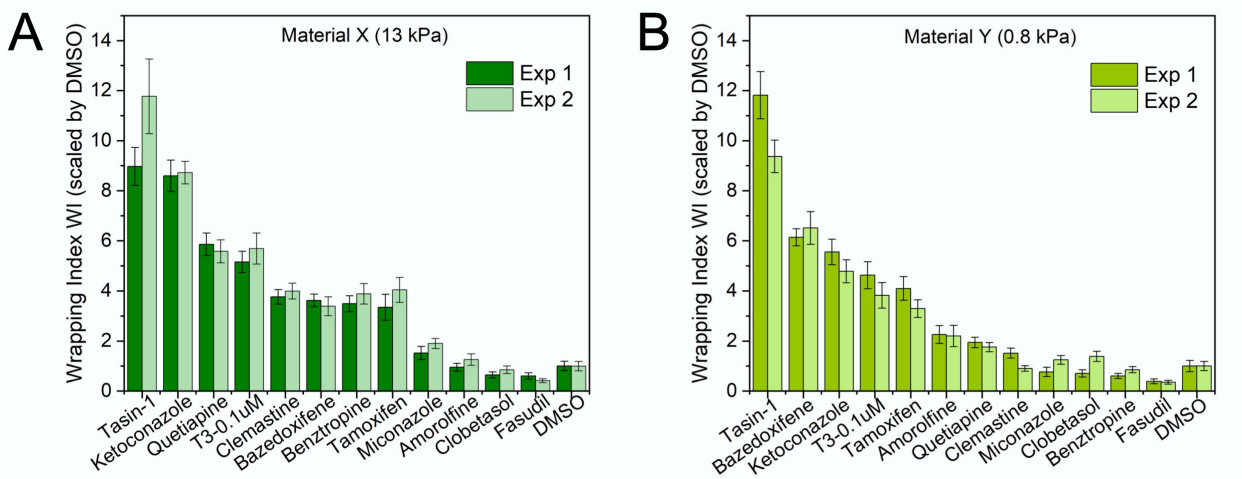

Figure 35 Deindividuated data for **Figure 34**, showing each of the two biological replicates

In summary, we demonstrated that the fabrication and implementation of 3D AAs can enable direct measurement of how biophysical cues influence the 3D process of myelin ensheathment by rat oligodendrocytes. By modulating the material composition and fabrication conditions, we developed AAs with tunable Young's moduli or mechanical stiffness (from the Pa to the kPa range), diameters (3 μm-15 μm) and axon densities. Increasing the Young's moduli or density of AAs corresponded in a concomitant increase in the mean *number* of AAs ensheathed by oligodendrocytes as quantified by a myelin WI that was normalized for the total cell number, with minimal impact on the resulting sheath segment lengths. Increasing the AA diameter corresponded to a decrease in the mean number of AAs ensheathed *and* a decrease in the mean segment lengths. Although future work is needed to even more closely represent physical cues of physiological axons (for instance, fabricating AAs with sub-3 μm diameter), these results demonstrate the capacity to probe correlative and causal relationships between biophysical cues and myelin wrapping *in vitro*.

An important application of *in vitro* modeling is the potential to compare and identify drug compounds that could stimulate myelin repair in demyelinating diseases. We found that the relative efficacies of pro-myelinating compounds differed depending on AA stiffness, as quantified by the wrapping index, which may have implications for *in vitro* drug screening. For example, the compounds identified from high-stiffness substrata such as tissue-culture polystyrene (TCPS) may not be representative of the 3D wrapping responses predicted in a more compliant biomechanical environment. As **Figure 34** suggests, it is possible that drugs which *may* have been ranked highly in mechanically compliant environments could be missed when screening oligodendrocyte response in formats of superphysiological stiffness. Collectively, these results speak to the importance of studying myelination in mechanically representative environments.

3.6 How myelin debris and microglia affect myelin wrapping

In addition to changes in tissue stiffness and axon density, other hallmarks of demyelinating lesions include inflammation, glial scar formation, and the presence of myelin debris[31]. Multiple sclerosis is characterized by an inflammatory cascade wherein immune cells, including autoreactive T cells, B cells, and macrophages are recruited to the brain[32–34]. This leads to the destruction of myelin through a range of immune-mediated mechanisms, such as cytokine damage, oxidative injury and phagocytosis. An ongoing research question is how features of the demyelinating lesion may inhibit the remyelination process, for example whether and how the lesion environment may inhibit the differentiation and recruitment of OPCs to repair the lost myelin. For example, the accumulation of myelin debris and inflammatory cytokines[35] is thought to contribute to a growth inhibitory environment that impairs remyelination[36,37].

Prior *in vitro* studies have shown that the presence of exogenous myelin debris can arrest the differentiation of OPCs[38]. This result was substantiated by more recent *in vivo* studies in which rat brain stem lesions were injected with purified myelin, which also inhibited remyelination by OPCs[39]. Interestingly, injecting purified fragments of liver membrane also led to a mild inhibitory effect on OPC differentiation, even though

purified liver membrane does not produce any inhibitory effect *in vitro*. One hypothesis is that debris clearance by microglia is essential during remyelination, and the presence of liver debris overwhelmed the phagocytic ability of microglia cells, therefore impeding the full clearance of myelin debris from the lesion. It is still unclear what molecular mechanisms cause exogenous myelin debris to inhibit remyelination.

These results speak to the critical role of microglia in debris clearance and repair. More broadly, microglia are the tissue-resident macrophages of the central nervous system, playing important roles in surveilling the brain parenchyma, being 'activated' by markers of cell injury, and playing a role in tissue repair and maintenance[40,41]. Many studies have pointed towards a link between inefficient debris clearance by microglia and impaired remyelination. In one cuprizone mouse model of demyelination, mice with a CX3CR1 knockout (a cell surface receptor in microglia that ordinarily plays important roles in debris uptake) had impaired remyelination[42]. In a similar study, mice with a TREM2 knockout (a phospholipid receptor expressed by microglia that can bind myelin debris) also resulted in impaired remyelination[36,37].

The role of microglia is more nuanced than simply engulfing debris alone. In fact, during demyelination, microglia can play both beneficial and harmful roles. For example, microglia can not only engulf debris but also secrete pro-repair soluble factors[43]. However, microglia can also adopt a pro-inflammatory phenotype that can exacerbate demyelination and contribute directly to the pathology[44]. Therefore, it is generally accepted that the field should stop arguing for microglia as being good or bad, but rather acknowledge their broad involvement in both injury and repair.

The impact of myelin debris on myelination represents a promising context in which to use AAs. Since this result has been validated using *in vivo* studies, if we can recapitulate the same negative effect of myelin debris *in vitro*, this would suggest that the AAs are indeed amenable to modeling disease-like environments and yielding similar results to *in vivo* studies. Therefore, we seeded rat OPCs on AAs, and on day 2 of the culture we added varying degrees of purified myelin debris (obtained from the Li-Huei Tsai Laboratory). After 14 days of culture, we fixed and stained the cells for MBP and

determined the wrapping index in each condition. **Figure 36** shows the dose-dependent effect of exogenous myelin debris, where increasing debris concentration resulted in a monotonic decrease in the extent of myelin wrapping. Since this experiment did not involve any microglia, these results also speak to the direct inhibitory effect of myelin debris on the oligodendrocytes (as opposed to exerting their inhibitory effect through microglia as an intermediate mechanism). In sum, this finding is consistent with previous *in vivo* results about the inhibitory effect of myelin debris, and shows the potential promise of using AAs as a reductionist *in vitro* model for lesion-like environments.

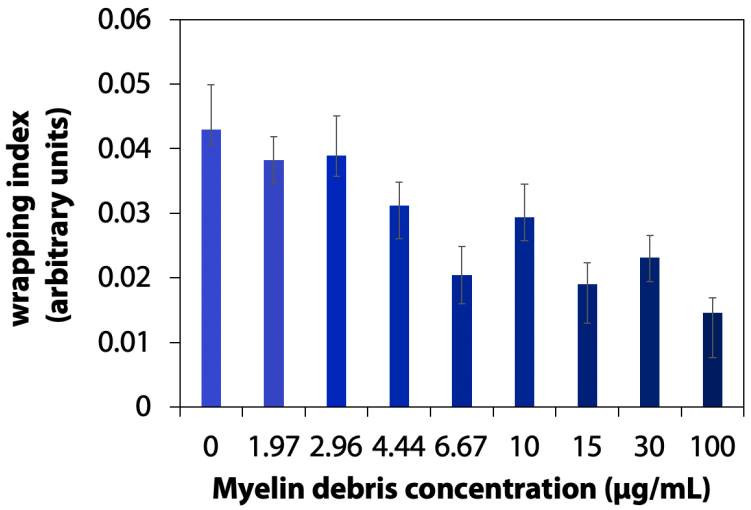

Figure 36 Dose-dependent effect of exogenous myelin debris on the wrapping index of primary rat oligodendrocytes. Error bars show standard error of the mean (SEM) across two biological replicates.

Next, we investigated the effect of microglia co-culture on OPC wrapping. We seeded primary rat OPCs onto AAs, at our standard seeding density of 20k OPCs per well of a 96-well plate. On day 2, we added differing numbers of hiPSC-derived microglial cells. After 14 days of culture, we fixed and stained the cells for MBP. We found that there was also a dose-dependent effect of microglia on OPCs, where there was an optimum seeding ratio of 20k OPCs: 10k microglia that led to the most beneficial effect on

wrapping (**Figure 37**). These results speak to the promise of using AAs to investigate how co-culture of oligodendrocytes with other cell types may influence myelin ensheathment. An important methodological caveat here is that due to cell availability, this experiment involved co-culturing primary rat oligodendrocytes with human iPSC-derived microglia. Future experiments can attempt to use either exclusively primary murine cells or human iPSC-derived cells to avoid any inadvertent complexity that may have been introduced by this species mixing.

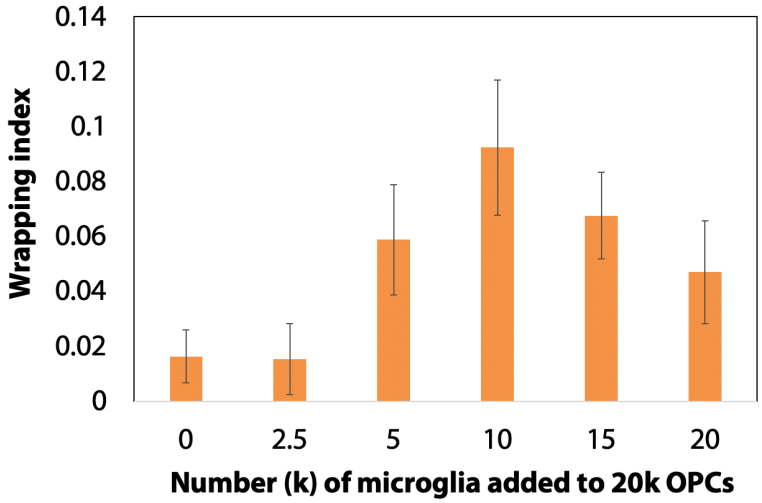

Figure 37 Dose-dependent effect of microglia co-culture on the wrapping index of primary rat oligodendrocytes. Error bars show standard error of the mean (SEM) across two biological replicates.

Finally, we explored whether in the absence of oligodendrocytes, microglia seeded on AAs could engulf myelin debris. We seeded 10k microglia onto each well of AAs, and on day 2 of culture we added 10 µg/mL of purified myelin debris. The debris was tagged with a pH-sensitive pHrodo dye, causing the debris to fluoresce in acidic environments. Therefore, if the myelin debris is successfully phagocytosed by microglia and trafficked to the acidic lysosome, those microglia should fluoresce. **Figure 38** is an example confocal micrograph showing the presence of fluorescing myelin debris on the

AAs, indicating that microglia can indeed successfully uptake exogenous myelin debris on the AA platform. Interestingly, in the upper left corner of the image, we also observe some microglia fully engulfing the AAs themselves.

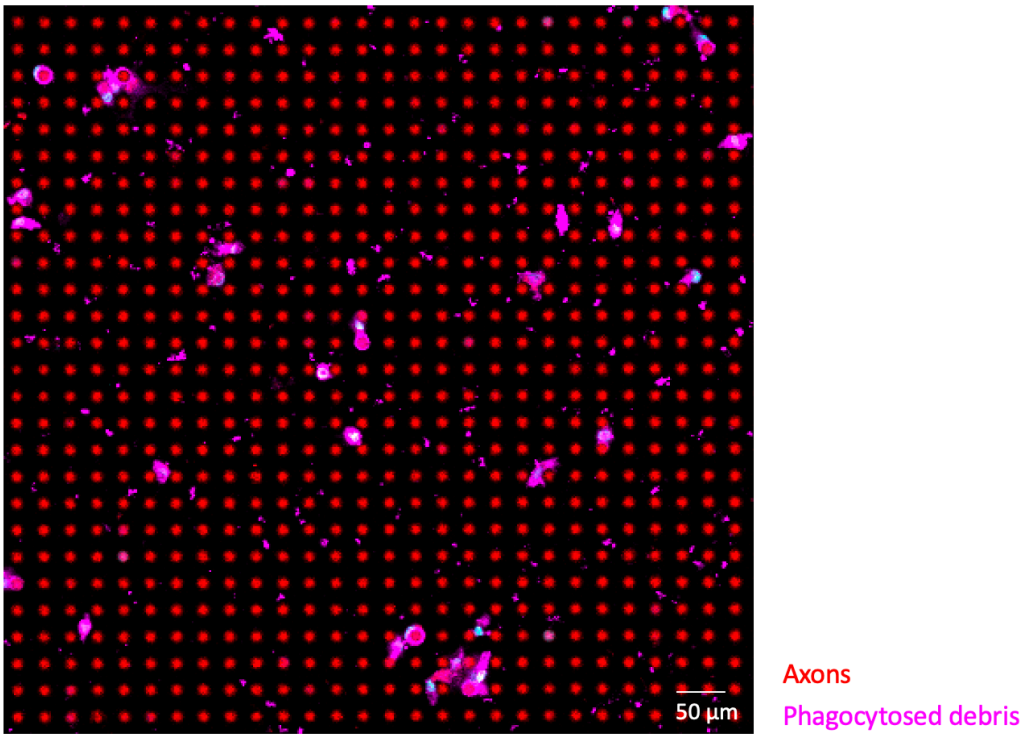

Figure 38 Confocal micrograph showing uptake of pHrodo-labeled myelin debris by microglia seeded on AAs

Together, the three results above pave the way towards investigating the tripartite interactions between myelin debris, microglia co-culture, and oligodendrocytes. For example, when all three components are added to AAs, do microglia uptake myelin debris and thus rescue myelin ensheathment compared to conditions where microglia are absent? Or do microglia adopt an inflammatory phenotype upon debris uptake and produce a detrimental effect on myelin ensheathment? Our initial results for this question are shown in **Figure 39**, however we caution against overinterpretation of these results. Although it may appear that microglia co-culture can beneficially affect myelin wrapping even in the presence of debris, unfortunately this result failed to

recapitulate the *negative* effect of debris. We hypothesize that this was because we switched to a new batch of myelin debris when starting this experiment, which may have had differences in its isolation protocol. Therefore, in future repeats of this experiment, we recommend using the same batch of myelin debris, first verifying that the debris has a negative impact on myelin ensheathment before incorporating microglia into the co-culture system.

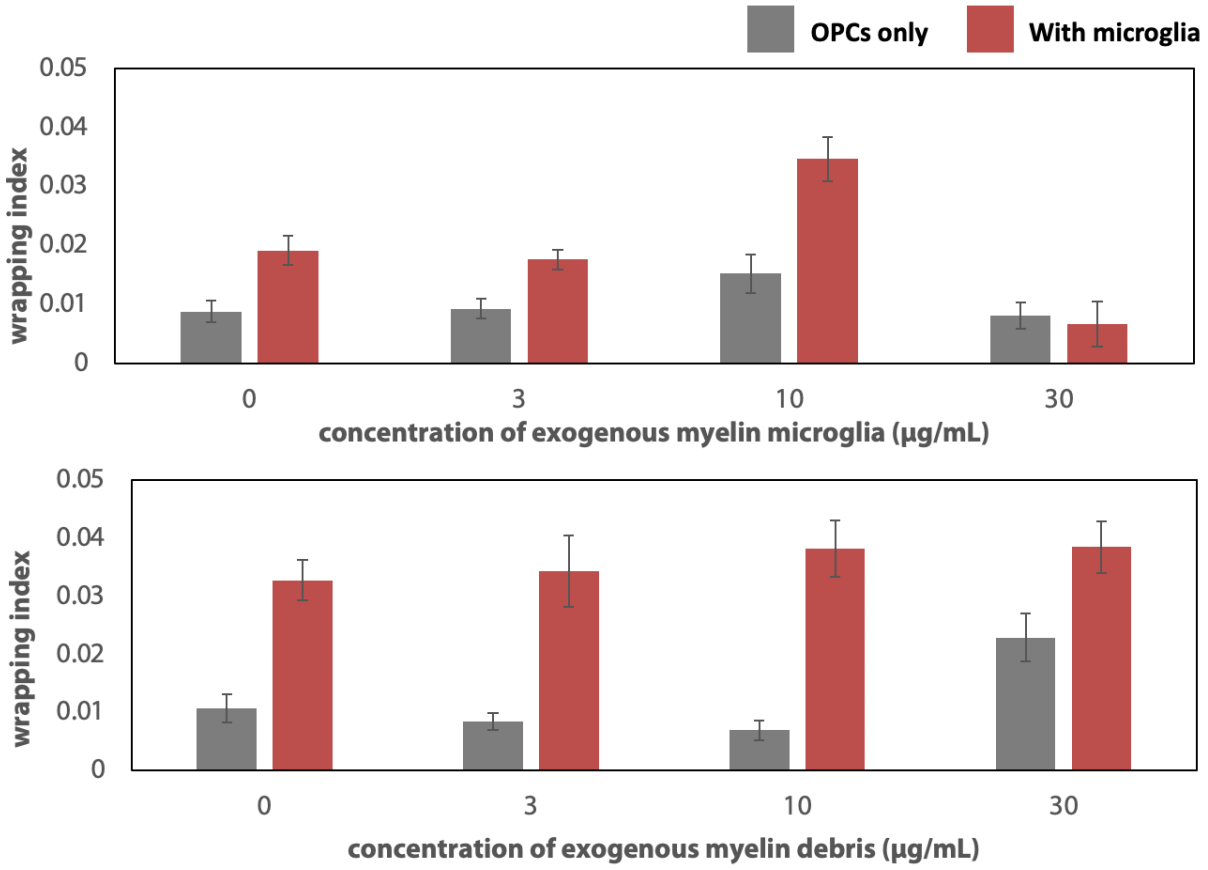

Figure 39 Preliminary results investigating the tripartite interaction between myelin debris, microglia co-culture and oligodendrocytes. Error bars show standard error of the mean (SEM).

3.7 Materials and Methods

Fabrication of Artificial Axons (AAs)

Artificial axons were fabricated directly in 96-well plates, using a projection microstereolithography setup. To vary axon stiffness (material Young's modulus) the resins were prepared with varying ratios of 1,6-hexanediol diacrylate (HDDA) (Sigma-Aldrich) and 4-arm PEG acrylate (starPEG) (JenKem) monomers, at mass ratios of 3:1, 2:1, and 1:1. The resins were pipetted into the wells of 96-well plates and exposed to UV light using our custom made projection microstereolithography setup[45]. Projecting the UV light onto the resin through the digital mask caused the liquid monomer resin to polymerize into solid vertical pillars that match the geometric pattern of the mask. The shape of the mask, the composition of the resin, the UV exposure duration, and the UV exposure intensity could all be modified to independently tune the Young's modulus, diameter, and spacing of the axons. For convenience, for the experiments on drug-induced myelination on different stiffness axons, we used a physical mask with the area corresponding to the area of the entire plate bottom, to generate axons in all plate wells simultaneously. Prior to introduction of rat oligodendrocyte progenitor cells, the AAs were functionalized with poly-D-ornithine (Sigma-Aldrich) (50 μg/mL) followed by incubation with laminin (Gibco) (20 μg/mL) to facilitate cell adhesion. The completed AA plates were stored in PBS at 4°C and warmed to 37°C the day of OPC seeding.

Mechanical characterization of AAs

The Young's modulus E of the cured AA material was determined using atomic force microscope (AFM)-enabled nanoindentation measurements (MFP-3D Bio, Asylum Research). Cylindrical structures of each material (10 μm thickness and width) were fabricated by projection microstereolithography using the same printing conditions as the AAs, and equilibrated overnight in PBS. AFM measurements were performed using a cantilever with nominal spring constant k = 0.1 N/m, terminating in a poly(methyl methacrylate) spherical probe with approximate diameter 1.5 μm (NanoAndMore). The

actual spring constant was calibrated via the thermal noise method[46]. Between 30 and 40 force-depth responses were collected from each sample of the material. The cantilever base velocity was 1 μm/s, and probe retraction was triggered after reaching a maximum force of 30-100 nN, with lower forces for the more compliant samples. Young's moduli *E* were calculated by fitting the spherical Hertzian elastic contact model for data acquired up to an indentation depth of 200 nm.

3D myelin wrapping assay

Rat oligodendrocyte progenitor cells (rOPCs) were isolated from neonatal rat brains (postnatal day 1) using magnetic sorting with beads coated with A2B5 antibodies (Miltenyi). The isolated cells were expanded in tissue culture flasks for 2-3 days in proliferation medium containing DMEM/F-12 media (Gibco), penicillin-streptomycin (Gibco), B-27 (Gibco), 10 ng/mL each of platelet-derived growth factor (PDGF) (Gibco), and fibroblast growth factor (FGF) (Gibco). Expanded rOPCs were seeded in 96-well AA plates at a density of 20,000 cells per well in differentiation medium, consisting of DMEM/F-12 media, B-27, and 2 ng/mL each of PDGF and FGF. Only the inner 60 wells were used to avoid the outermost perimeter of wells which had accelerated liquid evaporation. 24 hours after seeding, 1/3 of the media was changed with fresh differentiation medium supplemented with a pro-myelinating drug. As the control condition, we used medium containing 0.1% DMSO, which was the solvent vehicle used for other compounds. Media exchange of 33% volume occurred every other day, and cells grew on the AAs for either seven or 14 days before being fixed and stained. Every condition was repeated in at least triplicate, and two independent biological replicates (separate rounds of cell culture with two different rOPC batches) were conducted.

Immunostaining

Cells were fixed with 4% paraformaldehyde (Electron Microscopy Sciences), washed three times with PBS, and permeabilized with 0.1% v/v Triton X-100 and 5% v/v goat serum in PBS for 10 minutes at room temperature. Then, cells were washed three times

in PBS and blocked for 1 hour in 5% v/v goat serum in PBS for 1 hour at room temperature. Cells were incubated in primary antibody (rat anti-MBP, BioRad, 1:200 dilution) for 24 hours at 4°C. Next, cells were washed three times in PBS and incubated with secondary antibody (Alexa-Fluor-647 goat anti-rat, Thermo Fisher, 1:200 dilution) for 1 hour at room temperature. Cells were then washed three times in PBS and incubated with DAPI (Thermo Fisher, 1:1000 dilution) for 5 minutes. Finally, cells were washed once more and stored in PBS at 4°C.

Fluorescence imaging

Stained samples were imaged under three fluorescent channels (Alex-Fluor 647 for MBP+ myelin, rhodamine for AAs, DAPI for nuclei) using a confocal microscope (Olympus, FluoView 3000) at 20x air lens. For each well of the 96-well plate, eight fields of view were imaged; at each one, a confocal stack image was taken consisting of 8 *z*-stacks separated by a step size of 2 μm. Collectively, ~10,000 AAs were imaged and analyzed per well.

Quantification of 3D myelin wrapping on AAs

The fluorescent optical *z*-stack images were processed through an in-house image analysis pipeline. In brief, the AA, MBP+, and DAPI channels were imported to ImageJ and thresholded to obtain binary masks, followed by 3D volume reconstructions of the *z*-stacks. A 1-pixel-thick outline was traced around each AA; the outline was compared to the myelin mask to quantify the fraction of each axon circumference ensheathed by myelin. Aggregating across all *z*-stacks, AA pillars were classified as ‘fully wrapped’ if they exhibited a contiguous >6 μm ensheathed segment length in which the AA pillar was >80% wrapped in oligodendrocyte-synthesized myelin membrane positive for myelin basic protein (MBP) across all *z*-stacks of that pillar height. For each field of view, a myelin wrapping index (WI) was calculated, as the number of fully wrapped artificial axons normalized by the number of cell nuclei.

Statistical analysis

All imaged fields of view from a given experimental condition were pooled and averaged to determine a mean wrapping index per condition. For pairwise comparisons between conditions, Mann Whitney Wilcoxon tests were performed using the SciPy package in Python. For three-way comparisons between three tested conditions, Kruskal-Wallis tests were performed using the SciPy package. For drug response experiments, pairwise comparisons between conditions were done using one way ANOVA with Bonferroni correction within Origin Pro software.

3.8 References

1. Makhija, E. P., Espinosa-Hoyos, D., Jagielska, A. & Van Vliet, K. J. Mechanical regulation of oligodendrocyte biology. *Neurosci. Lett.* **717**, (2020).
2. Lourenço, T. *et al.* Modulation of oligodendrocyte differentiation and maturation by combined biochemical and mechanical cues. *Sci. Rep.* **6**, (2016).
3. Urbanski, M. M., Brendel, M. B. & Melendez-Vasquez, C. V. Acute and chronic demyelinated CNs lesions exhibit opposite elastic properties. doi:10.1038/s41598-018-37745-7.
4. Segel, M. *et al.* Niche stiffness underlies the ageing of central nervous system progenitor cells. *Nature* **573**, 130–134 (2019).
5. Espinosa-Hoyos, D. *et al.* Mechanosensitivity of Human Oligodendrocytes. *Front. Cell. Neurosci.* (2020) doi:10.3389/fncel.2020.00222.
6. Jagielska, A. *et al.* Mechanical environment modulates biological properties of oligodendrocyte progenitor cells. *Stem Cells Dev.* **21**, 2905–2914 (2012).
7. Jagielska, A. *et al.* Mechanical strain promotes oligodendrocyte differentiation by global changes of gene expression. *Front. Cell. Neurosci.* **11**, 1–16 (2017).
8. Rosenberg, S. S., Kelland, E. E., Tokar, E., De La Torre, A. R. & Chan, J. R. The geometric and spatial constraints of the microenvironment induce oligodendrocyte differentiation. *Proc. Natl. Acad. Sci. U. S. A.* **105**, 14662–14667 (2008).
9. Lee, S. *et al.* A culture system to study oligodendrocyte myelination processes using engineered nanofibers. **9**, (2012).
10. Urbanski, M. M. *et al.* Myelinating glia differentiation is regulated by extracellular matrix elasticity. *Sci. Rep.* **6**, (2016).
11. Leipzig, N. D. & Shoichet, M. S. The effect of substrate stiffness on adult neural stem cell behavior. *Biomaterials* **30**, 6867–6878 (2009).
12. Elosegui-Artola, A. *et al.* Mechanical regulation of a molecular clutch defines force transmission and transduction in response to matrix rigidity. *Nat. Cell Biol.* **18**, (2016).
13. Bangasser, B. L. *et al.* Shifting the optimal stiffness for cell migration. *Nat. Commun.* **8**, (2017).
14. Simons, M. & Trajkovic, K. Neuron-glia communication in the control of oligodencrocyte function and myelin biogenesis. *J. Cell Sci.* **119**, 4381–4389 (2006).

15. Katsumi, A., Orr, A. W., Tzima, E. & Schwartz, M. A. Integrins in Mechanotransduction. *J. Biol. Chem.* **279**, 12001–12004 (2004).

16. Sun, Z., Guo, S. S. & Fässler, R. Integrin-mediated mechanotransduction. **215**, (2016).

17. Hieda, M. cells Signal Transduction across the Nuclear Envelope: Role of the LINC Complex in Bidirectional Signaling. doi:10.3390/cells8020124.

18. Wuerfel, J. *et al.* MR-elastography reveals degradation of tissue integrity in multiple sclerosis. *Neuroimage* **49**, 2520–2525 (2010).

19. Streitberger, K.-J. *et al.* Brain Viscoelasticity Alteration in Chronic-Progressive Multiple Sclerosis. doi:10.1371/journal.pone.0029888.

20. Schregel, K. *et al.* Demyelination reduces brain parenchymal stiffness quantified in vivo by magnetic resonance elastography. doi:10.1073/pnas.1200151109.

21. Riek, K. *et al.* Magnetic resonance elastography reveals altered brain viscoelasticity in experimental autoimmune encephalomyelitis ☆. *YNICL* **1**, 81–90 (2012).

22. Mikelberg, F. S., Drance, S. M., Schulzer, M., Yidegiligne, H. M. & Weis, M. M. The Normal Human Optic Nerve: Axon Count and Axon Diameter Distribution. *Ophthalmology* **96**, 1325–1328 (1989).

23. Liewald, D., Miller, R., Logothetis, N., Wagner, H. J. & Schüz, A. Distribution of axon diameters in cortical white matter: an electron-microscopic study on three human brains and a macaque. *Biol. Cybern.* **108**, 541–557 (2014).

24. Fisher, E. *et al.* Imaging correlates of axonal swelling in chronic multiple sclerosis brains. *Ann. Neurol.* **62**, 219–228 (2007).

25. Sasaki, S., Maruyama, S., Yamane, K., Sakuma, H. & Takeishi, M. Swellings of proximal axons in a case of motor neuron disease. *Ann. Neurol.* **25**, 520–522 (1989).

26. Bjartmar, C., Wujek, J. R. & Trapp, B. D. Axonal loss in the pathology of MS: Consequences for understanding the progressive phase of the disease. *J. Neurol. Sci.* **206**, 165–171 (2003).

27. Roduit, C. *et al.* Stiffness tomography by atomic force microscopy. *Biophys. J.* **97**, 674–677 (2009).

28. Thomas, G., Burnham, N. A., Camesano, T. A. nn. & Wen, Q. Measuring the mechanical properties of living cells using atomic force microscopy. *J. Vis. Exp.* 1–8 (2013) doi:10.3791/50497.

29. Lee, S. *et al.* A culture system to study oligodendrocyte myelination processes using engineered nanofibers. *Nat. Methods* **9**, 917–922 (2012).

30. Moeendarbary, E. *et al.* The soft mechanical signature of glial scars in the central nervous system. *Nat. Commun.* **8**, (2017).

31. Longo, D. L., Reich, D. S., Lucchinetti, C. F. & Calabresi, P. A. Multiple Sclerosis. *N Engl J Med* **378**, 169–80 (2018).

32. Frohman, E. M., Racke, M. K. & Raine, C. S. *Medical Progress Multiple Sclerosis-The Plaque and Its Pathogenesis*. www.nejm.org (2006).

33. Lassmann, H., Brück, W. & Lucchinetti, C. Heterogeneity of multiple sclerosis pathogenesis: Implications for diagnosis and therapy. *Trends in Molecular Medicine* vol. 7 115–121 (2001).

34. Ghasemi, N., Razavi, S. & Nikzad, E. *Multiple Sclerosis: Pathogenesis, Symptoms, Diagnoses and Cell-Based Therapy Citation: Ghasemi N, Razavi Sh, Nikzad E. Multiple sclerosis: pathogenesis, symptoms, diagnoses and cell-based therapy*. *CELL JOURNAL(Yakhteh)* vol. 19.

35. Starost, L. *et al.* Extrinsic immune cell-derived, but not intrinsic oligodendroglial factors contribute to oligodendroglial differentiation block in multiple sclerosis. *Acta Neuropathol.* (2020) doi:10.1007/s00401-020-02217-8.

36. Neumann, H., Kotter, M. R. & Franklin, R. J. M. Debris clearance by microglia: An essential link between degeneration and regeneration. *Brain* vol. 132 288–295 (2009).

37. Cignarella, F. *et al.* TREM2 activation on microglia promotes myelin debris clearance and remyelination in a model of multiple sclerosis. *Acta Neuropathol.* **140**, 513–534 (2020).

38. Robinson, S. & Miller, R. H. Contact with central nervous system myelin inhibits oligodendrocyte progenitor maturation. *Dev. Biol.* **216**, 359–368 (1999).

39. Kotter, M. R., Li, W.-W., Zhao, C. & Franklin, R. J. M. Brief Communication Myelin Impairs CNS Remyelination by Inhibiting Oligodendrocyte Precursor Cell Differentiation. (2006) doi:10.1523/JNEUROSCI.2615-05.2006.

40. Helmut, K., Hanisch, U. K., Noda, M. & Verkhratsky, A. Physiology of microglia. *Physiol. Rev.* **91**, 461–553 (2011).

41. Augusto-Oliveira, M. *et al.* What do microglia really do in healthy adult brain? *Cells* **8**, 1–17 (2019).

42. Lampron, A. *et al.* Inefficient clearance of myelin debris by microglia impairs

remyelinating processes. *J. Exp. Med.* **212**, 481–495 (2015).

43. Sariol, A. *et al.* Microglia depletion exacerbates demyelination and impairs remyelination in a neurotropic coronavirus infection. *Proc. Natl. Acad. Sci. U. S. A.* **117**, 24464–24474 (2020).

44. Guerrero, B. L. & Sicotte, N. L. Microglia in Multiple Sclerosis: Friend or Foe? *Front. Immunol.* **11**, 1–8 (2020).

45. Espinosa-Hoyos, D., Du, H., Fang, N. X. & Van Vliet, K. J. Poly(HDDA)-Based Polymers for Microfabrication and Mechanobiology. *MRS Adv.* **2**, 1315–1321 (2017).

46. Hutter, J. L. & Bechhoefer, J. Calibration of atomic-force microscope tips. *Rev. Sci. Instrum.* **64**, 1868–1873 (1993).

4. Modeling myelin ensheathment with human oligodendrocytes

4.1 Human induced pluripotent stem cells (hiPSCs)

All the experiments described thus far in this thesis used primary rat oligodendrocyte progenitor cells (OPCs) as the myelinating cells. Advancing the AA platform further necessitates the use of human oligodendrocytes. Since it is practically impossible to non-invasively obtain live OPCs from a human brain, one promising approach is to derive oligodendrocytes from human induced pluripotent stem cells (hiPSCs).

Stem cells are unspecialized cells that are capable of self-renewal and can differentiate into multiple other cell types that are more specialized in function. Stem cells give rise to all somatic cell types of the human body, and are increasingly being leveraged for regenerative medicine and tissue engineering applications[1–3]. One way to classify stem cells is by their potency, which is the range of specialized cell types into which a stem cell can differentiate[4]. Totipotent stem cells, such as the zygote, have the potential to differentiate into any specialized cell type. Pluripotent stem cells, such as the embryonic stem cells (ESCs) formed during early development, can differentiate into almost all cell types with the exception of extraembryonic cells, such as placental cells. Multipotent stem cells, such as hematopoietic stem cells and mesenchymal stem cells[2,5,6], are further committed and can only differentiate into specific cell lineages. Finally, unipotent stem cells, such as dermatocytes, are defined by their ability to continually replenish and renew one specific cell type. Therefore, leveraging stem cell pluripotency presents a promising avenue to derive human oligodendroglial cells for *in vitro* modeling.

During human development, the only naturally existing pluripotent stem cells are embryonic stem cells. However, seminal work by Takahashi, Yamanaka et al. demonstrated that it is possible to induce a pluripotent state in terminally differentiated

cells[7]. Using retroviral transduction of four transcription factors (Oct3/4, Sox2, Klf4, and c-Myc), they demonstrated that human adult dermal fibroblasts could be reprogrammed into a pluripotent state. The resultant cells, termed human induced pluripotent stem cells (hiPSCs), exhibited markers that were characteristic of human embryonic stem cells produced naturally during development. This study opened the possibility of deriving iPSCs from individual patients, thus paving the way towards personalized models of disease.

4.2 Protocol adaptation for differentiating hiPSCs

Many groups have developed protocols for differentiating OPCs from hiPSCs. One limitation of these approaches is that culture times are lengthy, reaching upwards of 200 days. Furthermore, the efficiency of producing O4+ cells is variable[8].

More recently, Douvaras and Fossati developed a differentiation protocol that produces O4+ OPCs from a 75-day culture[8], which was shorter than all previously reported approaches. They validated the protocol across nine iPSC lines derived from different donors, finding that the efficiency of O4+ OPC production ranged from 28-80%. This protocol involves providing soluble factors to iPSCs that mimic the endogenous signaling cues experienced by ESCs during development that drive oligodendroglia formation, outlined in **Figure 40**. We henceforth refer to the products of this differentiation as ‘human oligodendroglia’ because a known but unquantified fraction of resultant cells are not oligodendrocytes; astrocytes also make up a variable fraction of the products and are also able to proliferate under the same culture conditions. This represents a significant limitation to the iPSC differentiation protocol, since there can be significant batch-to-batch heterogeneity in the composition of the oligodendroglial cells obtained.

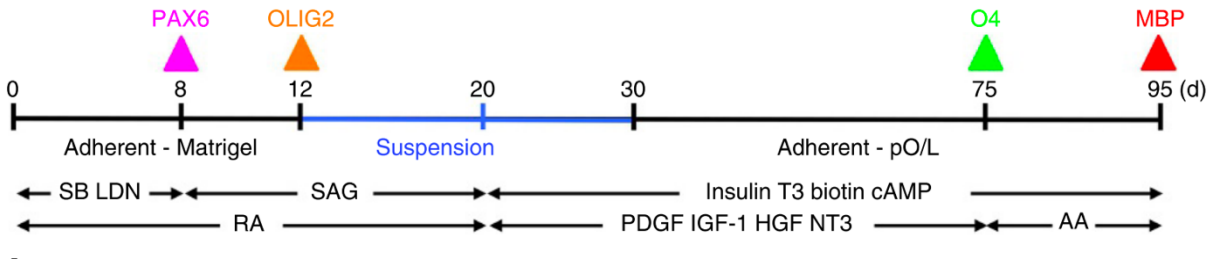

Figure 40 Differentiation protocol for generating human oligodendrocytes (hOLs) from human induced pluripotent stem cells (hiPSCs), from Douvaras and Fossati[8]

In brief, the hiPSC differentiation process is as follows: during days 0-8 of the differentiation protocol, iPSCs are exposed to SB431542 and LDN193189, factors that are shown to upregulate the differentiation of PAX6+ cells, a key marker of neural stem cells (NSCs) that are committed to this lineage. After an adherent culture of PAX6+ NSCs are grown to confluency, they are either mechanically or chemically dissociated and plated into a low-attachment plate, where the cells self-assemble to form spherical aggregates. This aggregation process is used to enrich for OLIG2+ cells, since OLIG2- cells do not self-assemble into aggregates. After 2-3 weeks of leaving the aggregates to grow in suspension, the aggregates are then replated for adherent culture on a tissue culture polystyrene (TCPS) plate, coated with laminin to mimic the extracellular matrix (ECM) cues found in the brain. At this point, cells are exposed to factors that drive differentiation from OLIG2+ OPCs to OLIG4+ pre-oligodendrocytes, such as platelet-derived growth factor (PDGF), neurotrophin 3 (NT3), and triiodo-L-thyronine (T3). Over 40 days of adherent culture, terminally differentiated neuroglial cells migrate out of the spheroids; this process starts with neurons and astrocytes migrating out, but at the day 75, O4+ pre-oligodendrocytes are the predominant cell type to emerge from the spheroid. Finally, all cells are enzymatically detached from the TCPS substrate to produce a suspension of oligodendroglial cells that can be seeded onto AAs.

Prior unpublished by myself and Daniela Espinosa-Hoyos in the Van Vliet Group used Douvaras and Fossati's protocol to generate hiPSC-derived OLIG4+ pre-oligodendrocytes for testing with Artificial Axons (AAs), but the results of the

differentiation were variable. Using four iPSC lines from separate donors, we observed significant inter-donor variation in the efficiency of OLIG4+ cell production. Furthermore, when the pre-oligodendrocytes were seeded on AAs, they would often fail (>50% of the time) to differentiate into MBP+ oligodendrocytes that ensheathed myelin around the AAs. These results varied significantly between donor lines, and also between multiple successive differentiation attempts of the same line of hiPSCs. These findings speak to the broader issue of cell heterogeneity, which is a common challenge underlying all iPSC technologies. For example, variability in cell behavior can be introduced by the age and biological sex of the donor, stochastic genetic or epigenetic changes that may be introduced during the reprogramming process, and batch effects across different differentiation conditions. For example, during the 75-day differentiation protocol, iPSCs are exposed to upwards of 20 different soluble factors, each of which may have subtle batch-to-batch variability, both in how each factor was originally isolated and manufactured, and also how those factors were handled in the lab (e.g., thawing time, storage time since receipt). Each of these factors could contribute sources of variability in the final cell phenotype; even if the individual effect size of an individual variable may be small, their unknown additive effect can contribute to large heterogeneity. Furthermore, this protocol does not result in a pure sample of pre-oligodendrocytes; instead, the composition of the final cell population is a mixed pool of astrocytes, neurons, and pre-oligodendrocytes, and the proportions of each can vary from batch to batch and from donor to donor. Since MBP+ myelin wrapping of these hiPSC-derived pre-oligodendrocytes was low (and non-existent the majority of the time), further optimization of the differentiation and cell seeding protocol was required to generate reproducible, quantifiable myelin wrapping of AAs.

First, we sought to improve the efficiency of MBP+ myelin ensheathment around AAs by hiPSC-derived oligodendroglia. One potential approach was to increase the cell seeding density, as prior work on rat OPCs showed that exceeding a critical cell density threshold promoted OPC differentiation[9]. In our previous experiments with rat OPCs, the typical plating density was 20k (20,000) OPCs per well of a 96-well plate. However, prior

work plating hiPSC-derived oligodendroglia at this same density led to inconsistent results, often with little to no MBP+ expression. One possible explanation is that the heterogeneity of hiPSC-derived cultures leads to lower proportions of actual OPCs within cell suspension, whereas the purity of OPCs is typically higher in primary rat OPCs. To that end, we plated hiPSC-derived oligodendroglia on AAs at four different seeding densities for 21 days: 40k, 60k, 80k, and 100k per well. Across three separate cell lines, and across two independent differentiations of each line, we observed a robust biphasic response: at the 40k and 60k plating densities, little to no MBP+ myelin was observed. At the 80k and 100k plating densities, consistent MBP production was observed (**Figure 41**).

These results are consistent with prior data of having a critical density threshold when differentiating OPCs *in vitro* – interestingly, these prior studies suggest that physical crowding is the primary mechanism that drives differentiation rather than active intercellular signaling. For example, prior work showed that adding inert polystyrene beads to a primary rat OPC culture to increase extracellular crowding (while holding OPC cell density constant) also drove OPC differentiation[9]. Based on these results, for all subsequent experiments in this thesis involving hiPSC-derived oligodendroglial cells, we use a standard cell seeding density of 80k per well.

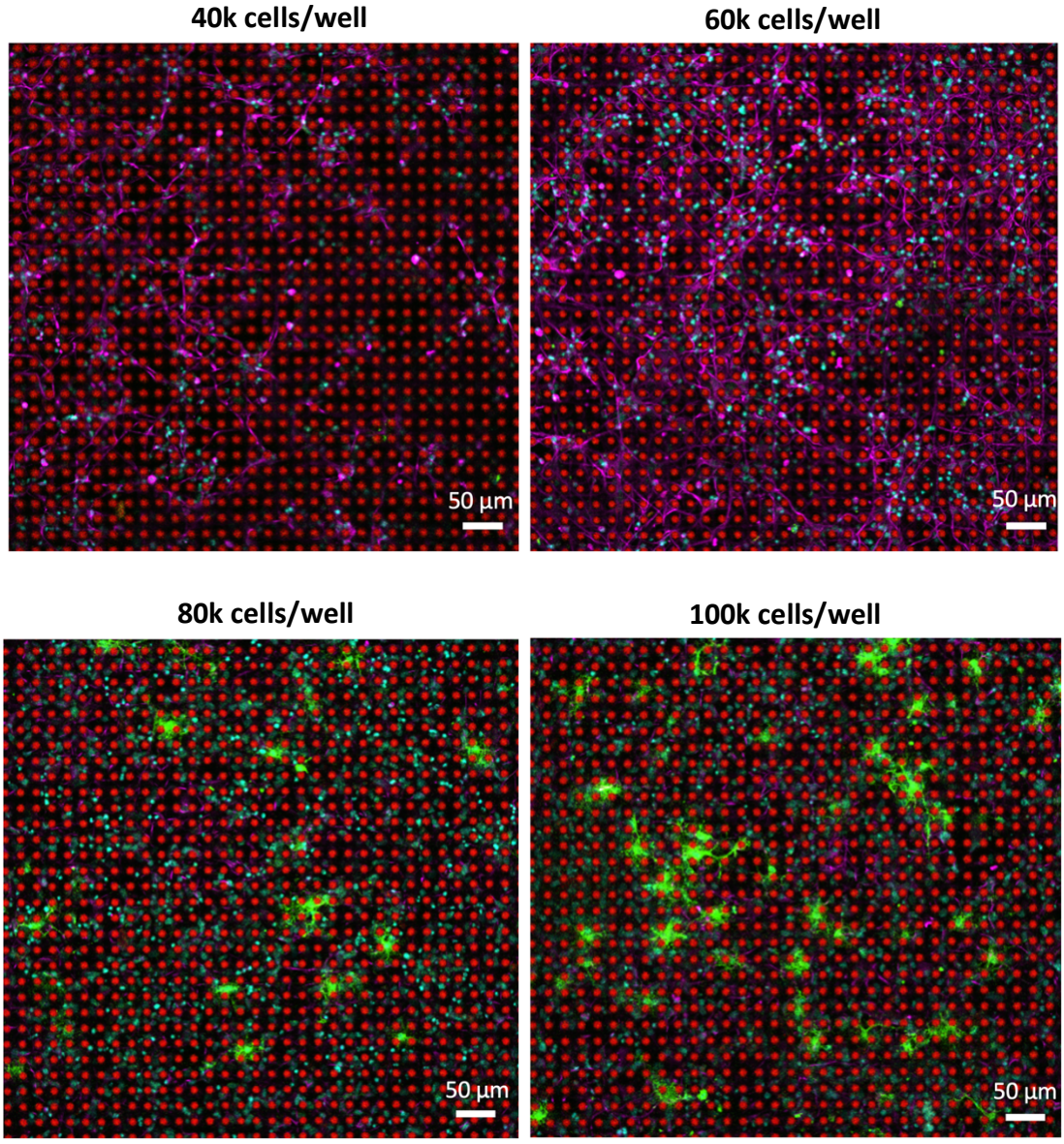

Figure 41 Confocal micrographs illustrating the dependence of hOL seeding density on production of MBP+ oligodendrocytes. Above 80k cells/well of a 96-well plate, reproducible myelin ensheathment is observed.

Next, we tested whether the hiPSC-derived oligodendroglial cells were amenable to freeze-thawing. A major advantage to using primary rat OPCs is that a large batch can be isolated at once, then all those OPCs can be frozen and then subsequently thawed when desired. In contrast, all our previous experiments with hiPSC-derived cells involved differentiating a fresh batch each time, leading to experiments that lasted 100+

days. An ideal workflow would be to differentiate a large batch of hiPSCs and freeze them at day 75 (after enzymatic attachment of the adherent spheroids to isolate a suspension of oligodendroglial cells). Then, this would result in a pool of ready-to-use human cells that can be thawed and immediately seeded on AAs.

In our first attempt to test freeze-thawing, we collected an oligodendroglial cell suspension at day 75 of the hiPSC differentiation protocol, which we separated into two batches. One batch was seeded immediately on AAs at a density of 80k cells/well for 21 days. The second batch was mixed with a commercial cryopreservative and stored in liquid nitrogen. After one week in liquid N_2, this second batch was thawed and then seeded on AAs at a density of 80k cells/well for 21 days. Both batches were fixed and stained at the end of the culture period. **Figure 42** shows that although both conditions had comparable cell densities, only batch 1 (plated on AAs immediately on day 75) exhibited MBP+ myelin, whereas batch 2 showed no myelin ensheathment.

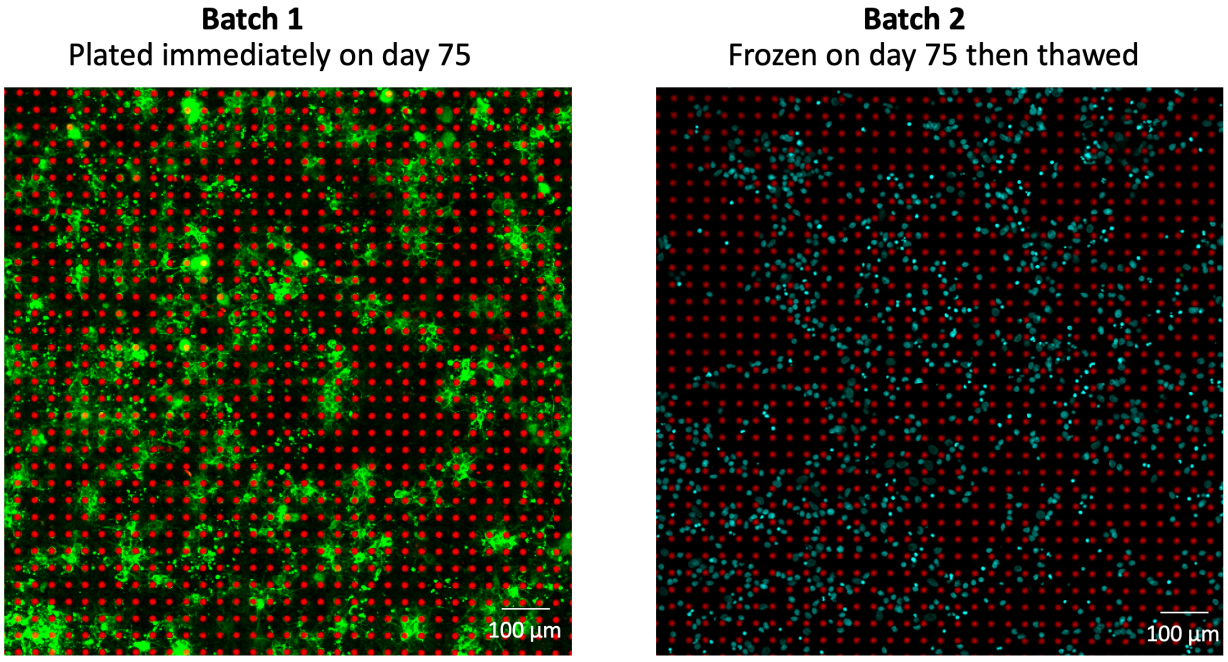

Figure 42 Confocal micrographs of hiPSC-derived hOLs, seeded directly on AAs on day 75 of the differentiation (batch 1) or seeded after freeze-thawing of cells on day 75 (batch 2)

Next, we attempted to promote OPC differentiation in batch 2 (freeze-thaw condition). We repeated the same experiment as described above, but this time added three additional conditions. First, plated the cells for 42 days instead of 21, to verify whether the freeze-thaw group *would have* eventually produced MBP+ myelin if given longer to differentiate. However, this was unsuccessful, and no MBP+ oligodendrocytes were observed, suggesting that the lack of MBP is not because the freeze-thawed oligodendrocytes were simpler slower to differentiate. As a positive control, we also seeded batch 1 (fresh) cells for 42 days and verified that they still exhibit MBP+ expression after a longer culture time. Secondly, instead of using the differentiation medium in Douvaras and Fossati's protocol, we attempted to grow the seeded oligodendroglial cells using conditioned media from hiPSC-derived neuron cultures, obtained from Li-Huei Tsai's laboratory. Our hypothesis was that conditioned media may contain additional soluble factors that might lead to paracrine signaling effects that promoted OPC differentiation. Similarly, freeze-thawed oligodendroglial cells did not differentiate into MBP+ cells, whereas our positive control of fresh cells did. Finally, we returned to using Douvaras and Fossati's differentiation medium, but instead of preparing a large batch of media to use over 30 days (as specified in the protocol), we remade the media with fresh reagents every day we fed the cells. Once again, this 'fresher' medium failed to elicit MBP+ oligodendrocytes in the freeze-thawed cells, but the positive control fresh cells continued to differentiate as per normal. These results indicate that within the parameter space we tested, hiPSC-derived oligodendroglial cells are not compatible to freeze-thawing, and should be used fresh during each differentiation for the best results.

Finally, we explored whether hiPSC-derived oligodendroglia were amenable to cell passaging to increase cell number. This is important because the requirement of higher cell plating densities demands an increase in the number of cells generated per differentiation. On day 75 of the differentiation protocol, after obtaining an oligodendroglial cell suspension, we plated all the cells on TCPS functionalized with laminin and regrew the cells to confluency, leading to a 5-fold increase in cell number.

After reaching confluency, we enzymatically detached the cells and split them into two batches as before. We plated one batch directly onto the AAs, and freeze-thawed the second batch before plating onto AAs for 21 days. As expected, the freeze-thawed group did not differentiate into MBP+ myelin. Interestingly, neither did the fresh cells, which also exhibited no MBP production. All the results described above are summarized in **Figure 43**. In summary, based on the conditions we tested, we conclude that hiPSC-derived oligodendroglia should be differentiated anew for each intended use case and plated directly onto AAs without any intermediate passaging or freeze-thawing steps. Although it was discouraging that these approaches were unsuccessful, we believe that this work has value in elucidating the parameter space of what can and cannot be done to increase the differentiation throughput of hiPSCs.

Description of condition	MBP+ cells observed?	
	Batch 1 (Fresh)	Batch 2 (Freeze-thaw)
Regular medium and protocol	YES	NO
Plate the cells for 42 days instead of 21.	YES	NO
Use 'conditioned media' from neuron cultures.	YES	NO
Add reagents to the differentiation medium fresh each day.	YES	NO
Passage cells at day 75	NO	NO

Figure 43 Summary of protocol modification steps to increase throughput of hOL production from hiPSCs

4.3 Drug response of hiPSC-derived OPCs vs. primary rat OPCs

AAs represent a promising platform for drug screening to discover therapeutics that may boost OPC differentiation and myelination. All commercial drug screens for pro-myelination compounds are conducted on TCPS substrates using primary rat OPCs, using a 2D MBP readout. The possibility of seeding hiPSC-derived oligodendroglial cells

on AAs raises the possibility of using human cells to discover drugs and also generate patient-specific dose-response curves, paving the way to more personalized medicine approaches. As a preliminary proof of concept, our goal was to explore whether the AA platform could be used to investigate the response of hiPSC-derived oligodendrocytes to pro-myelinating drugs, and also how the drug response of hiPSC-derived cells differed from primary rat OPCs.

First, we systematically characterized the response of primary rat OPCs to a range of promyelinating compounds. We tested a small library of compounds with demonstrated potency to increase expression of MBP by rat OPCs, to assess whether the platform could resolve dose-dependent propensity for 3D wrapping of AAs. The EC_{50} values of these compounds were established to be within the nanomolar to micromolar range when MBP expression was quantified by ELISA. We considered two subsets of compounds: group A comprising compounds with measured MBP-ELISA EC_{50} values within the range from 100 nM to 1 mM, and group B comprising compounds with measured MBP-ELISA EC_{50} within the range below 100 nM (**Figure 44**).

Compound	EC_{50}, nM			Efficacy (relative to T3)	
	3D AAs	2D Glass	ELISA* (MBP expression)	3D AAs	2D Glass
Group A					
benztropine	581	375	127	6.1 (0.6)	2.1 (0.1)
clemastine	678	121	120	4.3 (0.4)	1.4 (0.1)
clobetasol	1040	546	455	2.4 (0.5)	1.6 (0.2)
fasudil	-	339	260	2.5 (0.3)	1.0 (0.1)
ketoconazole	507	315	470	3.0 (0.5)	1.6 (1.1)
miconazole	623	397	302	1.9 (0.6)	1.5 (0.1)
quetiapine	635	207	184	2.3 (0.4)	1.9 (0.2)
Group B					
amorolfine	5	10	16	4.1 (0.4)	2.4 (0.2)
bazedoxifene	3	0.1	16	1.8 (0.2)	0.6 (0.1)
tamoxifen	8	2	88	6.4 (0.8)	2.0 (0.2)
tasin-1	22	13	17	7.8 (0.5)	2.0 (0.2)
T3	16	7	96	1.0 (0.2)	1.0 (0.1)

* ELISA experiments were performed with a different batch of rat OPCs than the 3D AA and 2D differentiation experiments.

Figure 44 EC_{50} (nM) and efficacy values (relative to T3) for compounds obtained for 3D myelin wrapping assay using AAs, 2D differentiation assay, and ELISA. Standard error of the mean (SEM) is in parentheses following the efficacy value.

For each compound, we computed the wrapping index (see Chapter 3 for definition), to generate a 9-point dose-response curve (**Figure 45**), which was fitted with a sigmoidal curve, allowing for calculation of the EC_{50} and efficacy (the maximum effect) of the compounds' promyelinating potential *in vitro* ((**Figure 45 B-D**). Our AA assay demonstrated well-defined dose-dependent myelin wrapping for almost all tested compounds. Only one compound (Fasudil) did not exhibit a response plateau/maximum at the highest tested concentration of 10 mM. To our knowledge this is the first *in vitro* platform that enables measuring the dose-dependence curves for myelin wrapping by rat OPCs. In the present 3D myelin wrapping assay, all tested compounds demonstrated higher efficacy than the vehicle DMSO and T3, the extensively validated promyelinating thyroid hormone (**Figure 44**). The highest promyelinating efficacy we measured for tasin-1, tamoxifen, and benztropine. The EC_{50} values quantified by our assay'.

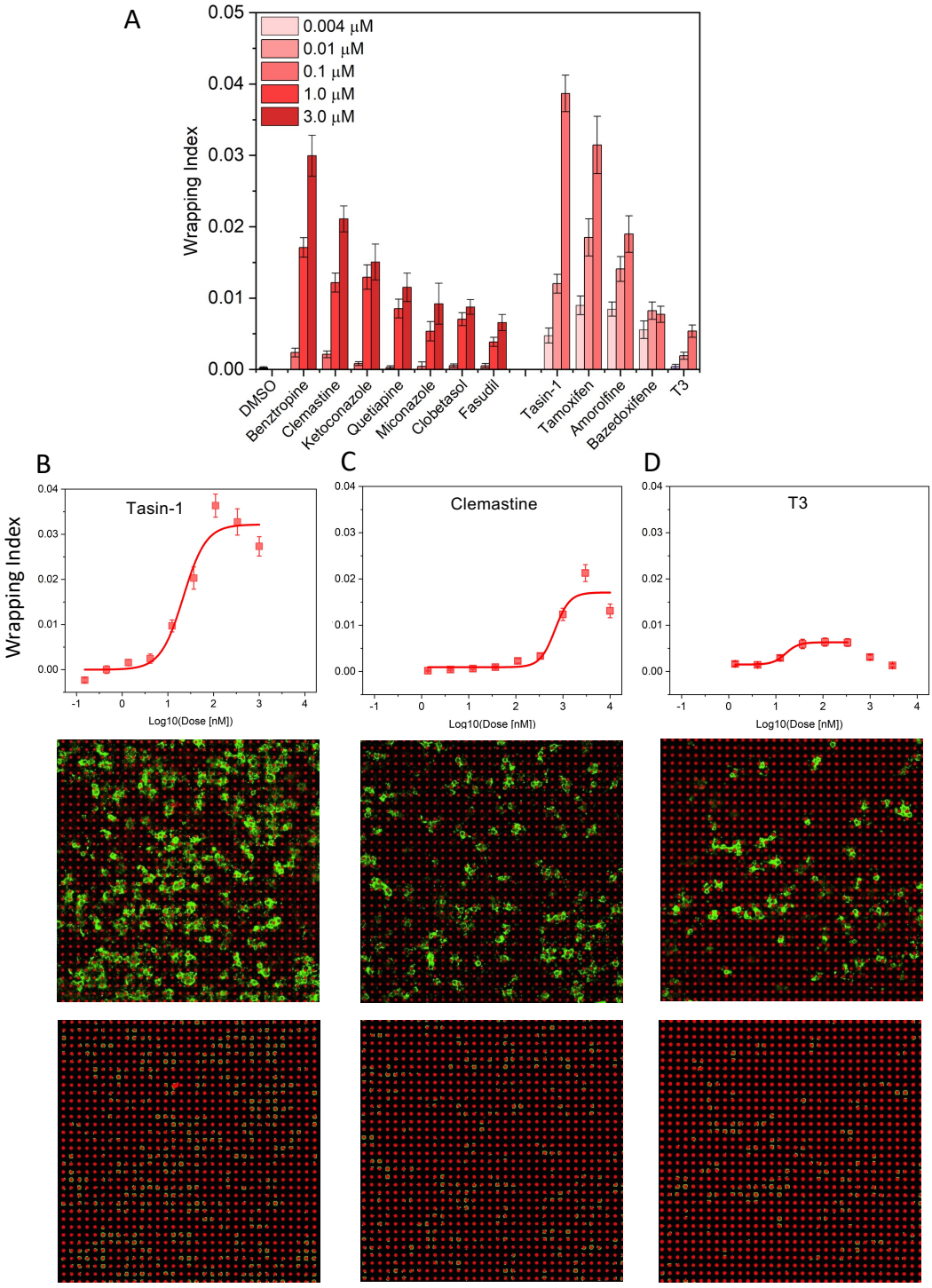

Figure 45 Dose-dependent myelin wrapping of AAs in response to compounds. (A) 3-point series of concentration (taken from 9-point dose response data) illustrate compound's dose-dependent effect on myelin wrapping. (B-D) Top panel: examples of sigmoidal dose-response curves fitted to the wrapping index data for the 9-point concentration series, for, tasin-1, clemastine and T3. The sigmoidal fit excludes concentrations above which the drug induced cytotoxicity. Reported are average values over all fields of view (3 replicates with combined 27 fields of view). Error bars are

standard error of the mean (SEM); Middle panel: examples of MBP staining of myelin wrapping around artificial axons (shown is one field of view at a selected z-plane) corresponding the maximum efficacy dose for tasin-1 (100 nM), clemastine (3 mM) and T3 (100 nM); Bottom panel: processed images from middle panel showing wrapped myelin membrane around artificial axons. Axon diameters are 5 μm.

Traditionally, the capacity of compounds to stimulate myelin wrapping *in vitro* is inferred from 2D differentiation assays. Such 2D assays quantify the relative amount of MBP production, a hallmark of OPC maturation and differentiation into a myelinating oligodendrocyte, rather than the active process of 3D ensheathment by the MBP-containing myelin. Although differentiation is a required step in oligodendrocyte biology to reach a mature stage of the myelinating oligodendrocyte, differentiation and myelin wrapping are distinct processes. We speculated that the compounds' relative ranking could differ for pro-differentiation vs. pro-myelination capacities. We thus conducted a conventional 2D differentiation assay in parallel with the AA assay, using the same preparation of rat OPCs. We performed the differentiation assay using 96-well plates with glass bottom, to match the commonly used conditions for this kind of assay. For most of the compounds, the EC_{50} determined by the wrapping index was noticeably higher than that determined by the 2D MBP area, indicating a 'lag' of actual myelin wrapping with respect to the differentiation and production of MBP-positive membrane (**Figure 46 A**). In other words, for these compounds a higher dose is needed to reach the half-effect on myelin wrapping than on differentiation. The only compound in our assay with the reverse order of EC_{50} was amorolfine. The relative order of compounds based in their EC_{50} and the efficacy values was also different for the myelin wrapping assay compared to differentiation (**Figure 46 A-B**). The comparison of the relative efficacy (expressed as multiple of the T3 maximum effect in respective myelin wrapping and differentiation assays) shows higher values with respect to T3 for myelin wrapping compared to differentiation for most of the compounds (**Figure 46 B**). Overall, the 3D wrapping assay reveals much stronger relative differences between the compounds than the differentiation assay, in addition to a different relative ordering of the compounds'

efficacy. In conclusion, the interpretation of compounds' relative ability to promote myelin wrapping by rat OPCs inferred from a differentiation assay is different from our AA assay, which directly quantifies 3D myelin wrapping. This suggests that the 2D differentiation assays that quantify myelin membrane area may not be good discriminators of compounds' relative pro-myelination potential.

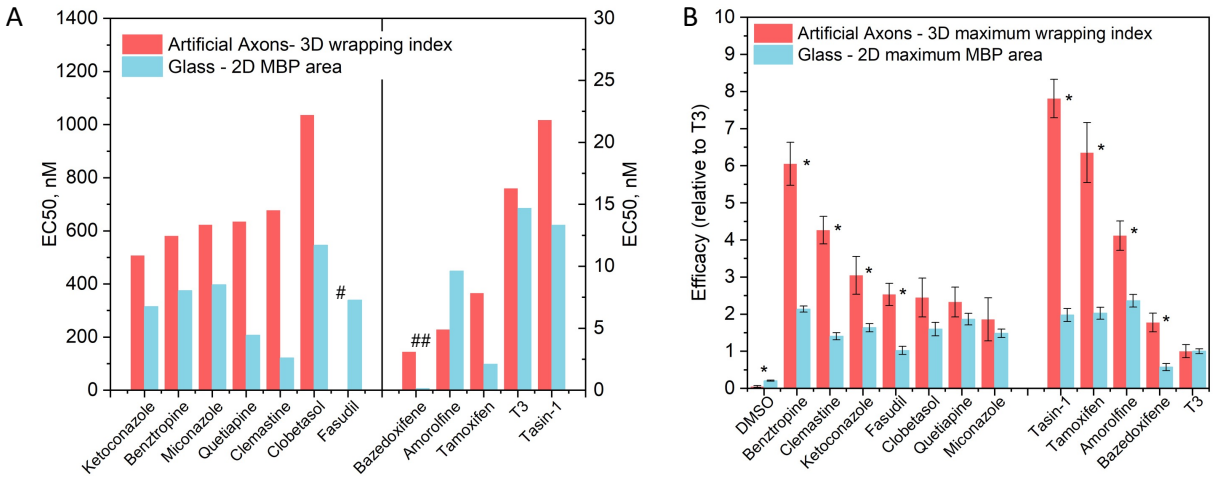

Figure 46 (A) The EC_{50} values (left scale for the compound subset left from the middle line and right scale for the compound subset right from the middle line) and (B) the efficacy values relative to T3, obtained from 9-point dose-response data for wrapping index in 3D myelin wrapping assay (red columns) and for MBP area in 2D differentiation assay (blue columns). The compounds are organized according to the values for myelin wrapping assay, for easier visualization of the different outcomes from the myelin wrapping and differentiation assays. Reported are average values over all fields of view (3 replicates with combined 27 fields of view). Error bars in (B) are standard error of the mean (SEM); In (A) EC_{50} values are obtained from one experimental screen with 3 replicates resulting in one dose-response curve, therefore no SEM is available. * p-value < 0.05.

Next, we leveraged the three-dimensionality of the readout to conduct a more granular analysis of the extent of myelin ensheathment by rat OPCs. For each compound (at the dose corresponding to its highest wrapping index) we considered all the AAs that exhibited any MBP-positive membrane on their surface (0-100% of the AA circumference). Within this set we quantified the percent of AAs at different stages of wrapping, from the least (<50% of AA circumference) to the most engaged or fully wrapped (>80% of AA circumference with the MBP-positive segment length >6 μm)

(**Figure 47**). Note that the darkest green region for each response bar in **Figure 47** represents the percentage of fully wrapped AAs within the considered AAs subset. This morphological analysis revealed further differences among the compounds, showing the highest fraction of fully wrapped AAs for tamoxifen, bazedoxifene, tasin-1, and amorolfine.

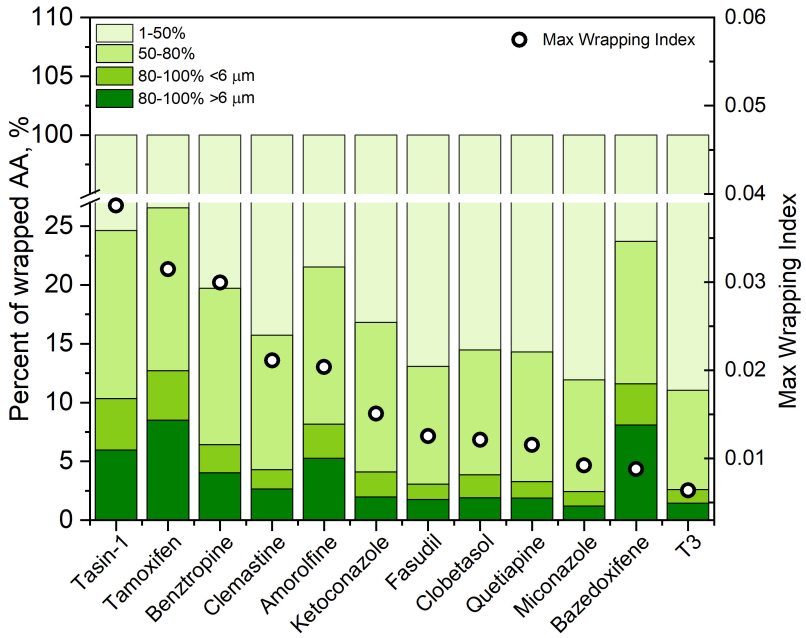

Figure 47 Changes of myelin wrapping extent with compounds concentration. (A) Percentage of AAs with increasing extent of wrapping (<50%, 50-80%, 80-100% and 80-100% with >6 µm myelin segment; left scale) for each compound at its maximum effect (max. wrapping index) (green columns). Mapped on it is maximum wrapping index for each compound (open circles, right scale).

Another unique advantage of AAs is the capacity to quantify the segment length of discrete myelin sheaths along each AA. For each compound (**Figure 48**), we examined the distribution of myelin sheath lengths at each drug concentration. Unlike wrapping index that quantified the cell-normalized number of fully wrapped AAs, the average sheath length did not exhibit any dose-dependence for any compound considered. This suggests that the primary effect of each drug is to influence the *number* of fully wrapped AAs rather than the MBP-positive sheath *lengths* along those AAs. To further verify this interpretation, for each compound we examined the sheath length distribution at the

dosage corresponding to the highest wrapping index. We then generated a probability distribution function of the sheath lengths >6 μm. **Figure 48** shows examples of the length distributions for Tasin-1 and T3 at 110 nM concentration, the dose corresponding to the maximum wrapping index. Even though tasin-1 and T3 exhibited significantly different efficacies as measured by maximum wrapping index, they both showed a similar distribution of sheath lengths. This observation underscores that the primary difference between these compounds was the number of AAs engaged and wrapped by the oligodendrocytes (as quantified by the wrapping index) and not the length of myelin sheaths along those AAs.

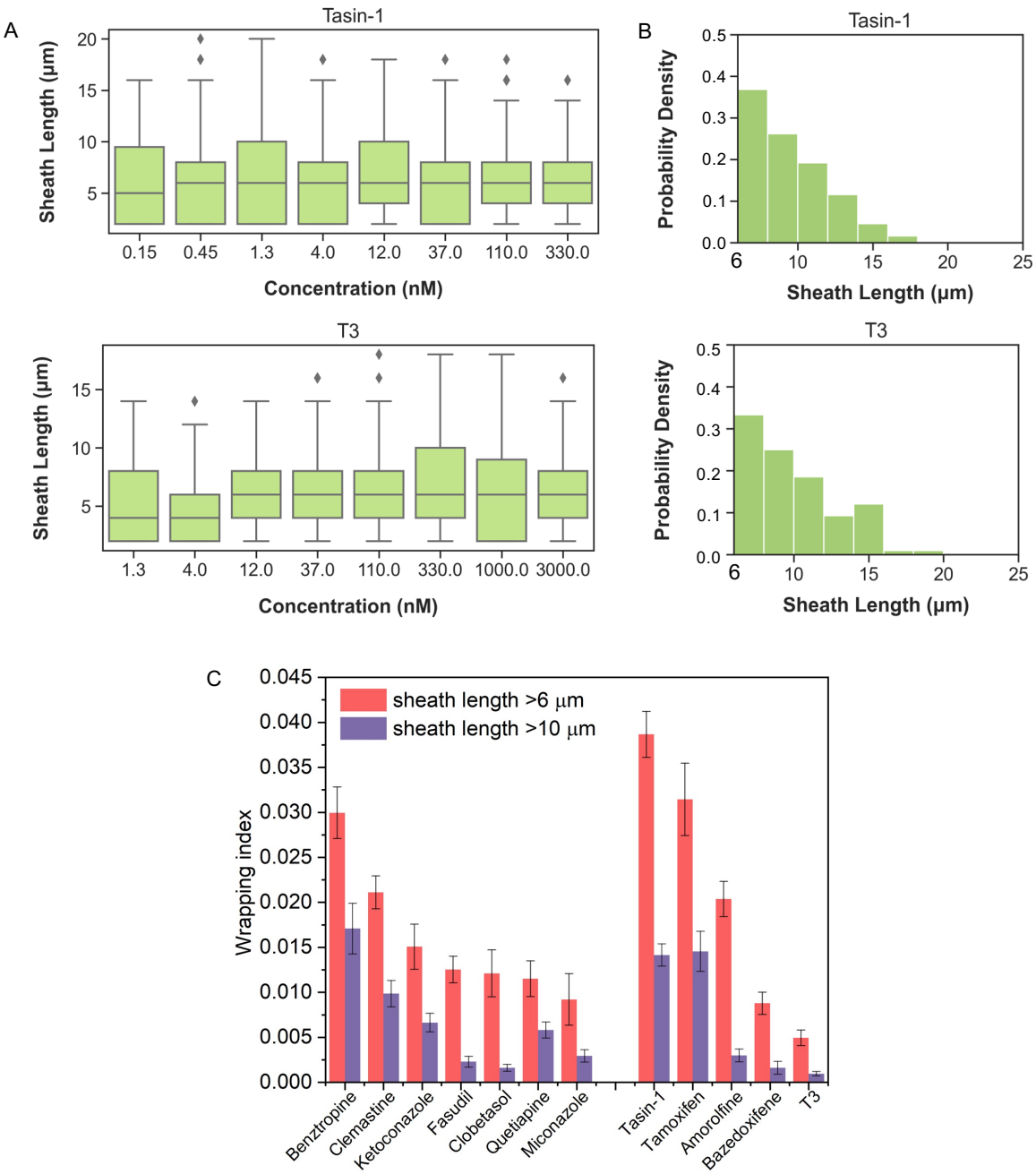

Figure 48 (A) Box plots showing the length distribution of myelin sheaths with >80% of wrapped circumference for tasin-1 and T3 at different drug concentrations. Box represents the interquartile range of 25 (Q1)-75 (Q3) percentile (IQR), whiskers represent data set minimum (Q1-1.5*IQR) and maximum (Q3+1.5*IQR), diamonds represent individual outliers, middle line represents data set median. (B) Normalized histograms showing the length distribution of myelin sheaths >6 µm, for tasin-1 and T3. Histograms were generated for concentrations corresponding to the maximum wrapping index (110 nM for tasin-1 and T3). (C) Comparison of maximum wrapping index for myelin sheath length >6 µm (red) and >10 µm (violet). Error bars are standard error of the mean (SEM) (for 3 replicates with combined n = 27 fields of view).

The wrapping index could be defined alternatively for a different threshold of fully wrapped segment length. **Figure 48 C** illustrates this point for a wrapping index that uses a 10 μm segment length threshold (violet bars). In general, drugs that had a higher maximum wrapping index for 6 μm sheath lengths (red bars) also showed higher numbers of fully wrapped AAs with >10 μm sheaths. However, comparing the two metrics side-by-side in this way can enable identification of disparate responses among drugs, such as to amorolfine, clobetasol and fasudil. Even though these compounds induced high numbers of AAs wrapped with >6 μm sheaths, neither scored well if the threshold for full wrapping was 10 μm sheath length. Taken together, this analysis pipeline allows us to decouple the *number* of AAs wrapped from the *length* of myelin sheaths on those wrapped AAs. By providing different measures to evaluate myelin wrapping extent, such as the number of wrapped AAs and sheath length, which can be used individually or in combination, this platform enables capturing differences in pro-myelinating properties among compounds, not available in other *in vitro* assays.

After systematically characterizing the dose-response of rat OPCs to pro-myelinating drugs, we then compared how the drug responses of hiPSC-derived oligodendroglial cells differed. Since the cell density required for hiPSC-derived cells was much higher, it was not possible to generate enough human oligodendroglial cells to produce a full dose response. Therefore, we instead identified the maximum dose of each drug for rat OPCs (**Figure 49**), and we exposed hiPSC-derived oligodendroglia to that dose for 48 days. Then, we fixed and stained the cells to conduct the same analysis as above. **Figure 49** shows the wrapping index for each drug at its maximum dose (as identified for rat OPCs) for both human and rat OPCs. The y-axis shows the wrapping index relative to T3, the positive control for rat OPCs. Each drug is ranked in reverse consecutive order of wrapping index for the human OPCs. Notably, the top 3 most effective drugs to promote wrapping by human OPCs were Tasin, ketoconazole, and benztropine. In contrast, the 3 most effective drugs for rat OPCs were Tasin, tamoxifen, and amorolfine. These results underscore that the most efficacious drug hits identified through screening

with rat OPCs may be different from those that are most efficacious with human cells. Furthermore, some drugs that were identified to be highly effective in screens with rat OPCs, such as clemastine (>2-fold increase in rat OPC myelin wrapping compared to baseline) were indistinguishable from baseline from the human OPCs. Put together, these results underscore that drug screening with primary rat OPCs can yield different rankings compared to drug screening with hiPSC-derived OPCs. An important caveat here is that we only explored this result for one line of hiPSCs, and for two independent differentiations. Although the result was reproducible across two separate differentiations of the same line, it is very likely that a different cell line may demonstrate different drug efficacies compared to those observed here.

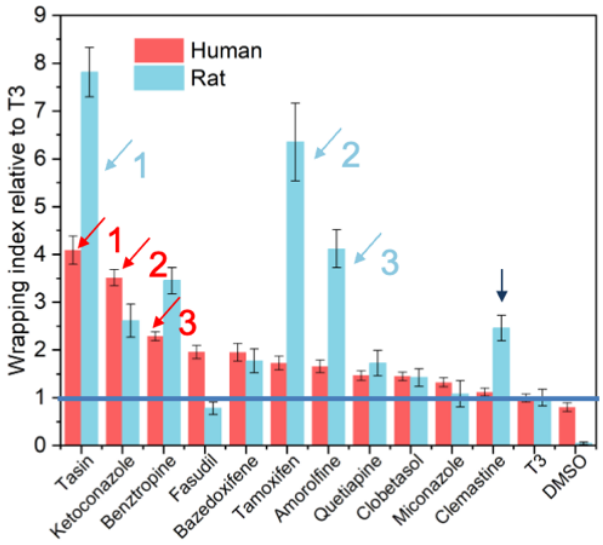

Figure 49 Effect of different pro-myelinating drugs on the wrapping index of human and rat OPCs. The dosage of each drug was selected by choosing the concentration producing the highest wrapping index in rat OPCs. Bars are numbered to emphasize the three most efficacious drugs measured for human and rat OPCs.

In summary, we showed that the effect of these pro-myelinating compounds on myelin wrapping is dose-dependent, and that we can use AAs to generate characteristic dose-response curves for each compound with rat OPCs and determine compounds EC_{50} values and efficacy for myelin wrapping, from sub-nanomolar to micromolar

concentrations. We found that the ranking of efficacy and myelination potency (EC_{50}) among compounds differed significantly between this AA myelin wrapping assay and the corresponding conventional oligodendrocyte differentiation assay (planar deposition of the MBP-positive membrane). Moreover, the dynamic range or relative difference among compounds using the AA myelin wrapping assay was significantly greater than that of the planar differentiation assay. This heightened differential response in the functional result-of-interest (axon engagement and wrapping by the oligodendrocyte) increases the signal-to-noise ratio, potentially helping to discriminate among the compounds.

Further, our 3-dimensional analysis of axon wrapping allows for quantification of myelin sheath length, which is related to the physiological internode length. Interestingly, we observed no significant correlation of the sheath length with compound concentration for this set of compounds. However, we did observe differences among the compounds' potential to induce sheath lengths >6 and 10 μm. Specifically, we observed that three compounds (tasin-1, tamoxifen and benztropine) showed a greater propensity to induce longer myelin sheath lengths. Previous *in vivo* and *ex vivo* quantification of myelin sheath length distributions in murine cell co-culture and brain tissue slice analysis indicates a mean sheath length greater than 10 μm[10,11]. Thus, these unique readouts of the AA wrapping assay such as sheath length has the potential to improve selection of compounds with the ability to induce more physiological wrapping.

Collectively, these results speak to the promise of using AAs as a drug screening platform to discover new pro-myelinating therapeutics, although follow-up experiments are required to both validate these results *in vivo* and also to explore the heterogeneity between different human iPSC donors.

4.4 How APOE3/4 isoform reflects myelin wrapping

In addition to modeling drug response, the AA platform is suited to creating *in vitro* disease models. In Chapter 3, we demonstrated a reductionist model of the MS lesion microenvironment, showing how the presence of exogenous myelin debris

decreased the extent of myelin ensheathment by primary rat OPCs. We also demonstrated a dose-dependence in the effect of microglia on myelin ensheathment. The availability of hiPSC-derived oligodendrocytes opens the door to exploring how human genetic variants, such as documented genetic risk factors for multiple sclerosis (MS), may influence myelin ensheathment by human oligodendroglia.

Both environmental perturbations and genetic risk factors work in tandem to induce MS pathology. One genetic locus of interest is the gene encoding apolipoprotein (ApoE), which is involved in lipid transport and membrane repair. There are three alleles of the *ApoE* gene, designated ApoE2, ApoE3, and ApoE4. Most individuals have the ApoE3 allele, however expression of ApoE4 is correlated with worsened prognosis in MS patients[12]. Furthermore, MRI studies have shown that the ApoE4 genotype is associated with a steeper decline in age-related myelin breakdown[13]. The underlying mechanism by which the ApoE isoform affects remyelination is unclear[14]. One hypothesis is that ApoE4 expression impairs the intrinsic myelination capacity of oligodendrocytes. Another hypothesis is that the ApoE4 genotype in other glial cells such as microglia, which regulate remyelination and debris clearance[15–18].

ApoE is a recognized lipid and cholesterol transporter, and prior studies have shown that the ApoE4 variant changes the structure of the protein's lipid-binding region, in turn affecting cholesterol and lipid transport capacity[19]. In particular, ApoE is a secreted protein that binds to ATP-binding cassette (ABC) transporters ABCA1 and ABCG1 to transfer cholesterol out of the cell, forming extracellular lipoprotein particles[20,21]. Recent studies have also shown that ApoE4 promotes the accumulation of unsaturated triglycerides in iPSC-derived astrocytes compared to ApoE3 cells[22]. Furthermore, gene expression studies of postmortem human brains showed that individuals with the ApoE4 allele exhibited dysregulated lipid metabolism pathways, such as abnormally upregulated genes in cholesterol synthesis pathways (e.g., *SQLE, HMGCR, MVK*) Interestingly, this pathological accumulation of lipids in ApoE4 is also classically associated with risk for Alzheimer's disease[13].

The ApoE3/ApoE4 polymorphism is a single-nucleotide substitution, making it amenable to genetically alter wild-type ApoE3 iPSCs to instead express the ApoE4 isoform (while holding all other factors constant). We obtained an ApoE3 iPSC line from a parental ApoE3 homozygote (provided by Joel Blanchard in the Li-Huei Tsai laboratory), which was edited using CRISPR-Cas9 to produce the corresponding isogenic ApoE4 line (**Figure 50**).

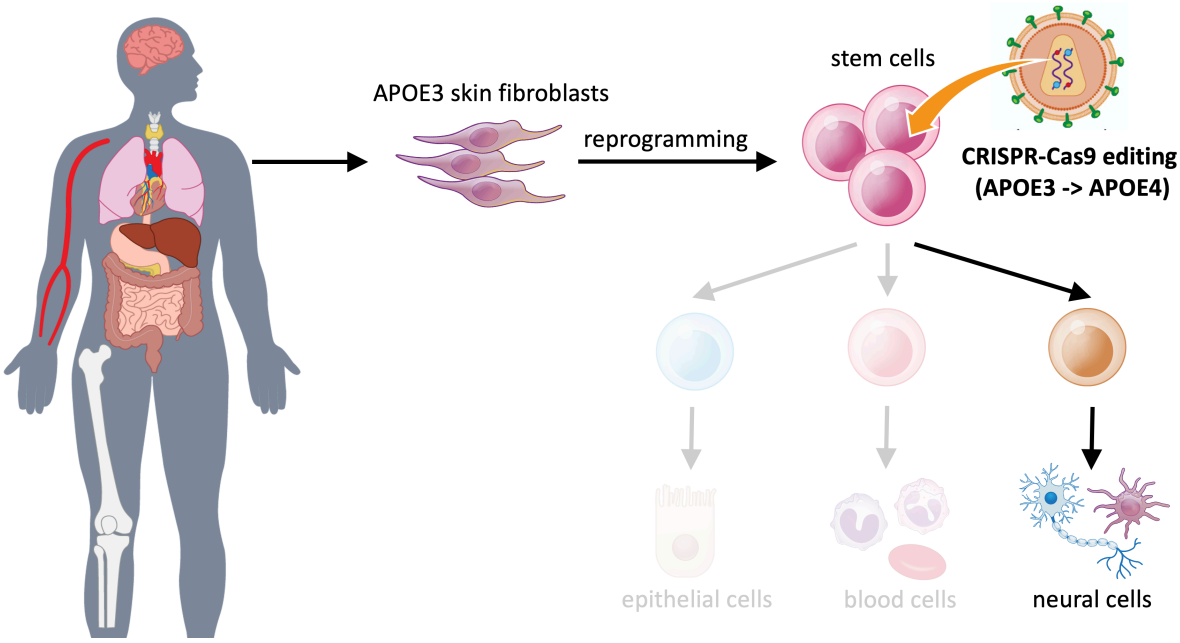

Figure 50 Schematic of process for generating ApoE3 vs. ApoE4 hiPSC cell lines. Individual illustrations designed by Betsy Skrip.

We investigated whether there were differences in the intrinsic myelination potential of ApoE3 vs. ApoE4 hiPSC-derived oligodendroglia. hiPSCs provided a controlled way to investigate these questions since the two cell lines were otherwise isogenic, except for the ApoE polymorphism. One hypothesis is that ApoE4 oligodendrocytes have lower intrinsic myelination potential, which may explain the failure to remyelinate in ApoE4 patients and therefore the worsened MS prognosis. An important caveat is that our experimental design does not address *re*myelination directly (myelination following injury), since there is no *de*myelination component to our model.

However, by exploring the intrinsic capacity of ApoE3 and ApoE4 cells to myelinate, we can speculate about their differential ability to form myelin following injury.

We differentiated the ApoE3 and ApoE4 lines in parallel according to Douvaras and Fossati's protocol and our process optimizations described previously[23]. On day 75, we isolated oligodendroglial cells and plated them on AAs at three different densities: 20k, 50k, and 80k per well. After 42 days of culture, we fixed the cells and stained for MBP. **Figure 51 A** shows the wrapping index for ApoE3 vs. ApoE4 oligodendroglia at each plating density. As expected, we observed an increase in wrapping index as the seeding density increased. Note that in the calculation of wrapping index, the number of fully wrapped pillars is normalized by the number of nuclei present. Therefore, this result was not purely an effect of there being more cells in each condition; instead, when normalized by cell density, the cells were on average wrapping more extensively in the higher-density conditions. In contrast, ApoE4 cells exhibited markedly lower wrapping indices at all cell densities explored, which suggests that ApoE4 cells may indeed have lower intrinsic myelination potential.

We also investigated whether using a different readout for quantifying myelin would affect the measured performance of ApoE3 vs. ApoE4. Instead of our 3D myelin wrapping readout, we also quantified the 2D projected area of MBP expression. **Figure 51** shows that at low cell densities (20k and 50k), the difference in MBP expression was indistinguishable, whereas it was only at 80k density that ApoE4 was observed to have lower MBP expression than ApoE3. These further reinforce our earlier results that the measured performance of oligodendrocytes can differ between 2D and 3D readouts, and that the extent of 2D MBP deposition does not always correlate with 3D wrapping. For example, there may be differences in 3D myelin ensheathment between cell lines that are missed when only 2D readouts are used.

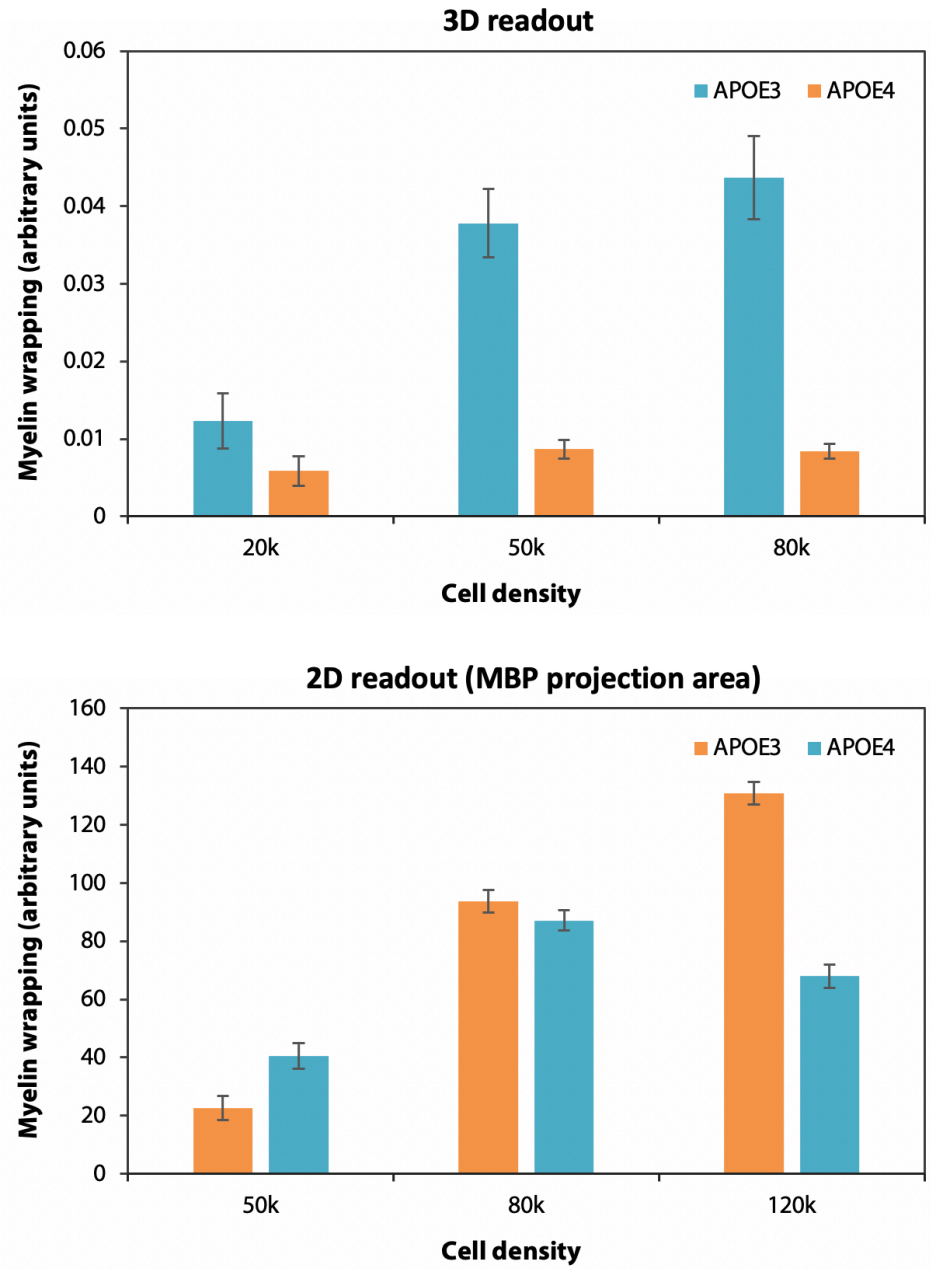

Figure 51 Comparison of wrapping index and 2D myelin deposition of ApoE3 vs. ApoE4 hiPSC-derived oligodendrocytes, at three different cell seeding densities. Error bars show standard error of the mean (SEM).

Next, we explored whether the wrapping index of ApoE4 cells could be boosted. We hypothesized that feeding the hiPSC-derived oligodendroglia with conditioned media from neuronal cultures could increase OPC differentiation through paracrine signaling effects. Therefore, we cultured both ApoE3 cells in conditioned and unconditioned media

for 42 days and measured the wrapping index. **Figure 52** shows that there was no benefit to using conditioned media for ApoE3 cells, and that there was a small but not significant boost to wrapping index for ApoE4 cells. These results indicate that media conditioning was not an effective approach for 'rescuing' myelin wrapping for ApoE4 cells.

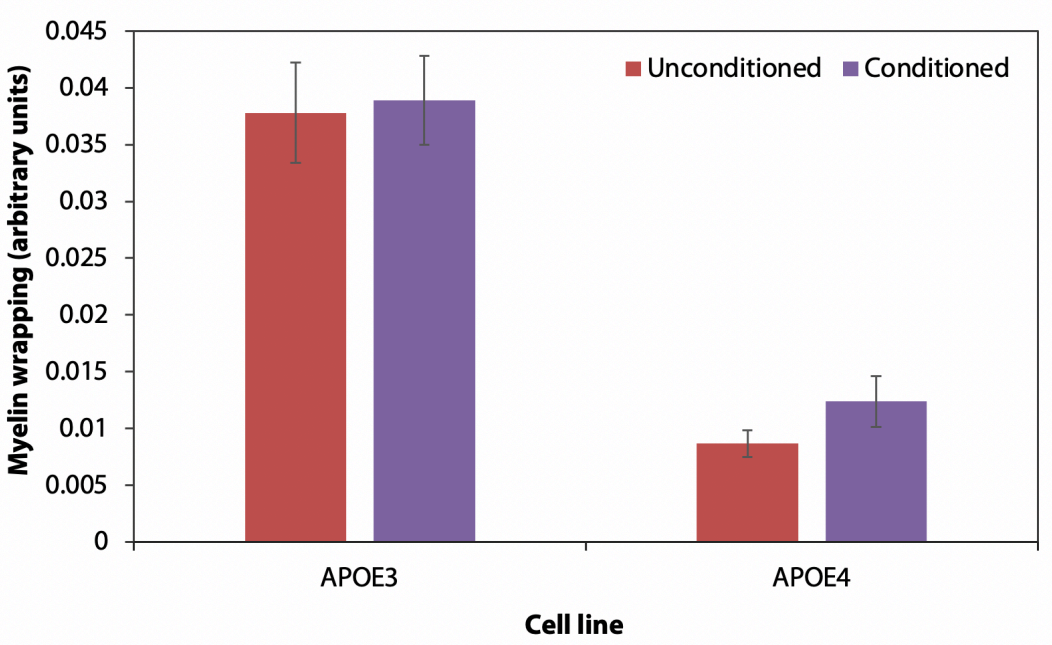

Figure 52 Wrapping index of ApoE3 vs. ApoE4 hiPSC-derived oligodendroglia in the presence of unconditioned and conditioned media. Conditioned media were obtained from culture of iPSC-derived neurons, obtained from the Li-Huei Tsai laboratory. Error bars show standard error of the mean (SEM).

Next, we explored how different small-molecule pro-myelinating drugs could differentially affect ApoE3 vs. ApoE4 cells. This work was informed by a recent seminal paper showing that many previously identified promyelinating drugs all actually affect the same underlying cholesterol metabolism pathway[24] (**Figure 53**). In particular, many pro-myelinating drugs act not through their canonical targets but instead through inhibiting enzymes like CYP51, TM7SF2, or EBP, which are all found within the same section of the cholesterol metabolism pathway. As a result, these drugs lead to the accumulation of the enzymatic substrates, which are all 8,9-unsaturated sterols. Studies

have shown that direct inhibition of these enzymes lead to increased OPC differentiation and MBP expression, and that directly supplying the unsaturated sterols to OPCs also yields the same effect. However, these studies were only performed on wild-type, ApoE3 cells. Therefore, we aimed to explore how different pro-myelinating drugs, including those that do and do not affect cholesterol metabolism, may have differential effects on ApoE3 vs. ApoE4 hiPSC-derived oligodendroglia.

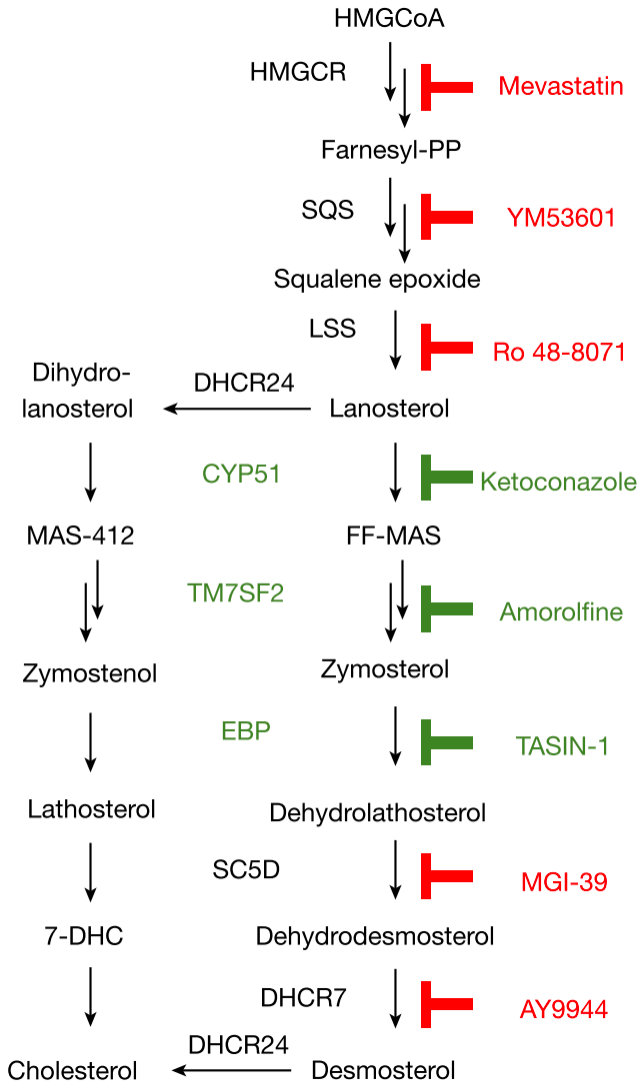

Figure 53 Cholesterol metabolism pathway targeted by many canonical pro-myelinating drug compounds. From[24]

We cultured APOE3 vs. APO4 hiPSC-derived oligodendroglia in the presence of five different pro-myelinating drugs, at the dosage identified earlier in this chapter. After 42 days of culture, we fixed and stained the cells for MBP (protocol in Appendix). **Figure 54** shows the results from one independent differentiation of cells. Notably, many drugs that are canonically promyelinating are *only* beneficial to ApoE3 cells. In particular, drugs like Tasin and ketoconazole actually lead to reduced myelin wrapping in ApoE4 cells compared to the baseline DMSO control. Furthermore, drugs that do not target components of the cholesterol biosynthesis pathway did not exhibit such large differences between ApoE3 and ApoE4 cells.

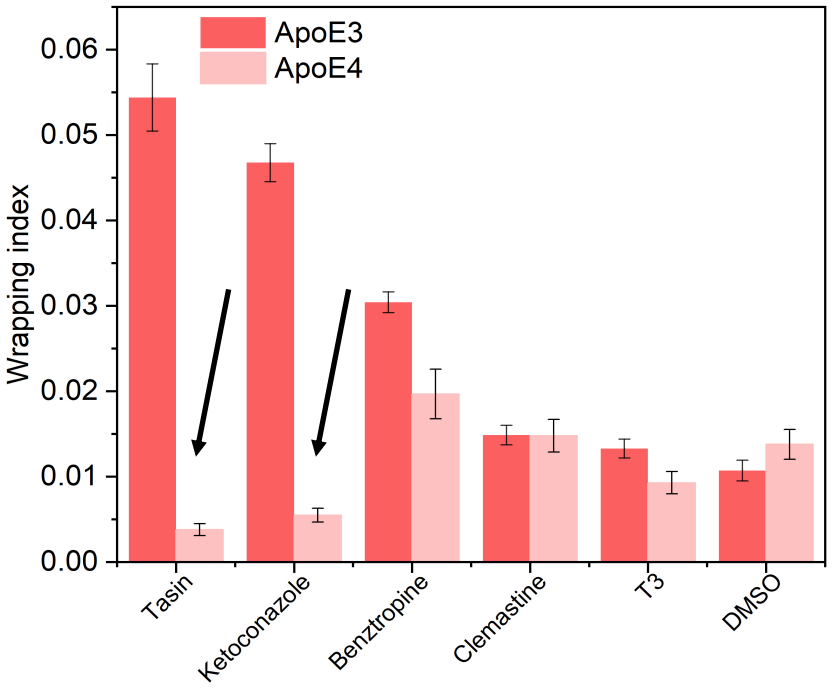

Figure 54 Differential response of ApoE3 vs. ApoE4 hiPSC-derived oligodendrocytes to different pro-myelinating compounds. Drugs that promote accumulation of 8,9-unsaturated sterols were beneficial for wrapping index in ApoE3 cells but were detrimental to ApoE4 cells.

Based on these results, we hypothesize that the accumulation of cholesterol precursors is *only* beneficial for ApoE3 cells and not for ApoE4. We hypothesize that there is a dose-dependence to the benefit of accumulating 8,9-unsaturated sterols. In

wild-type ApoE3 cells, sterol accumulation is beneficial as previously reported. However, in ApoE4 cells there is already a pre-existing accumulation of cholesterol precursors due to the impaired cholesterol efflux from the cell. We speculate that there exists a threshold intracellular cholesterol concentration at which the beneficial impact of 8,9-unsaturated sterols is maximized, but concentrations above this threshold may be cytotoxic. For example, this would be consistent with many other known dysmyelinating diseases in which cytotoxic lipid accumulation is the primary driving force underlying dysmyelination. For example, X-linked adrenoleukodystrophy (X-ALD) is caused by mutations in the *ABCD1* gene. The *ABCD1* gene encodes the adrenoleukodystrophy protein (ALDP)[25]. ALDP is localized to the peroxisome membrane and transports very long chain fatty acids (VLCFAs) into the peroxisome lumen for degradation. Consequently, VLCFAs accumulate within cells, which is thought to lead to mitochondrial dysfunction and oxidative damage that causes oligodendrocyte apoptosis during development[5]. In sum, we hypothesize that accumulating 8,9-unsaturated sterols is only beneficial for oligodendrocytes in which there was a healthy intracellular concentration of cholesterol to begin with; in contrast, cells that begin with elevated intracellular concentrations of cholesterol do not benefit from these pharmacological perturbations. Further studies are required to verify this mechanism, which will be outlined in Chapter 5.

4.5 Materials and Methods

Fabrication of AAs

We have previously developed a proprietary process to fabricate vertical free-standing artificial axons with diameters of ~5-8 μm, heights of ~20 μm, and tunable stiffness ranging from sub-kilopascals to ~140 kPa, to mimic biological axons[26–28], which were previously 3D-printed on glass cover slips[19]. In this work, we expanded this technology to 3D-print our custom-developed resin (HsP, 140 kPa)[28,29] directly in the wells of 96-well glass-bottom plates using masked near-UV light and our new custom-built 3D printing setup. The updates to the new 3D printing system included the new light engine, modified optics, improved translational stage accuracy and areal coverage, integrating a tissue culture plate, as well as the corresponding automated software environment with a GUI for customizable operation, resulting in superior reproducibility and rapid fabrication of AAs in 96-well plates. Before cell plating, the AAs were functionalized with poly-D-ornithine (50 mg/ml, 24 h incubation in 37^{o}C) followed by incubation with laminin (20 mg/ml, 24 h, 4^{o}C) and stored in 4^{o}C.

3D myelin wrapping assay and dosing with compounds

Rat oligodendrocyte progenitor cells (rOPCs) were isolated from neonatal rat brains (P1) using magnetic sorting with beads coated with anti-A2B5 antibodies (Miltenyi, 130-093-392). The isolated cells were expanded in tissue culture flasks for 2-3 days, in the proliferation media (DMEM/F12 (Gibco, 11330-032), Penicilin-Streptomycin (Gibco, 15140-12), B27 (Gibco, 12587-010), PDGF (platelet-derived growth factor, ThermoFisher PHG0035) and FGF (fibroblast growth factor, (ThermoFisher PHG0024) at the concentration of 10 ng/ml each. Expanded rOPCs were plated in 96-well plates containing in each well AAs functionalized with poly-D-ornithine/laminin at a density of 20,000 cells per well of a 96-well plate in 150 ml of the differentiating medium (DMEM/F12, Penicilin-Streptomycin, B27, PDGF and FGF at the reduced concentration of 2 ng/ml each). Only the inner 60 wells were used to avoid the drying effect of the outer-most wells. Plating day was considered day 0 of cell culture. Cells were allowed to attach to AAs for 24 hours. Starting with day 1, rOPCs were dosed with

compounds every 2-3 days by replacing 50 ml of old media with fresh media containing compound (Monday-Wednesday-Friday schedule), for the total of three repeated doses. Cells were fixed on day 7, followed by immunostaining for myelin basic protein (MBP). For each compound, we applied 9 concentrations obtained by 3x serial dilutions, starting from the highest concentration of either 10 mM (for benztropine, clemastine, clobetasol, fasudil, ketoconazole, miconazole, quetiapine, and T3), or 1 mM (for tasin-1, tamoxifen, amorolfine, bazedoxifene). As the control condition we used medium containing 0.1% DMSO, which was the solvent vehicle for the compounds. The compounds were provided by Sanofi as 10 mM stock in DMSO. Each condition was repeated in triplicate.

2D differentiation assay

In parallel with the 3D myelin wrapping assay, a companion 2D differentiation assay was conducted using the same rOPC cell batch, plate functionalization with poly-D-ornithine/laminin, cell culture and dosing protocol, and assay duration (7 days). For this 2D assay, rOPCs were plated in the 96-well glass bottom plates (60 inner wells) at a density of 10,000 cells per well.

Enzyme-linked immunosorbent assay (ELISA) analysis of myelin basic protein (MBP)

Standard sandwich ELISA was performed using the following antibodies diluted in PBS (coating antibody) or PBS containing 1% bovine serum albumin (all other antibodies). Coating antibody: monoclonal anti-MBP (1:2500, Millipore Cat# MAB382, RRID:AB_94971); detection antibody: polyclonal anti-MBP (1:2500, Abcam Cat# ab28541, RRID:AB_776581); biotinylated goat anti-rabbit IgG antibody (1:10,000, Vector Laboratories Cat# BA-1000, RRID:AB_2313606), streptavidin-biotinylated HRP complex (1:8000, GE Healthcare, Chicago, USA). Cells harvested at 3- and 6-days post treatment were lysed in triple detergent buffer (50 mM Tris-HCl, pH 8.0, 150 mM sodium chloride, 0.02% sodium azide, 0.1% sodium dodecyl sulfate, 1.0% NP-40, 0.5% sodium deoxycholate, all from Sigma) containing 1X Complete Mini, EDTA-free Protease Inhibitor

Cocktail (Roche, Mannheim, Germany). Known concentrations of recombinant bovine MBP (Invitrogen) were used to generate a standard curve. Standards and cell lysates were added to 96-well Maxisorp plates (Nunc, ThermoFisher) pre-coated with coating antibody and incubated overnight at 4°C. Plates were washed three times with phosphate buffered saline containing 0.5% Tween-20 (Sigma) (PBST) using an automated microplate washer (405 TS, BioTek Instruments Inc. Winooski, USA). Plates were then incubated at room temperature with detection antibody (2 hours), biotinylated anti-rabbit IgG (1 hour), and streptavidin-biotinylated HRP complex (1 hour) with three washes with PBST between each incubation step. To induce colorimetric change, o-phenylenediamine dihydrochloride (OPD) (Sigma) was added to each plate for 30 minutes and the reaction stopped by addition of 2N sulfuric acid (RICCA). Total MBP concentration was determined by colorimetric change of plates read at 492nm using the FlexStation® 3 Multi-Mode Microplate Reader (Molecular Devices, San Jose, USA). Total protein concentration in the lysates were determined by Bicinchoninic Acid Assay (BCA) Protein Assay (Pierce, ThermoFisher) according to the manufacturer's instructions.

Immunostaining

Cells were fixed with 4% paraformaldehyde (PFA, Electron Microscopy Sciences 15714-S) in two steps, by first applying 4% PFA in cell media for 15 min, at room temperature (to avoid rapid change from media to PBS), followed by applying 4% PFA in PBS for 15 min. Next, cells were washed 3 times with PBS and permeabilized with 0.2% Triton -X, for 3 min. Cells were then washed 3 times with wash buffer (PBST: PBS/0.01% Tween) and blocked with 5% goat serum in PBST for 1 h. Cells were then incubated with the primary antibody against MBP, the marker of myelin membrane, (BioRad, rat anti-MBP, MCA409, 1:200 dilution) for 24 h, in 4^{o}C. Next cells were washed 3 times with PBST and incubated with secondary antibody (Alexa-Fluor-647, goat anti-rat, ThermoFisher, A-21247, 1:200 dilution), for 1 h. Cells were then washed 3 times with PBST and incubated with DAPI (ThermoFisher, 62248, 1:1000 dilution) for 5 min. After washing 3 times with PBST, cells were stored in PBS in in 4^{o}C.

Fluorescence imaging

Immunostained samples were imaged either in three channels, for AAs samples (rhodamine for AAs, Alexa-Fluor 647 for myelin, and DAPI for nuclei) or in two channels for 2D differentiation samples (Alexa-Fluor 647 for myelin, and DAPI for nuclei) using a confocal microscope (Olympus, FluoView 3000) and 20x air lens. To image 3D myelin wrapping around axon mimics, for each well of the 96-well plate we collected z-slice images (10 slices, with z-step of 2 μm) in 9 fields of view evenly spaced across the well. Collectively ~10,000 AAs were imaged and analyzed per well. For the 2D differentiation samples, single plane images were collected in 9 fields of view per well.

Quantification of 3D myelin wrapping on AAs

The collected fluorescence z-slice images were processed using Fiji[30] software and custom-developed protocols to obtain the thresholded binary masks of myelin, axons, and nuclei channels; and the 3D data of myelin wrapping around each axon, including percent of wrapping around axon circumference for each z-slice, and the length of myelin segments along each axon (in z-direction). Using these data, we quantified the number of axons with different percentage of MBP-positive membrane wrapping around axon circumference, for ranges of 0-20%, 20-50%, 50-80%, and 80-100% with at least one z-slice, and a number of axons with 80-100% wrapping and a continuous MBP-positive membrane segment length of at least 6 μm (three z-slices), referred here as “full wrapping”. For each imaged field of view, we quantified “wrapping index”, as the number of fully wrapped axons divided by the number of nuclei. The reported here data are averages over all fields of view.

Quantification of 2D differentiation

Single-plane images of samples from the 2D differentiation assay were processed using Fiji to obtain thresholded masks of MBP-positive membrane. The area was quantified as

a measure of cell differentiation for each field of view. The data reported here are averages over all fields of view.

Compounds potency (EC_{50}) and efficacy

The 9-point dose-response data, measured as “wrapping index” for 3D myelin wrapping assay, or as MBP area for 2D differentiation assay, were fitted to sigmoidal curve model using Origin Pro (OriginLab Corporation) data analysis software. The reported values of compound’s potency - EC_{50} or the effective compound’s concentration to induce 50% of maximum effect - were obtained from the fitted curves; the efficacy (the maximum compound’s effect) was reported directly from the obtained data points.

Statistical analysis

The 3D myelin wrapping and 2D differentiation assays to obtain dose responses to compounds were performed in triplicate (3 wells). For each well we analyzed images from 9 fields of view per well, with ~10,000 AAs analyzed for the 3D myelin wrapping experiment and MBP-positive area analyzed for the 2D differentiation experiment. The reported data are averages over all fields of view. The one-way ANOVA was used to determine statistical significance of differences between the compared conditions.

4.6 References

1. Wang, L. L. W. *et al.* Cell therapies in the clinic. *Bioeng. Transl. Med.* **6**, (2021).
2. Gottipamula, S., Bhat, S. & Seetharam, R. N. Mesenchymal Stromal Cells: Basics, Classification, and Clinical Applications. *J. Stem Cells* **13**, (2018).
3. Rajabzadeh, N., Fathi, E. & Farahzadi, R. Stem cell-based regenerative medicine. *Stem Cell Investig.* **6**, (2019).
4. Zakrzewski, W., Dobrzyński, M., Szymonowicz, M. & Rybak, Z. Stem Cells: Past, Present and Future. *IEEJ Trans. Fundam. Mater.* **128**, 329–332.
5. Zhu, J. *et al.* The Changing Face of Adrenoleukodystrophy. *Endocrine Reviews* vol. 41 (2020).
6. Leclerc, T. *et al.* Cell therapy of burns. *Cell Prolif.* **44**, 48–54 (2011).
7. Takahashi, K. *et al.* Induction of Pluripotent Stem Cells from Adult Human Fibroblasts by Defined Factors. *Cell* **131**, 861–872 (2007).
8. Douvaras, P. *et al.* Efficient generation of myelinating oligodendrocytes from primary progressive multiple sclerosis patients by induced pluripotent stem cells. *Stem Cell Reports* **3**, 250–259 (2014).
9. Rosenberg, S. S., Kelland, E. E., Tokar, E., De La Torre, A. R. & Chan, J. R. The geometric and spatial constraints of the microenvironment induce oligodendrocyte differentiation. *Proc. Natl. Acad. Sci. U. S. A.* **105**, 14662–14667 (2008).
10. Bechler, M. E., Byrne, L. & Ffrench-Constant, C. CNS Myelin Sheath Lengths Are an Intrinsic Property of Oligodendrocytes. *Curr. Biol.* **25**, 2411–2416 (2015).
11. Murtie, J. C., Macklin, W. B. & Corfas, G. Morphometric Analysis of Oligodendrocytes in the Adult Mouse Frontal Cortex. *J. Neurosci. Res.* **3253**, 3244–3253 (2007).
12. Masterman, T. *et al.* APOE genotypes and disease severity in multiple sclerosis. *Mult. Scler.* **8**, 98–103 (2002).
13. Bartzokis, G. *et al. Apolipoprotein E Genotype and Age-Related Myelin Breakdown in Healthy Individuals Implications for Cognitive Decline and Dementia. Arch Gen Psychiatry* vol. 63 (2006).
14. Fazekas, F. *et al.* The impact of our genes: Consequences of the apolipoprotein E polymorphism in Alzheimer disease and multiple sclerosis. *J. Neurol. Sci.* **245**, 35–39 (2006).
15. Kıray, H., Lindsay, S. L., Hosseinzadeh, S. & Barnett, S. C. The multifaceted role of astrocytes in regulating myelination. *Experimental Neurology* vol. 283 541–549 (2016).

16. Olah, M. *et al.* Identification of a microglia phenotype supportive of remyelination. *Glia* **60**, 306–321 (2012).
17. Cignarella, F. *et al.* TREM2 activation on microglia promotes myelin debris clearance and remyelination in a model of multiple sclerosis. *Acta Neuropathol.* **140**, 513–534 (2020).
18. Neumann, H., Kotter, M. R. & Franklin, R. J. M. Debris clearance by microglia: An essential link between degeneration and regeneration. *Brain* vol. 132 288–295 (2009).
19. Yamazaki, Y., Zhao, N., Caulfield, T. R., Liu, C. C. & Bu, G. Apolipoprotein E and Alzheimer disease: pathobiology and targeting strategies. *Nat. Rev. Neurol.* **15**, 501–518 (2019).
20. Karten, B., Campenot, R. B., Vance, D. E. & Vance, J. E. Expression of ABCG1, but not ABCA1, correlates with cholesterol release by cerebellar astroglia. *J. Biol. Chem.* **281**, 4049–4057 (2006).
21. Wahrle, S. E. *et al.* ABCA1 is required for normal central nervous system apoE levels and for lipidation of astrocyte-secreted apoE. *J. Biol. Chem.* **279**, 40987–40993 (2004).
22. Sienski, G. *et al.* APOE4 disrupts intracellular lipid homeostasis in human iPSC-derived glia. *Sci. Transl. Med.* **13**, 1–11 (2021).
23. Douvaras, P. & Fossati, V. Generation and isolation of oligodendrocyte progenitor cells from human pluripotent stem cells. *Nature Protocols* vol. 10 1143–1154.
24. Hubler, Z. *et al.* Accumulation of 8,9-unsaturated sterols drives oligodendrocyte formation and remyelination. *Nature* **560**, 372–376 (2018).
25. Moser, H. W., Mahmood, A. & Raymond, G. V. X-linked adrenoleukodystrophy. *Nat. Clin. Pract. Neurol.* **3**, 140–151 (2007).
26. Espinosa-Hoyos, D. *et al.* Engineered 3D-printed artificial axons. *Sci. Rep.* **8**, 1–13 (2018).
27. Vliet, K. J., Jagielska, A., Homan, K., Lewis, J. & Busbee, T. A. Neuronal Axon Mimetics For In Vitro Analysis Of Neurological Diseases, Myelination, And Drug Screening. vol. 2 (2020).
28. Espinosa-Hoyos, D., Jagielska, A., Du, H., Fang, N. X. & Van Vliet, K. J. Engineered 3D-Printed Artificial Axons. vol. 1 (2018).
29. Espinosa-Hoyos, D., Du, H., Fang, N. X. & Van Vliet, K. J. Poly(HDDA)-Based Polymers for Microfabrication and Mechanobiology. *MRS Adv.* **2**, 1315–1321 (2017).
30. Schneider, C. A., Rasband, W. S. & Eliceiri, K. W. *NIH Image to ImageJ: 25 years of Image Analysis HHS Public Access*. *Nat Methods* vol. 9 (2012).

5. Conclusions and outlook

5.1 Conclusions

In this thesis, I advanced the Artificial Axon (AA) platform to create *in vitro* models of myelination, with a particular emphasis on recapitulating lesion-like environments in myelination diseases.

In Chapter 2, we built a new high-resolution 3D printer (HR-3DP) that was compatible with fabricating AAs directly within a multi-well plate format. This significantly increased production throughput; whereas it previously took two weeks to fabricate AAs to fill a 96-well plate, the process now requires just one hour. We also designed a graphical user interface through which the HR-3DP operator can automate AA fabrication across the entire well plate, with custom geometries within each well. I further demonstrated how varying physicochemical parameters during printing, such as UV light intensity and exposure duration, could achieve micron-scale control over AA diameter and interaxonal spacing. Furthermore, I demonstrated that the lowest limit of AA diameters that can be reproducibly fabricated is ~1.5 μm, which is very close to the micrometer-level diameter of biological axons in neural tissue. In contrast, such low-diameter axons had been previously unattainable with the first-generation 3D printer, since the extensive sample handling requirements would damage these low-diameter axons. I demonstrated that the AAs fabricated through the HR-3DP were biocompatible, since primary rat OPCs seeded on the AAs can differentiate into MBP+ producing oligodendrocytes within seven days of culture, fully ensheathing the AAs with myelin. Finally, we used transmission electron microscopy to image the ultrastructure of myelin around the AAs. Although we did not identify the presence of compact, multilaminar myelin, I established methodological best practices for this imaging process, for example using fiduciaries to identify regions of interest, fabricating AAs and culturing OPCs within chamber slides, and also avoiding membrane permeabilization, which degrades

myelin integrity. Future work will continue to explore the ultrastructure of myelin to determine whether there are regions of compact myelin ensheathed around the AAs.

In Chapter 3, we leveraged the tunability of the AAs to model lesion-like environments. First, I demonstrated the tunability of AA Young's moduli by varying the ratio of 4-arm PEG acrylate (starPEG) and 1,6-hexanediol diacrylate (HDDA) to achieve different polymer crosslinking densities. Using AFM-enabled indentation, we determined that AAs had Young's moduli E ranging from 13000 Pa to 98 Pa. Such low-stiffness axons had previously been unattainable the first-generation 3D printer due to disproportionate sample damage to the compliant AAs. Using an in-house image analysis pipeline that quantifies myelin ensheathment in 3D, we demonstrated the independent effects of AA stiffness, diameter, and density on myelin ensheathment by primary rat OPCs. Importantly, this analysis approach distinguished between the *number* of axons wrapped by oligodendrocytes and the *length* of myelin sheaths deposited on the wrapped axons. Within the range of Young's moduli explored (E = 100 Pa, 800 Pa, 13000 Pa), we found that higher-stiffness axons correlated with a higher number of ensheathed AAs, with no effect on the length of myelin sheaths deposited. Within the range of axon diameters explored (3 μm, 7 μm, 12 μm), we found that increasing diameter led to a reduction in the number of AAs ensheathed, with a concomitant decrease in the length of myelin along those AAs. These results raise the possibility that axon stiffness and diameter may play a causal role in affecting oligodendrocytes' propensity to myelinate. We also explored the response of primary rat OPCs to pro-myelinating compounds stiff (E = 13 kPa) vs. compliant (E = 0.8 kPa) AAs, and found that the relative efficacies of the drugs differed between the stiff vs. compliant axons. This result underscores the importance of studying myelination within mechanically representative environments. For example, current drug screens typically use tissue-cultured polystyrene as the OPC culture substratum, which has a Young's modulus several orders of magnitude above that of brain tissue. Based on these results, it is possible that the behavior and drug response of OPCs in these mechanically stiff environments does not represent their behavior *in vivo*. Finally, to validate the AA platform, we investigated the impact of exogenous myelin debris on OPC

myelination. Based on *in vivo* results that myelin debris inhibits remyelination, we similarly found a dose-dependent effect whereby higher concentrations of myelin debris led to a concomitant reduction in AA ensheathment by rat OPCs. These results suggest that the AA platform can be used to model lesion-like environments and recapitulate results obtained from *in vivo* animal disease models. Furthermore, this chapter underscores the utility of a deliberately reductionist model like AAs, where complexity can be layered in piece-by-piece to disentangle the many biomarkers correlated with disease states.

In Chapter 4, we demonstrated the compatibility of AAs with human oligodendrocytes derived from human induced pluripotent stem cells (hiPSCs). We adapted the Douvaras and Fossati protocol to reproducibly derive human oligodendrocytes that ensheathed AAs with MBP+ myelin. For example, we found a critical cell seeding density (80k cells per well) that resulted in reproducible MBP expression. We also demonstrated that freeze-thawing and passaging the oligodendroglia generated by this protocol completely eliminated MBP production, which speaks to the need to identify alternative approaches to increase cell production throughput. We further compared the drug response of hiPSC-derived OPCs and primary rat OPCs, identifying that the relative efficacies of drugs differed between human and rat oligodendrocytes. There are some important methodological caveats to interpreting these data: firstly, we only used one human cell line from a single donor. Although the results were consistent across multiple rounds of differentiation for this iPSC line, there is considerable heterogeneity between human donors, which may lead to different drug efficacies for a different cell line. Furthermore, although hiPSC-derived oligodendrocytes are similar to endogenous oligodendrocytes, they do differ in important ways, for example exhibiting distinct gene expression profiles. Nonetheless, these results speak to the importance of using human oligodendrocytes, since the drug hits identified by rat oligodendrocytes may differ from those that are most efficacious for human cells. Finally, we combined hiPSCs with CRISPR-Cas9 editing to determine the effect of the ApoE genotype on myelination. Prior clinical results indicate that individuals with the

ApoE4 allele have worsened MS prognosis compared to individuals with the ApoE3 allele, although the precise underlying reasons are unclear. We found that ApoE3 iPSC-derived oligodendrocytes had higher wrapping index compared to ApoE4 oligodendrocytes. Furthermore, ApoE3 and ApoE4 oligodendrocytes exhibited markedly different responses to pro-myelinating compounds, where ApoE3 cells were benefited by drugs that raised 8,9-unsaturated sterols, whereas the same drugs decreased myelin wrapping for ApoE4 cells. We hypothesize that since the ApoE4 allele is correlated with an intracellular accumulation of cholesterol, that further elevating unsaturated sterols in ApoE4 OPCs is detrimental to myelination.

5.2 Future outlook

Although we reported fabricating axons with diameters of 1.5 μm, future experiments can further attempt to reduce the diameter to reach sub-micron biological ranges. A limitation of the current hardware is that the UV projector has a residual background light, which minimizes the contrast between the AA mask and the dark background. The background light may cause diffuse initiation of off-target free radicals (outside of the intended polymerization region), thus producing AAs that are wider than intended. Future work can explore methods to filter the incident UV light or explore other alternative projector hardware with higher contrast and reduced background light. Another opportunity to more granularly adjust the AA geometry is to use computational approaches to model how different physicochemical factors affect axon diameter and spacing. This could enable more predictive models where a user can input their desired AA geometry, and the model would output the optimal fabrication conditions to achieve that geometry.

This thesis presented some preliminary attempts to image AAs using transmission electron microscopy, however future work can further probe whether there are regions of compact myelin. Our experiments showed that immunofluorescence microscopy involving sample permeabilization is *not* effective for identifying MBP+ regions of interest, since the detergents used in permeabilization degrade the integrity of the

myelin membrane. One promising approach is to use genetic reporters (e.g., a MBP green fluorescent protein reporter) cell line, where OPCs fluoresce upon expressing myelin basic protein. This approach would enable fluorescent detection of MBP without the requirement for permeabilization. With these reporter-based approaches, it is possible we might identify regions of compact myelin that were missed by our existing approaches.

In Chapter 3, we explored the role of myelin debris and microglia co-culture on myelin ensheathment by OPCs. The existing experiments focus on two-way interactions. Namely, when exogenous myelin debris is added to an OPC culture, wrapping index decreases in a dose-dependent manner. When myelin debris is added to a microglia culture (with no OPCs present), the microglia can phagocytose the debris. When microglia are added to an OPC culture (with no myelin debris present), wrapping index also changes in a dose-dependent manner. Future work can explore how all three factors interplay. For example, when all three components are added to AAs, do microglia phagocytose debris in a way that rescues myelin wrapping? Or does debris phagocytose polarize microglia to adopt an inflammatory phenotype that negatively impacts wrapping index? Although we attempted to conduct these experiments, limitations with sample availability meant that we had to use different batches of myelin debris. As a result, when we attempted the tripartite experiment, the batch of myelin debris failed to replicate the negative impact on wrapping index found across all other batches. Importantly, future work studying these three-way interactions should first set aside sufficient samples to revalidate and replicate the results found for individual two-way interactions. In addition, our current experiments used primary rat oligodendrocytes and human iPSC-derived microglia, since these two cell types were most readily available. This species mixing may have introduced additional complexity in our data (in particular because microglia are immune cells and may recognize distinct non-self antigens in rat oligodendrocytes). A future approach with this work is to use both hiPSC-derived oligodendrocytes and microglia from the same donor, to avoid any potential complexity with immune crosstalk due to the species mixing.

There are also several promising directions for experiments involving hiPSC-derived cells. First, future experiments can more precisely characterize the heterogeneity between different cell lines. For example, what are the relative efficacies of different pro-myelinating drugs across different cell lines, and are there any patterns based on the underlying mechanism of action of each drug? Furthermore, future work should more precisely characterize the distribution of cell types within the oligodendroglia are day 75. In our experiments, we seeded mixed oligodendroglia directly onto AAs, without any cell sorting to enrich for oligodendrocytes. This was based on previous results that magnetic activated cell sorting steps did not significantly enrich the purity of oligodendrocytes in these cell cultures. A more precise characterization of the relative proportions of astrocytes and neurons in these cultures is important for further disentangling mechanistic questions. One possible approach to improve oligodendrocyte purity is to include low amounts of ROCK inhibitor during the first 24 hours of oligodendrocyte culture, although this is yet to be carefully characterized. Another approach is to explore label-free approaches to cell separation, like inertial focusing, since Espinosa-Hoyos' prior work indicated that label-based sorting approaches (like magnetic and fluorescence-activated cell sorting) were ineffective at increasing oligodendrocyte purity. There have also been recent protocols (for example by García-León et al.) for deriving higher-purity oligodendrocytes from iPSCs that may be promising to explore, although such protocols often involve lentiviral transduction, which may limit translatability.

Finally, the experiments with ApoE3/4 iPSC-derived oligodendrocytes can be extended to further probe underlying disease mechanisms. For example, we hypothesize that because ApoE4 cells have deficient cholesterol efflux, these oligodendrocytes have higher basal levels of unsaturated sterols, and therefore drugs that elevate sterol levels (and improve myelination for ApoE3 oligodendrocytes) fail to improve myelination for ApoE4 cells. There are several ways to further validate this hypothesis by directly probing the underlying mechanism. One approach is to directly add unsaturated sterols to the cell culture (instead of drugs that indirectly act to change sterol concentration),

and explore whether exogenous sterols are beneficial for ApoE3 cells but detrimental for ApoE4 cells. Importantly, this work would require prior validation that sterol uptake is comparable across both cell lines. Furthermore, the hypothesis can be further validated by adding additional pharmacological compounds that directly affect sterol synthesis (but are not canonically associated with myelination). This would provide an orthogonal approach to explore whether sterol accumulation is indeed the causal factor. Most importantly, our experiments did not actually directly measure sterol concentration in ApoE3 vs. ApoE4 cells. Follow-up work can explore the use of mass spectrometry to directly quantify sterol concentration to verify that the drugs are indeed acting through this mechanism on the AA platform.

In summary, the work presented in this thesis addresses three key themes. First, we engineered an AA platform that achieved more biofidelic stiffness, diameter, and spacing of AAs relative to biological axons. Secondly, we validated the platform by replicating key *in vivo* correlative observations, such as the negative effect of exogenous myelin debris. Third, we used the AA platform as a tool for causative exploration. Having a deliberately reductionist model enables careful manipulation of one variable at a time (for example, a biophysical feature of the axons, a lesion component, the influence of a different cell type, or another mechanistic perturbation) to interrogate the underlying cellular and molecular mechanisms that drive myelination and disease.

Appendix A: Detailed protocols

A.1 Preparation of HsP resin

1. Weigh out each component below in an opaque container. The opaque container is necessary because Irgacure is UV-sensitive. Start with Sudan since the mass is the smallest. From Espinosa-Hoyos' thesis:

HDDA: starPEG ratio (% w/w all monomers)	HDDA (% w/w)	starPEG (% w/w)	Rhodamine 101 (% w/w)	Irgacure 819 (% w/w)	Sudan (% w/w)	DMSO (% w/w)	*E* (kPa)
3:1 (40)	30	10	0.005	2	0.1	57.895	140
1:1 (20)	10	10	0.005	2	0.1	77.895	0.4
1:3 (20)	5	15	0.005	2	0.1	77.895	0.2

   - All components are stored at room temperature except starPEG (20 kDa), which is stored at -20C.
2. Mix with a vortex for one minute.
3. Add to bead bath at 37C for 20 minutes.

A.2 Functionalization of 96-well plate

1. Prepare a solution of ethanol with 2% v/v 3-(trimethoxysilyl) propyl methacrylate (TMSPMA) and 1% v/v acetic acid.
2. Plasma treat the #0 glass-bottom well plate (Cellvis) in air plasma for 10 minutes.
3. To each well, add 100 µL of the solution and incubate at room temperature for 2 hours. Make sure the lids are on the 96-well plates since the solution is volatile.
4. Rinse each well 5 times in pure ethanol and leave to dry. Hold the well plate against the light to ensure that the bottom of each well is fully clear. If the washing process is insufficient, there will be a translucent crusty-looking residue at the bottom which will interfere with printing.

A.3 Fabrication of Artificial Axons using HR-3DP

For internal lab members, videos of this process can be found in the lab hard-drive Ming_Backup > Equipment Videos > HR3DP

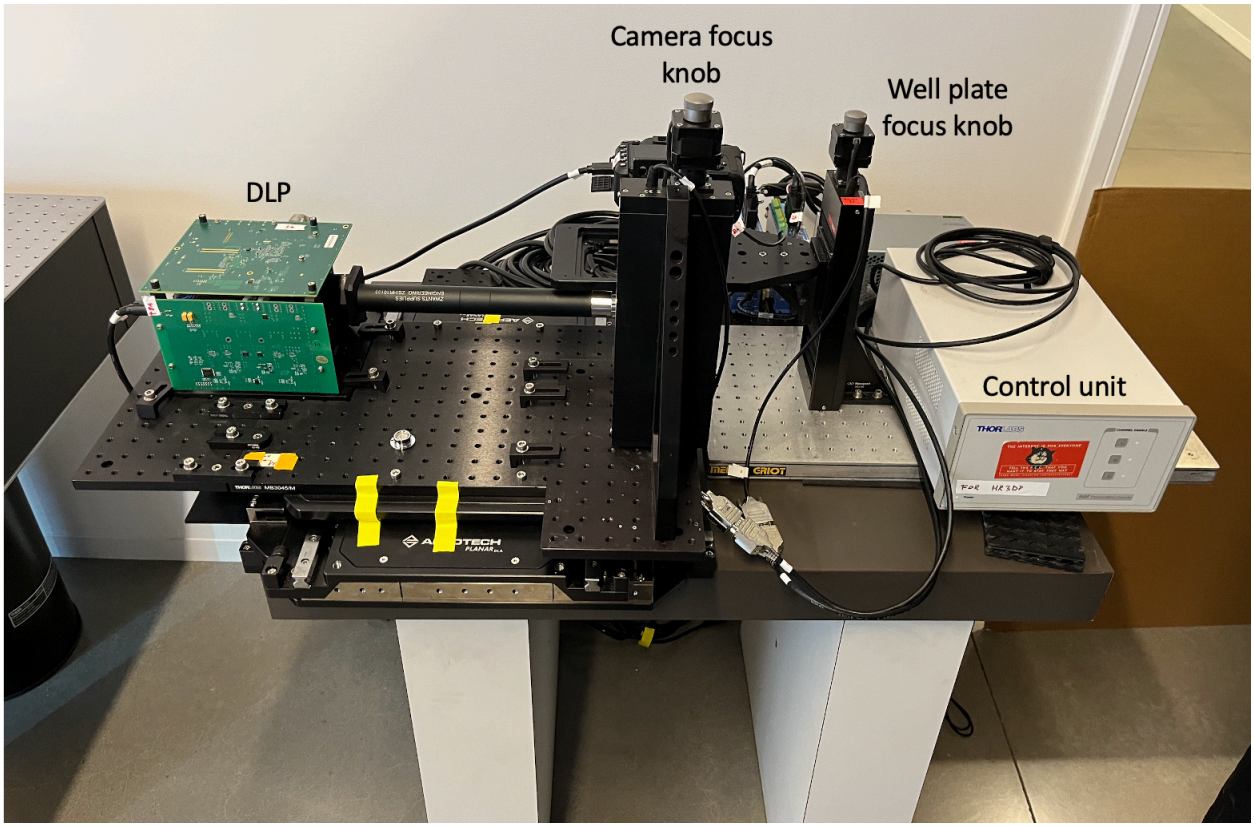

1. Remove the plastic dust cover.
2. Turn on fan to lowest setting; this cools the DLP (UV projector).
3. Open the laptop; it should be connected to the DLP and stage via USB, and to the camera via HDMI.
    a. The folder titled “MIT Operation” contains all necessary LabView files for printing
4. Turn on camera, then press LV button (live view) on the camera, then open the camera application on the laptop
    a. The image should be just black, since the camera’s default position is directly over the metal frame. You may need to click the ‘Switch view’

button (top right corner) to switch from the built-in laptop camera to the HR-3DP camera.

5. Turn on Thorlabs control unit by flipping switch (top right on the back), then turn all 3 channels on.
    a. Both the power light and all three channel lights should be on
6. Plug in DLP
7. Calibration and Focusing:
    a. Calibrating A1- Finding the coordinates of well A1, so the stage knows where the well plate is located.
        i. Ensemble Motion Composer is the program used to manually adjust the stage position.
        ii. After launching Ensemble Motion Composer, go to the section under “Jog” and click the [...] and set the speed to a lower value (<8).
        iii. Using the MIT Operations/Quick Operation/“Go to a selected well and display an image for focusing.vi” file. Under the ‘Well Selection’ tab, type in A1 (next to the green arrow) and select a full white image to project. Press the Run button (triangle on the top left).
        iv. Record the x and y coordinates of the center of well A1 under the ‘Plate Settings’ tab of the LabView program. To find the center coordinate of A1, you can use Ensemble Motion Composer to navigate to the edges of the well (e.g., go to the topmost and leftmost portion of the wells and record the x and y values respectively).
        v. You can double check your values by rerunning the program with the updated plate settings.
        vi. Save the settings by clicking “Edit” and clicking “Make current values default”.
    b. Focusing: This involves two steps: (1) focusing the camera so that the DLP projection is in the focal plane of the camera, (2) moving the well plate holder so that the bottom of the well plate is also in the same focal plane.

i. Go to MIT Operations/Quick Operation/“Go to a selected well and display an image for focusing.vi”
ii. In well selection, choose the file “focus image.bmp” to project.
iii. In the ‘Well Selection’ tab, enter the well you want to focus in. Make sure that under the “Plate Settings” tab, the correct A1 well coordinates are entered.
iv. Run the program by clicking the arrow in the top left.
v. With the image is displayed on the camera app, use the camera focus knob (see photo above) to change the focus until the projected axons are as clear (minimally blurry) as possible. This process moves the camera into the plane of focus of the DLP projection.
    - You can also change the shutter speed (brightness) on the camera to make focusing easier. I recommend minimizing the brightness during this initial focusing step.
    - You can also zoom in and out of the camera image using the + and – buttons on the camera.
vi. After focusing on dots, make a mark on the well plate with a sharpie or another marker. Dab the mark with an alcohol-moistened Kimwipe to create a rougher surface texture, giving more fine-grained features to focus on.
    - Use the well plate focus knob to move the *z*-position of the well plate holder, until the edges of the sharpie mark are clear. This brings the bottom of the well plate into the same focal plane as the projection.
    - I recommend increasing the camera brightness in this step to bring the mark into view.

8. Printing into each well. Open Mode_3_KK.vi in the ‘MIT Operations folder’.
a. Pipette 35 µL of resin into each well you plan to print in.
b. Under the ‘Plate Settings’ tab, input the x and y coordinates of well A1.

c. Well image settings files- For each well, make a CSV in the 'well settings' subfolder. I recommend copying and pasting an existing file and using that as a template to modify. This involves specifying which digital masks to print, the exposure time, exposure intensity, and exposure order.
d. Well config files- For each well, make a text file in the 'well config' subfolder. I recommend copying and pasting an existing file and using that as a template to modify. This involves setting the spacing between multiple projections within each well, and specifying the number of wells total. The default spacing is typically x = 1.5, y = 1.5.
e. In Mode_3_KK.vi, under the "Well Selection" tab, select all the wells you plan to print in. Remember that each well must have a corresponding file in both the well image and well config files.
    i. Select wells here by clicking on the well in the graphical user interface (in contrast to the previous LabView code used for focusing, where you typed in the well name).
f. Press the Run button (triangle in the top left) **AND** the text that says 'Run'.
    i. Note the contrast to before – in the previous LabView code used for focusing, you just pressed the triangle button to run the program. Here, you need to press both the triangle *and* the 'Run' text.
    ii. Conditions for printing axons:
        - 5 μm diameters, 30 μm spacing: intensity = 200, exposure time = 1.5s
        - To print smaller-diameter axons: reduce light intensity to 120 and keep exposure time at 1.5s. This will achieve a small patch of 2 μm axons, with an outer periphery of 1.5 μm axons.
        - Another approach to print smaller-diameter axons is to print a mask using 1 px axons separated by 50 px instead of 30 px. Use intensity = 200 and exposure time = 1.5s.

iii. Troubleshooting: Sometimes, if the stage fails to move after pressing 'Run', make sure to close any csv or txt files that are open. Sometimes, printing does not start if the well settings files being called are currently open.

A.4 Immunostaining for confocal microscopy.

1) Fix the cells in 4% paraformaldehyde for 10 minutes in a fume hood.
2) Wash three times in PBS to remove residual paraformaldehyde.
3) Prepare blocking solution: 5% v/v goat serum (store in -20C) in PBS
4) Prepare permeabilization solution: 0.1% Triton-X in goat blocking solution.
5) Permeabilize for ten minutes at room temperature.
6) Wash three times with PBS.
7) Block for 50 minutes at room temperature.
8) Add primary antibodies (also in blocking solution) and leave overnight in 4C.
9) Wash three times with PBS.
10) Add secondary antibodies (in PBS) leave at room temperature for an hour.
11) Wash three times in PBS.
12) During third wash, add DAPI to PBS and leave for 5 minutes.
13) Perform one final wash and leave cells in PBS.

A.5 Image analysis pipeline

These steps can be followed on any computer that runs Python 3.5.
If GetMyelinOnPillars does not run, uninstall and reinstall ImageJ.

1) Set up the correct directory structure. This is necessary so that the subsequent ImageJ analysis files can save the output data into the correct directory. Create a folder called DATA. Within this, create subfolders corresponding to each well (e.g., B1, B2, B3). Within each well folder, create a subfolder corresponding to each FOV (e.g., FOV1, FOV2, FOV3). Finally, within each FOV folder, create subfolders

labeled ‘OIR’, ‘TEMP’, ‘OBJECTS’, ‘MASKS’, and ‘DATA’. The following Python script can be used to create the necessary directory structure.

Image Analysis Making Directories.ipynb

Creates the required directory structure to be acted upon by the ImageJ scripts

```
import numpy as np
import pandas as pd
import matplotlib.pyplot as plt
import seaborn as sns
from itertools import groupby

sns.set(style="ticks",font="Myriad Pro",palette="Set1",font_scale=1.5)
%matplotlib inline

import time
import os
import shutil
import pickle as pkl

plate_folder_path = # fill in the directory of where the confocal images are saved
data_folder_path = # fill in the directory of where the analyzed images will go

# This code relies on there being 9 fields of view for every well

file_list = sorted(os.listdir(plate_folder_path))

counter = 0

if not os.path.exists(data_folder_path):
    os.makedirs(data_folder_path)
    for well in
['B2','B3','B4','B5','B6','B7','C2','C3','C4','C5','C6','C7','D2','D3','D4','D5','D6
','D7','E2','E3','E4','E5','E6','E7','F2','F3','F4','F5','F6','F7','G2','G3','G4','G
5','G6','G7']: # add or subtract wells
     for fov in ['FOV1','FOV2','FOV3','FOV4','FOV5','FOV6','FOV7','FOV8','FOV9']: #
add or subtract FOVs. This requires all wells to have 9 FOVs since the code will
automatically move OIR files from plate_folder_path to the corresponding subfolder
within data_folder_path

            if not os.path.exists(data_folder_path + '/'+ well + '/' + fov):
```

```
                os.makedirs(data_folder_path + '/'+ well + '/' + fov)
                os.makedirs(data_folder_path + '/'+ well + '/' + fov + '/OIR')

                shutil.move(plate_folder_path + '/' +
file_list[counter],data_folder_path + '/'+ well + '/' + fov + '/OIR/' +
file_list[counter])

                os.makedirs(data_folder_path + '/'+ well + '/' + fov + '/TEMP')
                os.makedirs(data_folder_path + '/'+ well + '/' + fov + '/OBJECTS')
                os.makedirs(data_folder_path + '/'+ well + '/' + fov + '/MASKS')
                os.makedirs(data_folder_path + '/'+ well + '/' + fov + '/DATA')
                counter = counter + 1
```

2) Run the ImageJ macro 'GetOverlapMasks.ijm'. This will iterate through each well and FOV in the DATA folder and create a myelin, axon, and overlap mask for each microscopy image. These masks will populate the MASKS subfolder.

GetOverlapMasks.ijm

```
//This macro runs Fiji to obtain overlap masks of AA pillars with myelin//

//path= # Fill in the file path to the DATA folder. Make sure to begin the filepath
with a / character.
//get names if all "DATA" directories (no other files)
list=newArray(0);
list1=newArray(0);
list2=newArray(0);

listall=getFileList(path);
for(i=0;i<listall.length;i++){
if(endsWith(listall[i],"/")){
        list=Array.concat(list,listall[i]);
        }
}

for(i=0;i<list.length;i++){
       print(list[i]);
```

```
}

//zlist=File.openAsString(path+"list-z");
//zlistarray=split(zlist, "\n");
//setBatchMode(true);

for(i=0;i<list.length;i++){
//for(i=13;i<14;i++){

//get wells
well = path+list[i];

//get fields
list1 = getFileList(well);
for(j=0;j<list1.length;j++){
       print(list1[j]);
}
//zstart = zlistarray[i];
for(j=0;j<list1.length;j++){
zstart = 1; //zstack beginning slice
zend = 10; //zstack ending slice
//print(zstart);
field = well+list1[j];
print(field);

//set directories
diroir = field+"OIR/";
dirtemp = field+"TEMP/";
dirmasks = field+"MASKS/";
dirdata = field+"DATA/";
//print(diroir);

// get zstack file name
list2 = getFileList(diroir);
file = list2[0];
filepath = diroir+file;
print(file);

//read zstack oir/oib file
run("Bio-Formats Importer", "open=filepath color_mode=Default rois_import=[ROI
manager] specify_range split_channels view=Hyperstack stack_order=XYCZT c_begin=1
c_end=3 c_step=1 z_begin=zstart z_end=zend z_step=1");
//print("HERE");
```

```
//nuclei channel
selectWindow(file+" - C=0");
saveAs("Tiff", dirtemp+"nuclei.tif");
run("Z Project...", "projection=[Max Intensity]");
setAutoThreshold("Default dark");
//setThreshold(800, 65535);
run("Convert to Mask", "method=Default background=Default black");
run("Watershed", "stack");
saveAs("Tiff", dirtemp+"mask-nuclei.tif");
saveAs("Tiff", dirmasks+"mask-nuclei.tif");

//count nuclei
run("Set Scale...", "distance=0 known=0 unit=pixel");
run("Set Measurements...", "  redirect=None decimal=2");
run("Analyze Particles...", "size=10-Infinity circularity=0.50-1.00 show=Nothing
summarize");
if (isOpen("Summary")) {
       selectWindow("Summary");
       saveAs("Results", dirdata+"nuclei.out");
       run("Close");
}


//red channel - pillars
selectWindow(file+" - C=1");
saveAs("Tiff", dirtemp+"pillars.tif");
run("Bandpass Filter...", "filter_large=40 filter_small=3 suppress=None tolerance=5
process");
setAutoThreshold("Default dark");
//run("Threshold...");
setOption("BlackBackground", true);
run("Convert to Mask", "method=Default background=Default calculate black");
//run("Watershed", "stack");

saveAs("Tiff", dirtemp+"mask-pillars.tif");
saveAs("Tiff", dirmasks+"mask-pillars.tif");
run("Duplicate...", "title=mask-pillar-1.tif duplicate");
run("Dilate", "stack");
run("Watershed", "stack");
run("Outline", "stack");
saveAs("Tiff", dirtemp+"mask-pillars-rim.tif");
saveAs("Tiff", dirmasks+"mask-pillars-rim.tif");
```

```
//green channel - myelin threshold "thresh"
thresh = 200;
selectWindow(file+" - C=2");
saveAs("Tiff", dirtemp+"myelin.tif");
setThreshold(thresh, 65535);
run("Convert to Mask", "method=Default background=Default black");
saveAs("Tiff", dirtemp+"mask-myelin-"+thresh+".tif");
saveAs("Tiff", dirmasks+"mask-myelin-"+thresh+".tif");

////clean salt-pepper noise in myelin channel if needed
//selectWindow("mask-myelin-"+thresh+".tif");
//run("Median...", "radius=0.5 stack");
//saveAs("Tiff", dirtemp+"mask-myelin-"+thresh+"-clean.tif");
//saveAs("Tiff", dirmasks+"mask-myelin-"+thresh+"-clean.tif");



//get Z-projection 2D myelin area and intensity (no myelin debris subtraction)
open(dirtemp+"myelin.tif");
selectWindow("myelin.tif");
run("Z Project...", "projection=[Max Intensity]");
setThreshold(thresh, 65535);
run("Set Scale...", "distance=0 known=0 unit=pixel");
run("Set Measurements...", "area mean integrated limit redirect=None decimal=2");
run("Measure");
//run("Analyze Particles...", "size=0-Infinity display clear summarize ");

if (isOpen("Results")) {
       selectWindow("Results");
       saveAs("Results", dirdata+"Total-MBP-2D-"+thresh+".out");
       run("Close");
}

run("Close All");

//overlap of pillar-rims and myelin
open(dirtemp+"mask-myelin-"+thresh+".tif");
open(dirtemp+"mask-pillars-rim.tif");
imageCalculator("Multiply create stack", "mask-pillars-rim.tif","mask-myelin-
"+thresh+".tif");
selectWindow("Result of mask-pillars-rim.tif");
saveAs("Tiff", dirmasks+"mask-myelin-overlap-"+thresh+".tif");
saveAs("Tiff", dirtemp+"mask-myelin-overlap-"+thresh+".tif");
```

```
run("Close All");

////overlap with cleanup
//open(dirtemp+"mask-myelin-"+thresh+"-clean.tif");
//open(dirtemp+"mask-pillars-rim.tif");
//imageCalculator("Multiply create stack", "mask-pillars-rim.tif","mask-myelin-
"+thresh+"-clean.tif");
//selectWindow("Result of mask-pillars-rim.tif");
//saveAs("Tiff", dirmasks+"mask-myelin-overlap-"+thresh+"-clean.tif");
//saveAs("Tiff", dirtemp+"mask-myelin-overlap-"+thresh+"-clean.tif");

run("Close All");
}
}
```

3) Run the ImageJ macro 'GetOverlapMasks.ijm'. This will compare all the mask files and identify which pixels of myelin corresponded to which AAs. The output is a text file that lists every pixel of myelin and is corresponding axon, which is then fed into a Python file (step 4) that quantifies the percentage wrapping of each axon.

GetMyelinOnPillars.ijm

```
//This macro runs Fiji 3D Manager to build 3D pillar objects from 2D pillar slices
and then overlaps each pillar with myelin.
//It generates V-Data.txt file with pixel by pixel information of the overlap

for(k=7;k<=7;k++) {

path= # Fill in the file path to the DATA folder. Make sure to begin the filepath
with a / character.

setBatchMode(true);
list=newArray(0);
listall=getFileList(path);
for(i=0;i<listall.length;i++){
if(endsWith(listall[i],"/")){
        list=Array.concat(list,listall[i]);
        }
}
```

```
for(i=0;i<list.length;i++){
//for(i=0;i<=8;i++){
dir = path+list[i];
print(list[i]);
dirmasks = dir+"MASKS/";
dirobjects = dir+"OBJECTS/";
dirdata = dir+"DATA/";
thresh = 200;

pillar = "mask-pillars-rim.tif";
myelin = "mask-myelin-overlap-"+thresh+".tif";
objects = "Objects"+thresh+".zip";
data = "Data-"+thresh+".txt";
pathpillar = dirmasks+pillar;
pathmyelin = dirmasks+myelin;
pathobjects = dirobjects+objects;
pathdata = dirdata+data;



open(pathpillar);
run("3D Manager");
Ext.Manager3D_Segment(128,255);

Ext.Manager3D_AddImage();
Ext.Manager3D_Save(pathobjects);

open(pathmyelin);
Ext.Manager3D_SelectAll();
Ext.Manager3D_List();
Ext.Manager3D_SaveResult("V", pathdata);
Ext.Manager3D_CloseResult("V");
Ext.Manager3D_Close();
run("Close All");

}
}
```

4) Run all the code cells in ‘Image Analysis ITERATE.ipynb’. This will analyze the text files from step 3, aggregating across all the z-stacks for a given axon to determine the percentage wrapped. This is also used to calculate the wrapping index.
    a. To conduct statistical tests, ca also import scipy as a package using `import scipy`

```
import numpy as np
import pandas as pd
import matplotlib.pyplot as plt
import seaborn as sns
from itertools import groupby

sns.set(style="ticks",font="Myriad Pro",palette="Set1",font_scale=1.5)
%matplotlib inline

import time
import os
import pickle as pkl


def fov_analysis(file_name):
    # Analyse myelin wrapping for a given field of view.

    # May need to replace 'Label' with 'Obj' based on whose code we're running

    raw_data = pd.read_csv(file_name, delimiter=r"\s+")

    #Create an empty list for the output
    pillar = []
    z_stack = []
    axon_pixels = []
    myelin_pixels = []
    fraction_wrapped = []
    category = [] #20, 50, 80, 100
    wrap80 = []



    df_to_group = raw_data[['Obj','Z','Value']]
    grouped_df =
df_to_group.groupby(['Obj','Z']).agg(return_wrapping_category).reset_index()
```

```
        # I spent one hour trying to find reset_index! Necessary for being able to
retrieve columns
    category = grouped_df['Value']
    pillar = grouped_df['Obj']
    z_stack = grouped_df['Z']

    grouped_df_2 = df_to_group.groupby(['Obj','Z']).agg(num_nonzeros).reset_index()
    myelin_pixels = grouped_df_2['Value'] # Total number of myelin pixels

    grouped_df_3 =
df_to_group.groupby(['Obj','Z']).agg(return_fraction_wrapped).reset_index()
    fraction_wrapped = grouped_df_3['Value'] # Total number of myelin pixels



    out1_data = {'pillar': pillar,'z_stack': z_stack,'myelin_pixels': myelin_pixels,
'fraction_wrapped': fraction_wrapped, 'category':category}

    out1_unfiltered = pd.DataFrame(out1_data) # contains every single pillarand z-
stack
    total_pillars = len(np.unique(out1_unfiltered['pillar'])) # RETURN: TOTAL NUMBER
OF PILLARS

    out1 = out1_unfiltered[out1_unfiltered.fraction_wrapped > 0] # contains only the
pillars that have non-zero wrapping

    wrap_any_pillars = len(np.unique(out1['pillar'])) # number of pillars with
myelin at all in any one z stack
    wrap_any_myelin = sum(out1['myelin_pixels']) # sum of all the myelin pixels in
all z stacks with wrapping

    # Filter out1 to contain only the pillars that are >50% wrapped
    out1_50 = out1[out1.category > 50] # out1 only with the pillars exceeding 50%
wrapping
    wrap_50_pillars = len(np.unique(out1_50['pillar'])) # number of pillars with 50%
wrapping in at least one z stack
    wrap_50_myelin = sum(out1_50['myelin_pixels']) # sum of all the myelin pixels in
all z stacks with >50% wrapping

    # Filter out1 to contain only the pillars that are >80% wrapped
    out1_80 = out1_50[out1_50.category > 80] # out1 only with the pillars exceeding
50% wrapping
    wrap_80_pillars = len(np.unique(out1_80['pillar'])) # number of pillars with 80%
wrapping in at least one z stack
```

```
    wrap_80_myelin = sum(out1_80['myelin_pixels']) # sum of all the myelin pixels in
all z stacks with >80% wrapping



    # Make an array of how many z-stacks in each pillar have >80% wrapping
(aggregating across all z stacks for one pillar)
    for pillar in np.unique(out1_80['pillar']):
        relevant_data = out1['category'] [out1['pillar'] == pillar] # array *
boolean
                    # array of the wrapping categories that are relevant
        wrap80.append(max([len(list(g[1])) for g in groupby(relevant_data) if
g[0]==100])) # ITAY'S CODE TO CHECK FOR LONGEST CONSECUTIVE REGION

    wrap80 = np.asarray(wrap80) # Turns wrap80 from a normal array to an np array,
allows for boolean comparisons

    # Determine the total number of pillars that have >80% in at least three z-
stacks
    wrap_80_three_stack = np.sum((wrap80>2))

    # Determine the total number of pillars that have >80% in at least five z-stacks
    wrap_80_five_stack = np.sum((wrap80>4))

    # Of the pillars that are >80% wrapped, determine the average length of myelin
wrapping in microns
    if np.sum(wrap80>0) == 0:
        average_full_wrapping_length = 0 # output>1 is to add up only the ones that
have >80% wrapping
    elif np.sum(wrap80>0) <= 1:
        average_full_wrapping_length = 1 # output>1 is to add up only the ones that
have >80% wrapping
    else:
        average_full_wrapping_length = 2*np.sum(wrap80)/np.sum(wrap80>0) # average
length in MICRONS (factor of 2)

  return total_pillars, wrap_any_pillars, wrap_50_pillars, wrap_80_pillars,
wrap_80_three_stack, wrap_80_five_stack, wrap_any_myelin, wrap_50_myelin,
wrap_80_myelin, average_full_wrapping_length



  ###

  def return_wrapping_category(x):
```

```
            current_fraction_wrapped = np.sum([x > 0])/len(x) # value of
fraction_wrapped of the slice

            if current_fraction_wrapped > 0.8:
                return 100
            elif current_fraction_wrapped > 0.5:
                return 80
            elif current_fraction_wrapped > 0.2:
                return 50
            else:
                return 20

    def num_nonzeros(x):
        return np.sum([x > 0])

    def return_fraction_wrapped(x):
        return np.sum([x > 0])/len(x)

    ###


    os.listdir(plate_folder_path)
    os.listdir(plate_folder_path)

    time_0 = time.time()

    plate_folder_path = # file path to the DATA folder containing all the wells and
FOVs
    export_file_name # file path of where the saved data should go

    total_pillars = []        # total number of pillars
    wrap_any_pillars = []     # total number of pillars with at least one pixel of
myelin around it
    wrap_50_pillars = []      # total number of pillars with at least one z stack that
is >50% wrapped
    wrap_80_pillars = []      # total number of pillars with at least one z stack that
is >80% wrapped
    wrap_80_three_stack = []  # total number of pillars with at least three z stack
that is >80% wrapped
    wrap_80_five_stack = []   # total number of pillars with at least five z stack
that is >80% wrapped
    wrap_any_myelin = []      # total area of myelin present
```

```
  wrap_50_myelin = []       # total area of myelin around all pillars that are >50%
wrapped
  wrap_80_myelin = []       # total area of myelin around all pillars that are >80%
wrapped
  average_full_wrapping_length = []   # of the pillars that contain full wrapping,
the average length of full wrapping (in microns)
  well_array = []
  fov_array = []

  z_projection = []
  total_nuclei = []

  # Iterate through all the wells
  for well in os.listdir(plate_folder_path):
      print(well)

      # Iterate through all the fields of view in each well

      for fov in os.listdir(plate_folder_path + '/' + well):
          print(fov)

  # Replace Data-500 with the appropriate threshold used in the ImageJ macro (e.g.
Data-1000 if the threshold was 10000)

          # Check that the three data files exist (txt file + nuclei + z-projection)
          if os.path.exists(plate_folder_path + '/' + well + '/' + fov +
'/DATA/V_Data-500.txt') and os.path.exists(plate_folder_path + '/' + well + '/' +
fov + '/DATA/Total-MBP-2D-500.out') and os.path.exists(plate_folder_path + '/' +
well + '/' + fov + '/DATA/nuclei.out'):

              # Load the relevant text file for a given fov
              file_path = plate_folder_path + '/' + well + '/' + fov +
'/DATA/V_Data-500.txt'

              # Call the fov_analysis function to analyse the fov
              out1, out2, out3, out4, out5, out6, out7, out8, out9, out10 =
fov_analysis(file_path)
              total_pillars.append(out1)
              wrap_any_pillars.append(out2)
              wrap_50_pillars.append(out3)
              wrap_80_pillars.append(out4)
              wrap_80_three_stack.append(out5)
              wrap_80_five_stack.append(out6)
```

```
                wrap_any_myelin.append(out7)
                wrap_50_myelin.append(out8)
                wrap_80_myelin.append(out9)
                average_full_wrapping_length.append(out10)
                well_array.append(well)
                fov_array.append(fov)

                z_projection.append(pd.read_csv(plate_folder_path + '/' + well + '/' +
fov + '/DATA/Total-MBP-2D-500.out', delimiter=r"\s+").iloc[0]['Area'])
                total_nuclei.append(pd.read_csv(plate_folder_path + '/' + well + '/' +
fov + '/DATA/nuclei.out', delimiter=r"\s+").iloc[0]['Count'])
                print(well + ' ' + fov)

  # Gather all the data into a dataframe
  processed_data = {'well': well_array,
                    'fov': fov_array,
                    'total_pillars': total_pillars,
                    'wrap_any_pillars': wrap_any_pillars,
                    'wrap_50_pillars': wrap_50_pillars,
                    'wrap_80_pillars': wrap_80_pillars,
                    'wrap_80_pillars_three_stack': wrap_80_three_stack,
                    'wrap_80_pillars_five_stack': wrap_80_five_stack,
                    'wrap_any_myelin': wrap_any_myelin,
                    'wrap_50_myelin': wrap_50_myelin,
                    'wrap_80_myelin': wrap_80_myelin,
                    'average_full_wrapping_length': average_full_wrapping_length,
                    'z_projection_area': z_projection,
                    'total_nuclei': total_nuclei}


  demo_df = pd.DataFrame(processed_data)

  print(time.time() - time_0)
  demo_df.to_csv(export_file_name)
```

A.6 Calibration and indentation with atomic force microscopy

For internal lab members, videos of this process can be found in the lab hard-drive Ming_Backup > Equipment Videos > AFM

1) Turn on the lamp, vibration isolation stage, and laser source.
2) Open Asylum Research app on the computer.
3) Open a pre-existing experiment template by clicking File -> Open Experiment -> USERS and choosing a prior experiment. You can open any experiment in my (Ming's) subfolder. These will simply open up the correct subset of windows/control toolbars, and I use the same in every experiment.
4) To calibrate the cantilever for InVOLS (n/V) and stiffness (N/m): Mount the cantilever and use tweezers to gently pull on the cantilever base to make sure it is secure.
    a. I use Cantilevers from NanoAndMore, specifically:
        i. Colloidal AFM probe, round tip, 0.1 N/m, 1.5 μm tip: part number CP-qp-CONT-PM-A-5
5) Place the cantilever onto the holder and place the holder onto the stage. Start by placing the front leg of the holder into the corresponding slot, then the back right leg, then the back left leg.
    a. Make sure that the legs of the holder are elongated before doing this; if the legs are too short, the cantilever may inadvertently make contact with the table surface which can lead to damage.
6) Click on the Video icon and select 'S video'. Use the live camera feed to focus the camera onto the cantilever (three focus knobs on the back of the cantilever holder which control mirrors on the stage, that in turn direct light into the camera). Make sure that the stage is clean so that you don't inadvertently focus on the dust.
7) Use the laser position knobs to adjust the position of the laser to maximize the 'Sum'.
8) Adjust the deflection to zero (akin to taring a scale) by turning the deflection knob next to the laser (this is clearer in the video).

9) Calibrate the AFM.
    a. Place a glass slide underneath the cantilever.
    b. Press the ‘Engage’ button in Asylum, which turns on the piezoelectric stack (will register a response when the cantilever hits the glass slide surface).
    c. Slowly lower the cantilever until the cantilever touches the surface (SUM will change when it does). Press ‘Retract’ to withdraw the cantilever.
    d. Under the Master Panel -> Force, set the Trigger channel to DefInVols. Set the Trigger Point to 1V.
    e. Press the ‘Continuous’ button on the Master Force Panel to perform many successive indentations of the sample.
    f. Under Toolbar, go to AFM Controls -> Master Force Panel -> Deflection. Select the relevant data.
    g. Shift-click ‘Fit’ to initiate a fit and then click ‘Fit’ again to fit a Gaussian to the histogram. Record the inverted spring constant in nm/V.
    h. In the Master Force Panel, copy the value into DefInvols.
10) Use the thermal noise approach to find the spring constant. The underlying principle is treating the system as a harmonic oscillator.
    a. Under the Master Panel, to the Thermal Tab and select ‘Capture Thermal Data’.
    b. After a few seconds, click ‘Stop Thermal Data’.
    c. Select ‘Initialize Fit’ and ‘Fit Thermal Data’ to obtain a spring constant in pN/nm.
    d. Enter the spring constant into the Master Panel.
    e. Click the Lock button. Now, the cantilever spring constant is fixed, and our next goal is to recalibrate the InVols in a PBS-immersed environment.
11) Pipette 100 uL of PBS onto the glass slide. This keeps the low-stiffness cantilever from bending back and fracturing when going through the air/water interface of your hydrated / liquid- immersed sample. Repeat step 9, this time with the cantilever indenting the glass slide within a submerged environment. In the

Master Force Panel, copy the new value into DefInvols. This is the value which will be used for subsequent AA indentation.

12) Place a coverslip containing AAs underneath the cantilever and repeat this same process to generate force-displacement curves for AAs.

AFM analysis script, adapted from Camille Farruggio

```
#Identify noise threshold for the force data and identify contact point

###write function to identify thresholding-relevant variables in one step

#The 'series' argument refers to the raw data (time series)

def analyze_slice(series,step_size,step_number):#counts steps from first point from
0
    min_index=step_size*(step_number)
    max_index=min_index+step_size
    #print(min_index,max_index)
    step=series[min_index:max_index]
    #print(step)
    upper_bound=step.max()
    lower_bound=step.min()
    max_change=upper_bound-lower_bound
    stdev=step.std()
    mean=step.mean()
    return upper_bound,lower_bound,max_change,stdev,mean

def characterize_noise(series,step_size,noise_end,time_size=0.0005):
    step_count=int(noise_end/step_size)#lossy conversion of manual guess at max
    #noise time to number of steps for characterizing noise. The larger the step,
    #the more likely it is to cut off time nearer contact.
    print("step count: ",step_count)
    for i in range(step_count):#set max/min values for step-size-dependent
descriptors
        upper,lower,change,dev,mean=analyze_slice(series,step_size,i)
        numdev=change/dev#how many standard deviations in the peak to peak value
        if (upper-mean)>(mean-lower):
```

```
            meandev=(upper-mean)/dev#max standard devs from the mean in this step
        else:
            meandev=(mean-lower)/dev
        if i==0:
            upper_lim=upper
            lower_lim=lower
            change_lim=change
            sdevs=[dev]
            means=[mean]
            numdevs=[numdev]
            meandevs=[meandev]
        elif i>0:
            if upper>upper_lim:
                upper_lim=upper
            if lower<lower_lim:
                lower_lim=lower
            if change>change_lim:
                change_lim=change
            sdevs.append(dev)
            means.append(mean)
            numdevs.append(numdev)
            meandevs.append(meandev)
    pdrift=(means[-1]-means[0])/(len(means)*step_size)#what's the drift per point?
    drift=(means[-1]-means[0])/(len(means)*step_size*time_size)#what's the drift per
second?
    vppsigma=sum(numdevs)/len(numdevs)#number of standard deviations between peaks
expected from noise signal.
    #Obtained by averaging actual peak to peak values relative to stdev in data. 6-8
sigma is common in random noise.
    devmean=max(meandevs)#max allowable standard deviations from the mean in noise
    return upper_lim,lower_lim,change_lim,devmean,vppsigma,drift,pdrift

###Write a function to find the contact point via various criteria
def
find_contact(series,step_size,noise_end,time_size,identifier='maxchange'):#identifie
s contact point using
    #3 methods: absolute thresholds, max change in a step, and standard deviations
from the mean
    contact_found=False
    current_step=int(noise_end/step_size)

upper_lim,lower_lim,change_lim,devmean,vppsigma,drift,pdrift=characterize_noise(seri
es,step_size,noise_end)
```

```
    while not contact_found:
        upper,lower,change,dev,mean=analyze_slice(series,step_size,current_step)
        current_step+=1
        if identifier=='maxchange':
            if change>change_lim:
                contact_point=int((step_size*current_step)+(step_size/2))#sets the
contact point in the middle of the current step. Will break down in accuracy for
very large step sizes
                contact_found=True
        elif identifier=='absthresh':
            if upper>upper_lim or lower<lower_lim:
                contact_point=int((step_size*current_step)+(step_size/2))#sets the
contact point in the middle of the current step. Will break down in accuracy for
very large step sizes
                contact_found=True
        elif identifier=='stdfrommean':
            meandev=(upper-mean)/dev#max standard devs from the mean in this step.
Only care about upwards deviation due to signal
            if meandev>devmean:
                contact_point=int((step_size*current_step)+(step_size/2))#sets the
contact point in the middle of the current step. Will break down in accuracy for
very large step sizes
                contact_found=True
            elif step_size*current_step>series.size:
                print("Maximum allowed standard deviations from mean:",devmean)
                devmean += -0.1
                print ("No contact point found, paramaters not strict enough. New
max allowed deviations from mean:",devmean)
                current_step=int(noise_end/step_size)#re-starts loop with new
devmean variable
    contact_time=contact_point*time_size
    contact_val=series[contact_point]
    return contact_point, contact_time, contact_val, drift, pdrift

##########################################################################
######  Define some fitting functions    ###################################


R1=0.75*10**(-6)#m (Radius of microcarrier)  ### MING TO CHANGE ###
# If the axon is much larger than the indenter, this could be infinity

def hertz_force(h,E1,dh,dP):#includes variables for origin offset (dh and dp)
```

```
    E2=2*10**9 # Pa (indenter stiffness) ### MING TO CHANGE ###
    v2=0.4 # (Poisson's ratio of indenter) ### MING TO CHANGE ###
    v1=0.5 # (Poisson's ratio of microcarrier (assume 0.5 for hydrogel))
    #R1=R1
    R2=7.5*10**(-6) # m (Radius of indenter) ### MING TO CHANGE ###
    exp=1.5
    E= (((1-(v1**2))/E1) + ((1-(v2**2))/E2))**(-1)
    R = (0 + (1/R2))**(-1)
    #R= ((1/R1) + (1/R2))**(-1)
    P=np.zeros(len(h))
    for i in np.where(h<dh):
        P[i]=dP
    for i in np.where(h>=dh):
        P[i]=((4/3)*E*(R**(0.5))*((h[i]-dh)**(exp)))+dP
    return(P)


#%%
#Load up data from saved, exported files as dicts of dataframes
path='Dropbox (MIT)/Documents/Academic/Lab/[Biofizz]/AFM-Analysis/raw_data' ### MING
TO CHANGE ###
directory = os.path.join('/Users/mingyu_yang/',path)
data={}
for experiment in os.listdir(path=directory):
    if experiment=='B':
        new_dir=os.path.join(directory,experiment)
    else:
        print('Skipped '+experiment)
        continue
    for condition in os.listdir(path=new_dir):
        if '.DS_Store' in condition:
            continue
        use_dir=os.path.join(new_dir,condition)
        label=experiment+" "+condition
        fdata={}
        for root,dirs,files in os.walk(use_dir):
            for file in files:
                if file.endswith(".csv"):
                    flabel=experiment+" "+condition+" "+file[:-4]
                    df=pd.read_csv(os.path.join(use_dir,file))
                    cols=df.columns.values
                    dat_df=pd.DataFrame()
                    #print(cols)
```

```
                    ###First extract the necessary data from the table
                    for col in cols:
                        if 'Force_Ext' in col:
                            if len(df[col].dropna())<10:
                                continue
                            else:
                                dat_df['ind_force (N)']=df[col].array#units are
Newtons
                        elif 'Ind_Ext' in col:
                            if len(df[col].dropna())<10:
                                continue
                            else:
                                dat_df['ind_depth (m)']=df[col].array#units are
meters
                        elif 'Force_Ret' in col:
                            if len(df[col].dropna())<10:
                                continue
                            else:
                                dat_df['ret_force (N)']=df[col].array#units are
Newtons
                        elif 'Ind_Ret' in col:
                            if len(df[col].dropna())<10:
                                continue
                            else:
                                dat_df['ret_depth (m)']=df[col].array#units are
meters
                        else:
                            print('missing')

#print(len(ind_force),len(ind_depth),len(ret_force),len(ret_depth))
                    fdata[flabel]=(dat_df) #a dict of keys which are individual
filenames which each point to the force and depth data for one indentation curve
whose data was stored as a CSV within that file
                    print(flabel)
        data[label]=fdata #a dict in which keys are the name of the experiment and
condition (i.e. sample dish descriptors) and point to a dict of keys which are
individual filenames which each point to the force and depth data for one
indentation curve taken within that dish
        print(label)

#%%
#define a function to round to a certain number of significant figures. This will
come in handy later.
```

```
def round_sig(x, sig=2):
    return round(x, sig-int(floor(log10(abs(x))))-1)

#%%
#define a function to take the area under a time-parameterized curve in the space
domain
def integ(y,x): #takes two series of data with data points evenly spaced in time
    ars=np.zeros(len(y)) #set up an array to hold areas for each point
    for i in range(len(ars)):
        if i==0:
            w=x[1]-x[0]
        elif i>0:
            w=((x[i+1]-x[i])/2)+((x[i]-x[i-1])/2)
        ar=y[i]*w
        ars[i]=ar
    return(np.sum(ars))
# Code below currently uses np.integrate.simps() instead, but this is here as a
simpler sanity check for the discrete integrals under the curve

#%%
df_all_E=pd.DataFrame(columns=['Carrier','Initial E','First Pass E','Second Pass
E'])
df_save_dir='/Users/mingyu_yang/Dropbox (MIT)/Documents/Academic/Lab/[Biofizz]/AFM-
Analysis/processed_data'+date

## If I get rid of R1, this can be removed
#diameters_sheet_loc=''
#diameters_df=pd.read_excel(diameters_sheet_loc,sheet_name=key,index_col=0)# accepts
an excel spreadsheet in which the first column is carrier names named according to
the same conventions as the spreadhseet files, and the second column is the
diameters in microns

data_list = []

for filename in data[key].keys():
    p_save_dir=df_save_dir+'/'+key
    if not os.path.isdir(p_save_dir):
        os.makedirs(p_save_dir)
    df=data[key][filename]
    carr_id=filename.split()[-1] ### NEED TO EDIT THIS BECAUSE CAMMIE GETS FILE ID
FROM THE FILE NAME
    print(carr_id)
    df_ind=df[['ind_depth (m)','ind_force (N)']]
```

```
    df_ret=df[['ret_depth (m)','ret_force (N)']]
    df_ind.dropna(inplace=True)
    df_ret.dropna(inplace=True)

    """ Note that the following code assumes that all dropped values were at
    the end and there were no gaps in the data such that the data remains an
    uninterrupted time series."""
    #ih,iF=df['ind_depth (m)'].to_numpy().astype(dtype=np.complex),df['ind_force
(N)'].to_numpy().astype(dtype=np.complex)
    ih,iF=df_ind['ind_depth (m)'].to_numpy(),df_ind['ind_force (N)'].to_numpy()
    rh,rF=df_ret['ret_depth (m)'].to_numpy(),df_ret['ret_force (N)'].to_numpy()

    #trim end noise from retraction data, which could cause issues later
    thousandth_ind=int(len(ih)/1000) #index of a point one tenth of the way through
the indentation data
    ihthousandth= ih[thousandth_ind]# indentation depth at one tenth the total
indentation time
    try:
        endind=np.where(rh<=ihthousandth)[0][0] #index of first point in time where
retraction depth is less than or equal to indentation depth at one tenth the total
indentation time
        print(endind)
        rh,rF=rh[0:endind],rF[0:endind]
    except IndexError:
        print('Retract not adjusted')
        rh,rF=rh,rF



    # do a first pass to remove egregious drift effects from data
    ## use analyze noise to analyze data at the very beginning of the curve
    ###set up step size and some other variables
    step_size=20#number of series points to include in a step
    time_size=0.0005#seconds per point in the data
    noise_end=500 #very safe guess at the final point at which contact definitely
hasn't occurred
    contact_point, contact_time, contact_val, drift,
pdrift=find_contact(iF,step_size,noise_end,time_size,identifier='maxchange')
    print ("length and zero: ",len(iF),contact_point)

    ## use pointwise drift rate to subtract a line from all included data
    if pdrift>0: #only adjust if upwards drift was found for now
        sub_arr=np.array(range(len(ih)))*pdrift #an array of values on the line to
be subtracted
```

```
        iF_older=iF
        iF=np.subtract(iF,sub_arr)
        sub_arr_r=np.flip(np.array(range(len(rh)))*pdrift)
        rF_older=rF
        rF=np.subtract(rF,sub_arr_r)

    try:

#popt,pcov=sp.optimize.curve_fit(hertz_force,ih,iF,p0=[100,0,contact_val,exp_ideal],
bounds=([-np.inf,min(ih),-np.inf,0.],[np.inf,max(ih),np.inf,5.]))
        popt,pcov=sp.optimize.curve_fit(hertz_force,ih,iF,p0=[1000,0,0])#,bounds=([-
np.inf,min(ih),-np.inf],[np.inf,max(ih),np.inf]))

    except RuntimeError:
        unfittable=False
        for E in range(1,10**6,10000):
            try:

#popt,pcov=sp.optimize.curve_fit(hertz_force,ih,iF,p0=[E,0,contact_val,exp_ideal],bo
unds=([-np.inf,min(ih),-np.inf,0.],[np.inf,max(ih),np.inf,5.]))

popt,pcov=sp.optimize.curve_fit(hertz_force,ih,iF,p0=[E,0,contact_val],bounds=([-
np.inf,min(ih),-np.inf],[np.inf,max(ih),np.inf]))
                continue
            except RuntimeError:
                if E>((10**6)-15000):
                    print(filename+ 'could not be fitted.')
                    unfittable=True
                    continue
                else:
                    continue
        if unfittable:
            continue

    print(popt)
    #print(pcov)
    h0=popt[1]
    P0=popt[2]
    E1=popt[0]
    #exp=popt[3]
    print("Contact point index: ",contact_point)
    print("E1: ",E1)
```

```
    data_list.append(E1)
    # calculate indentation parameters to determine hertzian behavior of indentation
curves
    iF_calc,ih_calc=iF-P0,ih-h0 #use fitted origin to re-center extension data
    rF_calc,rh_calc=rF-P0,rh-h0 #use fitted origin to re-center retraction data
    # also take portions of curves only during actual indentation of material for
calculation of plasticity factor
    try:
        iF_calc_pos,ih_calc_pos=iF_calc[(np.where(iF_calc<=0)[0][-
1]):],ih_calc[(np.where(iF_calc<=0)[0][-1]):]
    except IndexError: #occurs if there are no negative values so we just take the
whole thing
        iF_calc_pos,ih_calc_pos=iF_calc,ih_calc
    try:

rF_calc_pos,rh_calc_pos=rF_calc[0:(np.where(rF_calc<=0)[0][0])],rh_calc[0:(np.where(
rF_calc<=0)[0][0])]
    except IndexError: #occurs if there are no negative values so we just take the
whole thing
        rF_calc_pos,rh_calc_pos=rF_calc,rh_calc

    A1=sp.integrate.simps(iF_calc_pos,ih_calc_pos) # area under extension curve
    A2=sp.integrate.simps(np.flip(rF_calc_pos),np.flip(rh_calc_pos)) # area under
retraction curve
    phi=(A1-A2)/A1 # calculate the plasticity factor using areas under the extension
and retraction curves
    Fmax=max(rF_calc) # maximum force on extension curve
    Fad=min(rF_calc) # minimum force on retraction curve
    Fr=Fmax/abs(Fad) #calculate the force ratio using the ratio of the maximum force
and the force of adhesion

    if phi>0.2:
        print('A1 = ',A1)
        print('A2 = ',A2)
        print(phi,filename+' better modeled using Oliver Pharr')
        continue
    if Fr<=10:
        print(filename+' better modeled by JKR (compliant material) or DMT
(stiffness of material similar to probe stiffness)')
        continue

    plt.plot(ih_calc,iF_calc,label=filename+' E1='+str(round_sig(E1/1000,4))+'kPa')
```

```
plt.title(key+' Hertzian curves')
plt.legend(bbox_to_anchor=(1.05, 1),loc='upper left', borderaxespad=0.)
plt.savefig(p_save_dir+'/Extension curves'+'.png',bbox_inches='tight')
plt.show()
```

A.7 Differentiation of human oligodendroglia from induced pluripotent stem cells

50659, 51121, 51104 refer to the names of different iPSC lines.
All were obtained from Fossati/NYSCF under agreement and lab safety protocols.
All media recipes can be found in Douvaras and Fossati, 2015 (Chapter 1, citations 61 and 62)

Pre-Day 0: Before passaging for differentiation

0) Reconstitute Matrigel.

- Before: Pre-chill sterile pipette tips and well plates in the -20C fridge. Prepare ice bucket.
- Mix Matrigel aliquot with 25 mL DMEM. (Already pre-aliquoted so that each goes with 25 mL DMEM)

★ **Everything should be done inside the ice bucket. Matrigel should be kept totally cold.**

- Add **1 mL of Matrigel** solution to each well. Swirl plate each time.
- Change pipette tips after every few wells so that there isn't any inadvertent gelling in the tip.
- Incubate in 37C, for 1.5-2 hours.
- **Yield:** Usually each cryovial only gets you a couple of wells (typically just 1, sometimes 2)

1) Partially thaw a frozen cryovial containing hiPSCs by holding at 37 C water bath for 1-2 minute.

★ **The cryoprotectants are cytotoxic at room temperature. Must only partially thaw until a pellet remains.**

2) Add 1 mL DMEM to each partially thawed cryovial. Then transfer the contents into a 15 mL tube.

★ **Don't agitate the iPSCs too much. They like to be clumped. Unclumping -> loss of viability down the line.**

- Add DMEM to the tube until it reaches a total volume of 10 mL. This is to dilute the cryopreservative.

3) Add DMEM to the 15 mL tube to a total volume of 10 mL

- As before, the point is to dilute the cryopreservative.
- Alternative is to pre-fill each tube with 7-8 mL of DMEM and then add the cell suspension

4) Centrifuge for 5 min at 24 C and 800 rpm.

- Most protocols in the lab will use these centrifuge settings.
- Preparation for next step: Prepare solution of StemFlex and ROCK inhibitor. 1 mL media = 1 uL ROCK inhibitor
- Preparation for next step: Get ready for cell counting.

★ **Media must always be pre-warmed in every step. NEVER add cold media.**

5) Remove supernatant and resuspend the cell pellet in 1 mL of StemFlex containing 10 uM ROCK inhibitor

- Aspirate: Use the p200 (more delicate than p1000) to remove as much of the supernatant as possible, leaving just the clump of cells.
- Suspend cells in 1 mL of StemFlex + ROCK inhibitor. Then, take a 10 uL sample and prepare for cell counting ->
- Calculate how much cell suspension + media must be required to plate at 300-400k cells/well. Only need half the media for now.

★ **Reason is because you will pre-load each well with 1 mL of media. We pre-load so the Matrigel doesn't dry out.**

6) Plate cells at 300-400k/well

- Aspirate out the Matrigel solution. Pre-load each well with 1 mL of media + Rock inhibitor (ROCKi), stored in -20C. ROCKi is obtained from Stem Cell Technologies and is also often referred to as Y-27632.

- Deposit 1 mL of cell suspension + media into each well to make a total of 2 mL per well. Use a swirling motion.

★ **Must have an even distribution of cells across the plate.**

- After each well is seeded with cells, use a rocking motion to distribute.
- **Rocking motion**: Front-to-back and side-to-side gives even distribution. Rotating around would accumulate cells in the center
- RockI is only used in the first 24 hours after thawing/a new passage. Helps survival and maintains stem-like phenotype of iPSCs

7-9) Incubate the six-well plate in the 37 C. Change media everyday until ready to passage for differentiation.

★ **All days thereafter it is JUST StemFlex. No more ROCKi.**

10) When the cells reach 70-90% confluency, time to passage for differentiation.

★ **There should at least be one night without ROCKi before passaging.**

- Look at my folder 'Cell Training Round 2' to see examples that are ready vs. not ready.
- If not ready can lead to pretty serious consequences: detachment/poor differentiation, see 51104.

Pre-Day 0: After passaging

0) Reconstitute Matrigel.

- Need to prepare Matrigel. Remember that you also need control wells

★ **Even though the control wells are 10 times smaller, use 150 uL instead of 100 uL of Matrigel.**

- The goal for today is to passage 1 well for differentiation and then freeze the rest. Replenish the stock.

10-11) When the cells reach 70-90% confluency, add warmed Accutase and incubate for 5 minutes.

★ **There should at least be one night without ROCKi before passaging.**

★ **You usually only need to passage 1 or 2 wells for differentiation - one well can give 12. Remaining can freeze.**

- Aspirate each well then add 1 mL of pre-warmed Accutase.
- Accutase has a proteolytic effect: cleaves the cell-Matrigel interactions.
- Incubate for 5 minutes to allow the Accutase to take effect
- Hold the plate up to check if the bottom is clear. If not, put back in for a bit longer.

12-14) Dilute the Accutase solution by adding DMEM.

- For each line, prepare a 15 mL tube that contains 8 mL of DMEM (for dilution).
- Add 2 mL of DMEM into each well. Collect in a pipette and swirl around to wash a bit.

★ **Point is to dilute the Accutase in steps. First is the 2 mL DMEM. Then further dilute in the test tube.**

- Collect the 2 mL of each well into the 15 mL test tube. (Since only 1/2 wells, all go into one tube)
- Add 1 more mL of DMEM into each well to give it one final wash. The idea is to collect everything else at the bottom.

★ **Instead of adding Accutase down the sides (like media change), add directly to the center in a swirling fashion.**

★ **Adding a cell suspension to a test tube: Make sure it dribbles slowly down the sides.**

15) Centrifuge for 4 minutes at 24 C at 800 rpm.

★ **Never let the cell supply run out. Whatever iPSCs you take out, aim to freeze at this point to replenish.**

FOR PASSAGING:

16) Suspend the cells in 1 mL of StemFlex + ROCK Inhibitor

- Whilst the cells are spinning, prepare the appropriate quantity of StemFlex + ROCK inhibitor that you will need later.
- When cells are done, use a P200 pipette tip to aspirate out as much of the media as possible, leaving just the cell pellet.
- Resuspend pellet in 1 mL of StemFlex + ROCK inhibitor. Now count the number of cells in this pellet (next page)

17) Plate the cells in a Matrigel-coated plate.

- Aspirate out the Matrigel. Add 1 mL of StemFlex + ROCK inhibitor to each well.
- Top up the remaining 1 mL with the cell suspension prepared during cell counting.

★ **Experience is to plate all lines at 100k/well, EXCEPT 50659 and 51104 which we plate at 80k/well**

FOR FREEZING:

16) Suspend the cells in 1 mL of cold Synthafreeze

- Use a P200 pipette tip to aspirate as much of the media as possible, leaving just the cell pellet.
- Add 1 mL of **cold** Synthafreeze to the pellet. Gently pipette to mix and place in a cryovial.
- Place cryovial in Mr Frosty and set Mr Frosty in the -80C fridge.

★ **Mr Frosty should have been stored at room temp / 4C. Don't take a Mr Frosty directly from the -80 - too much shock**

★ **Periodically check Mr Frosty to make sure that the IPA level is kept above the line.**

AFTER PASSAGING:

18-19) Incubate the cells and perform media change every day.

- Like before, media change with StemFlex. No more ROCK inhibitor.

20) After hiPSC colonies reach 100-250 um in diameter, replace with neural induction medium.

- It's very important not to overshoot this. If the colonies start mixing into one another, grow out and passage again.

Days 0-8: Neural induction medium

21) After hiPSC colonies reach 100-250 um in diameter, replace with neural induction medium.

- The day this threshold is reached is **day 0** of the differentiation protocol. For the next few days, neural induction medium
- Main component of neural induction media is **mTeSR custom**
    - Comes as pre-measured media + supplement. Mix the entire bottles and add Pen-Strep. Concentration 1x desired. Add 5 mL
- The mTeSR custom can be stored in the -20 for 6 months. Every day, add RA, SB and LDN fresh.
    - RA and LDN are diluted 1000 fold, and SB is diluted 2000 fold. E.g. 12 mL media = 12 uL RA and LDN, 6 uL SB

★ **When you first prepare mTeSR custom and aliquot, aliquot into 40 mL quantities because the water expands**

^ This is generally true for all aliquoting that has to be done

22) Incubate and perform daily media change with neural induction medium until day 8

- After day 0 is decided, everything else from here on follows a stringent schedule.

Days 8-12: N2 medium

23) On day 8, switch to N2 medium

- All the media from here on start with **basal media**
    - With the exception of Pen Strep, everything you need for basal media is in the small 4C fridge.
- Make basal media. Then, add N2 to the basal media to turn it into **N2 media**
- Every day, change N2 media and add RA and SAG freshly on the day of use.
- Both RA and SAG are diluted 1000-fold.

Day 12: Mechanical dissociation

24) Detach the adherent cells.

- All the cells by now should be fully confluent. Phase contrast microscopy should see 3D structures.
- We will detach all the cells from their current plates and resuspend them into low-attachment plates.
- First, prepare N2B27 medium. Basal medium with N2 and B27 and insulin
- **Yield:** Each well is divided into two low-attachment wells

Steps for mechanical dissociation

- Prepare N2B27 medium **containing SAG and RA**.
- Prepare the low-attachment plates. Add 2 mL of N2B27 to each well. (**From now on**
- **we top up to 3 mL** - the third mL comes later)
- For the cells we are detaching: aspirate all the N2 media from the wells and replace with 1 mL N2B27.

- Use the scraper or roller to dissociate the cells from the bottom. Use a P1000 pipette to collect the suspension into a tube.
- Wash each well with another mL of N2B27 to collect the residuals that didn't pick up the first time. All 12 mL from one plate can go in one tube

★ **Technique for wash: Slant the plate down and dispense the media near the top so it trickles down and catches the cells with it**

- Now add this second mL into the same tube as before.

Cell scraper: 20 cuts in one direction, turn 90 degrees and make 20 more cuts, turn 90 degrees and make 20 more cuts

Try to avoid lifting the cell scraper out of the solution. Minimal agitation of the solution

Apply pressure and drag down. Afterwards, actually scrape the bottom (rotate the scraper) to detach any sticky bits.

Days 12-20: N2B27 medium

24) Change 2/3 of the media for the spheres once every other day.

THE VERY FIRST MEDIA CHANGE IS DIFFERENT

- Since there are still many small spheres that may not sink to the bottom, the first media change is different from the rest.
- Each cell is sitting in 3 mL of media. Every other day, we will change 2 mL of media with fresh N2B27 medium.
- For every three wells you are changing media for, prepare a 15 mL tubes.
  Using a 5 mL serological pipette, collect all the contents from the well into a tube.
- Rinse to pick up aggregates stuck to the bottom
  - Rinsing is the same ideas as before: tilt the plate down and dispense the media at the top, letting it slide down.

★ **For the first media change, centrifuge the suspension for 5 minutes at 800 rpm to help the small spheres sink to the bottom**

- Every day thereafter, there is no need for centrifugation. Just let the tubes sit for 3-5 minutes to let the spheres settle.
- Use the vacuum to aspirate out 2/3 of the media (i.e. 2 mL) and replenish with the same amount of N2B27 media.
- Gently pipette the suspension to break up any big clumps.

★ **Do not pipette TOO enthusiastically or the borders of the sphere will look blurry. Indicates that we are over-straining the cells.**

- Redistribute the cell suspension (pipetted first to distribute the aggregates evenly) back into the low-attachment plates.
    - The goal is to have a roughly equal number of aggregates in each well

Day 60: Dissociation and plating on AAs

1) Prepare

- Warm up DMEM, PDGF media, and accutase.

2) Dissociate cells from spheroid cultures.

- We are interested in the cells that have migrated out from the spheroids, not the spheroids themselves (full of dead cells)
- Aspirate **all** the medium using a serological pipette (carefully) and replace with 1 mL accutase.
- Incubate for 25-35 minutes. Takes longer. The entire sheet of cells should be floating. Some spheroids may still be stuck.
- Add 2 mL DMEM to each well and pipette 2-3 times to disperse spheres. Transfer 2 wells' contents into 15 mL tube.
- Dilute each well with DMEM and centrifuge at 800 RPM for 5 minutes.

3) Filter out large clumps/spheroids.

- Aspirate out the supernatant and resuspend each tube in 1 mL PDGF. Pipette 3-4 times.
  Prepare a 50 mL Falcon tube with a 75 um cell strainer. Rinse the strainer with 1 mL of
- PDGF to wet the membrane.
- Strain the cell suspension. Use a p1000 to transfer the cells from the 15 mL to the 50 mL
- Rinse the strainer with another 1 mL of PDGF to collect any remaining cells.
- Centrifuge the strained cells at 800 RPM for 5 minutes.

4) Count cells before sorting

- Aspirate out the supernatant and resuspend in 1 mL of PDGF.
- Count the suspended cells.
- Centrifuge at 800 RPM for 5 minutes.
- Plate at 80k cells/well.

A.8 Plan for experiment on tripartite interaction between microglia, debris and OPCs

- Obtain purified myelin debris from Li-Huei Tsai's laboratory. First, repeat the experiment described in Fig. 40 to verify the negative effect of the debris on oligodendrocytes.
- After replicating these results to verify the debris behaves as expected, test the following conditions:

Baseline conditions

1. OPC (20k)
2. OPC (20k) + microglia (10k)

Aim: Verify the dose-dependent negative effect of myelin debris on wrapping

1. OPC (20k) + debris (3 ug/mL)
2. OPC (20k) + debris (10 ug/mL)
3. OPC (20k) + debris (30 ug/mL)

Aim: Investigate whether the presence of microglia can rescue wrapping in the presence of debris

1. OPC (20k) + debris (3 ug/mL) + microglia (10k)
2. OPC (20k) + debris (10 ug/mL) + microglia (10k)
3. OPC (20k) + debris (30 ug/mL) + microglia (10k)

A.9 Plan for experiment on investigating cholesterol metabolism pathway

- Use Fossati et al. protocol to differentiate ApoE3 and ApoE4 iPSCs into oligodendrocytes.
- On day 75, plate oligodendroglia on AAs at a density of 80k cells/well.
- Test the following conditions, using 1 μM of each:
    - L-745870: EBP inhibitor that increases unsaturated sterols
    - Ro 48-8071: inhibits sterol synthesis
    - Zymosterol: the sterol itself
    - DMSO vehicle: control
- Hypothesis: Drugs that promote sterol accumulation (L-745870) AND supplying the sterol itself (zymosterol) should be beneficial for ApoE3 but not for ApoE4. Drugs that inhibit sterol accumulation (Ro 48-8071) should be beneficial to ApoE4 but not to ApoE3.

A.10 Sample preparation for TEM

1. Functionalize #0 glass coverslips using the same protocol as described in A.2.
    a. In the future, we recommend performing this experiment on chamber slides.
2. If using glass coverslips, use a hydrophobic wax pen to draw a square around the coverslip perimeter.
    a. If using chamber slides, there is no need to use the wax pen, since the chamber slide comes with removable walls.
3. Pipette resin onto the coverslip and print axons using the HR-3DP.
    a. A template well-settings file is found in the hard-drive Ming_Backup > TEM > well_settings_template.csv. This contains an example set of instructions for printing 8 distinct axon arrays with fiducial markers.
4. Gently submerge the coverslip in ethanol. If movements are too abrupt or fast, the turbulent ethanol flow can cause the pillars to topple over.
5. Leave coverslip in ethanol for 24 hours for the unreacted resin to dissolve away.
6. Gently dab vacuum grease onto each corner on the underside of the coverslip, then adhere the coverslip to the bottom of a plastic six-well plate.
7. Perform ten washes of the axons in ethanol. Do these very gently, as turbulent ethanol flow can lead to the axons toppling over.
8. Wash in five serial dilutions of PBS in ethanol. (e.g., 100% ethanol, 80% PBS and 20% ethanol, and so forth)
9. After the final wash, incubate in poly(ornithine) and laminin as described above.
10. Culture cells using the protocols described above for 2 weeks.
11. Obtain TEM fixative from core facilities. This will likely vary across TEM facilities and their fixation protocol.
    a. We obtained TEM fixative from the Koch Institute and followed their standard protocol for sample preparation.

Appendix B: Upskilling the cell therapy manufacturing workforce: design, implementation, and evaluation of a massive open online course

Mingyu Yang, Flora J. Keumurian, Caleb Neufeld, Elizabeth Skrip, John Duguid, Humberto Vega-Mercado, Reeta P. Rao, Marsha W. Rolle, Stacy L. Springs, Jacqueline M. Wolfrum, Paul W. Barone*, Krystyn J. Van Vliet*

This chapter is excerpted directly from an education research paper that was accepted for publication prior to the submission of this PhD thesis, in 'Advances in Physiology Education'. I am first author of that manuscript, and this article capturing my work in pedagogy and curriculum development during my PhD, as part of a larger educational project team-led by Van Vliet.

Introduction

Cell therapies have shown promise in treating and curing a range of diseases, including cancer[1], cartilage repair[2] and burns[3]. Unlike traditional small-molecule or protein therapeutics, cell therapies involve administering live cells into a patient. This approach leverages the broad biological functions and dynamic stimuli-responsiveness that cells uniquely exhibit but conventional protein therapeutics do not[4,5]. Despite the recent clinical successes of cell therapy products[6], very few formal training programs exist in the public domain for cell therapy manufacturing. Consequently, there exists an unmet need to develop a scalable course to support the growth of a well-trained workforce to manufacture these therapies[7]. To meet these needs, we developed a massive open online course (MOOC) hosted on the edX platform. In this paper, we summarize our experience in the collaborative design and implementation of the online course, as well as lessons learned based on student feedback.

The goals of the course were to teach the basic biology underpinning how cell therapies work, including the essential cell and systems physiology concepts, and to discuss the practical realities of how cell therapies are manufactured, industrialized, and regulated. The target audience of the course consisted of professionals in the biotechnology industry who were retraining to enter the cell therapy manufacturing workforce. These individuals have likely already received training in the manufacturing of protein drugs, such as monoclonal antibodies; therefore, we designed our course to emphasize the differences between these traditional biotherapeutics and cell therapy products. In particular, the cell therapy manufacturing workforce requires additional knowledge in cell biology, immunology, and a different set of analytical methods for process and product characterization. However, given the potential for MOOCs to reach a diverse, global audience[8], we also sought to make the course accessible to all learners, from college students to industry professionals with more limited biotechnology experience. In light of this, we did

not enforce any formal course prerequisites, although having a cell biology background was recommended.

The course development team consisted of researchers at two PhD-granting universities and individuals at three companies currently manufacturing cell therapy products. Our industry collaborators collectively represented roles from across the manufacturing pipeline, including research & development (R&D), technical operations, manufacturing science and technology, quality assurance, and regulatory affairs. This close collaboration with industry was central to the entire course development process, as one of our core teaching goals was to authentically immerse learners in the end-to-end manufacturing process. Examples of this collaboration include co-authoring all learning objectives with our industry partners and incorporating video interviews and on-site visits with each company. Furthermore, each section of the course was beta-tested (n = 66) and revised according to feedback from our industry collaborators and from first/second-year PhD students in various degree programs at MIT, to ensure the material was factually correct, authentic, and relevant for trainees and current working professionals.

Structure and content of the course

The course content is organized into six units, each covering a core pillar of cell therapy manufacturing. Each unit was designed to take one week, or approximately 7-10 hours of student effort, to complete. We ran the first iteration of the course as 'instructor-paced', where we released two units every two weeks. Learners were required to complete these two units before the next two were released. After receiving feedback from learners that this schedule was too inflexible (see 'Learner feedback' section), we changed the course to being 'self-paced', releasing all the material at course launch and allowing learners to work at their own pace. We also increased the course duration from six weeks to nine weeks in these subsequent offerings.

Unit 1 provided a brief historical context of cell therapy manufacturing and highlighted the similarities and differences between cell therapy manufacturing and protein manufacturing. Unit 2 provided the basic biological principles to understand how cell therapies work, including discussions of cell physiology, immunology, recombinant DNA techniques, and genome editing. The unit culminated in an overview of different types of cell therapy products currently being used for disease treatments, including chimeric antigen receptor (CAR)-T cells for oncology applications, and mesenchymal stromal/stem cells (MSCs) for myocardial infarctions. Unit 3 applied these fundamental biological principles to discuss the unit operations involved in producing the cell therapies, from cell acquisition through to administration of the final product to the patient. Unit 4 discussed quality control and how to assess critical quality attributes (CQAs) of the manufactured product. Topics included functional assays to characterize the therapeutic efficacy of the cell therapy, in addition to microbiological assays to check for contamination. Unit 5 showed how manufacturing

operations can be scaled-out or scaled-up to the industrial scale required to meet commercial demand. This unit also addressed pertinent business concepts such as cost of goods and supply chain management. Finally, Unit 6 explained how cell therapies are regulated to meet current good manufacturing practice (cGMP) standards, and the regulatory expectations for clinical approval.

When deciding the scope and depth of the course content, our guiding principle was to include only the practical knowledge that someone 'on-the-job' needed to know. Taking Unit 2 as a case study, we included an overview of metabolism that emphasized the nutrients and conditions required for cell culture, with comparatively less time dedicated to the details of biochemical pathway involved in cellular respiration. In contrast, some topics were more strongly emphasized; for instance, we dedicated a section to explain cell senescence and the consequences of high passage number during culture. The outline of content for all six units is provided in **Table 1** and **Table 2** shows the detailed learning objectives for each unit.

Table 1. Outline of course content

Unit		Course content
1	Overview of cell therapy manufacturing	History of cell therapies; Manufacturing cell therapies vs. protein therapeutics
2	Cell biology and immunology	Cell structure and organization; Nutrients and conditions for cell division; Stem cells; Cell-cell signaling; Immunology; Transfection and transduction; Targeted gene editing
3	Principles of cell therapy manufacturing	Acquisition and isolation of primary cells; Activation and genetic modification of cells; Expansion and cell culture; Harvest, formulation, and administration of cell therapies
4	Analytics for cell therapy manufacturing	Critical quality attributes; Characterization techniques in cell and molecular biology; Cell-based functional assays; Viral vector quality control assays; Microbiological and contamination assays
5	Industrialization of cell therapies	Scaling manufacturing to meet demand; Automation; Centralized vs. distributed manufacturing; Cost of goods; Supply chain management
6	Regulation of cell therapy manufacturing	Regulatory authorities; Regulatory expectations for approval pathways; cGMP requirements; Product safety and effectiveness; Process validation

Table 2. Detailed learning objectives for each unit

Unit		Learning objectives
1	Overview of cell therapy manufacturing	• Define what constitutes a cell therapy. • Outline the history of cells as therapies, including blood transfusions, autologous chondrocytes, epidermal autographs, xenotransplantation, *in vitro* fertilization, and chimeric antigen receptor-T cells (CAR-T). • Compare key product and manufacturing differences between recombinant proteins and cell therapies. • Analyze why the differences in recombinant protein manufacturing and cell therapy manufacturing exist and how they relate to final product quality. • Differentiate between autologous, allogeneic, and xenogeneic cell therapies.
2	Cell biology and immunology	• List the key attributes of the cell secretome and its impact on cell biology. • Differentiate paracrine signaling from direct repair. • Describe the steps of the cell cycle. • Identify important nutrients and conditions required to support cell division. • Differentiate between primary cells and immortal cell lines. • Define senescence and identify how it can affect important cell characteristics. • Describe the common techniques used for genetic engineering of cells, including transfection, viral transduction, and CRISPR-Cas9. • Explain if and how common viral vectors integrate DNA into host cells, and the key attributes of viral vectors for stable versus transient transduction. • Categorize the cells that make up the immune system and their function in the body's immune response to a foreign entity. • Identify the key characteristics of stem cells and how they can be used as therapeutics. • Describe how chondrocytes, keratinocytes, islet cells, xenogeneic cells, and immune cells can be used as therapeutics. • Appraise disease indications for their ability to be treated with cell therapies.

3	Principles of cell therapy manufacturing	• Define the concept of aseptic processing and list the key characteristics of good aseptic technique. • List the basic functions of a biosafety cabinet, incubator, and centrifuge. • Compare and contrast closed vs. open manufacturing operations, and list key controls that should be in place during open operations. • List the differences between attachment and suspension cell culture, and the impact of those differences on unit operation design. • Describe how the key concepts covered in Unit 2 drive decisions with regards to cell culture. • For the unit operations involved in cell therapy manufacturing (isolation, gene modification, expansion, cell culture, harvest, isolation, formulation, and cryopreservation), list the steps involved, and identify key attributes and parameters and their impact on downstream unit operations and patient experience. • Give an example of how a manufacturer would ensure quality control of cell thaw and administration at the clinical site. • Analyze differences in how autologous and allogeneic cell therapies are manufactured. • Define a batch record and describe what data are included in a batch record. • Describe and list the key steps of process verification, including when and how process samples are taken.
4	Analytics for cell therapy manufacturing	• Describe the key critical quality attributes (CQAs) for cell therapy products. • Identify key attributes used to confirm potency, purity, and safety of the final product. • Describe how steps in the manufacturing process can impact the potency, purity, and safety of the final product. • Describe how polymerase chain reaction (PCR) and flow cytometry work, and the cell therapy CQAs they can help to assess. • Describe how cell-based assays, such as secretory-assays, cell-based functional assays and replication competent vector assays, can be used to assess cell therapy CQAs. • Analyze the strengths and weaknesses of cell-based assays for assessing CQAs. • Describe how growth-based assays are used to test for the presence of microbial contamination in recombinant protein manufacturing, and why such assays are *not* ideal for use in cell therapy manufacturing. • Identify technologies that can be used to rapidly assess the sterility of cell therapy products.

		• Describe tests or endotoxin, including the limulus amebocyte lysate (LAL) gel clotting assay, kinetic assay, and rapid endotoxin essays.
5	Industrialization of cell therapies	• Summarize how automation is used in cell therapy manufacturing and the key drivers for its adoption. • Evaluate how control systems used in manufacturing drive final product quality. • Compare supply chain complexity for allogeneic and autologous cell therapy products, from donor to patient. • Identify the key considerations for quality and safety of a cell therapy product, and how they influence cell therapy industrialization. • Perform a simple cost of goods (CoGs) calculation and compare how key manufacturing decisions impact final CoGs. • List the steps required to release the final cell therapy product and the duration of each step. • Identify the key metrics for lot release. • Identify key considerations for final product distribution and administration, including shipping criteria and restriction time. • Compare centralized vs. distributed manufacturing to produce cell therapies and analyze key tradeoffs between the two approaches.
6	Regulation of cell therapy manufacturing	• Outline the history behind modern drug product regulations, identifying key themes that drive regulatory decision making. • Differentiate between the regulatory frameworks of protein therapeutics and cell therapies. • Define current good manufacturing practices (cGMPs), critical process parameter (CPP), process performance qualification (PPQ), and continued process verification (CPV). • Differentiate between cGMP requirements for protein therapeutics and cell therapies. • Evaluate whether a specific critical process parameter meets the definition. • List the components of manufacturing process validation and analytical method validation. • List components of a comparability study, and identify key differences in demonstrating comparability of protein therapeutics vs. cell therapies. • Give an example of a cell therapy manufacturing issue and its potential impact on process validation, method validation, and comparability studies. • Compare regulatory expectations across countries (e.g., US FDA, EMA, Japan, Singapore).

Types of instructional resources

We used a wide range of instructional modalities to teach the course material, shown in **Fig. 1**. Approximately 60% of the core material was delivered through text with embedded figures. Almost all the figures used in the course were created by the team's scientific illustrator, which gave the course its own visual identity and ensured that we were not reliant on license agreements for sourcing content. The remaining 40% of the core material was delivered through short (5-10 minute) instructional videos. These videos included lectures (professor standing in front of animated slides), 'Equipment in Action' videos (site visits to current cell therapy manufacturing facilities), and 'Meet the Expert' videos (interviews with current professionals about a day-in-their-life, their journey into the cell therapy manufacturing industry, and career advice to prospective hires). For accessibility, we added closed-captioning to all videos and wrote alt-text and figure captions for all static illustrations.

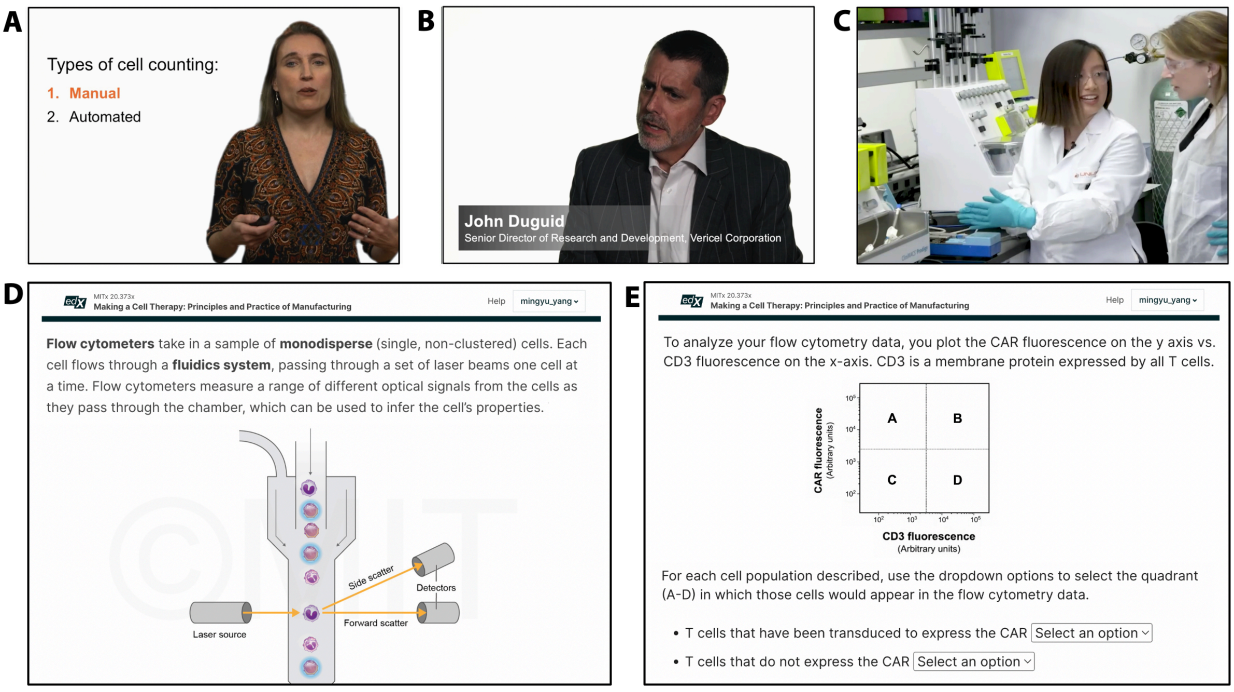

Figure 1. Examples of instructional modalities, including (A) lectures with the professor, (B) interviews with industry professionals, (C) videos of equipment in action, (D) text and embedded figures, (E) assessment questions.

To assess learning, we used a combination of formative and summative assessments. Multiple times within each unit, learners completed skill drills, which were low-stakes formative assessment problems that assessed knowledge of the most recently covered material. These questions were usually at the 'Remember', 'Understand', and 'Apply' tiers of Bloom's taxonomy[9,10], and students received unlimited attempts to answer each question.

Therefore, the main goal of skill drills was for learners to self-evaluate their understanding. After Units 2, 4, and 6, learners completed a problem set, which was a larger summative assessment designed to integrate concepts from across the previous two units. Every assessment question in the skill drills and problem sets was aligned directly to one of the learning objectives in **Table 2**. The problem sets followed a narrative progression, wherein learners took on the role of a new hire at a cell therapy manufacturing company, participating in a rotation program across different departments. The problem set questions typically were at the 'Apply', 'Analyze', and 'Evaluate' tiers of Bloom's taxonomy, and asked the learner to apply existing knowledge to new examples. For example, problem set 2 dealt with the use of hematopoietic stem cells (HSCs) for treating sickle cell disease, a cell type and disease indication that was only minimally discussed earlier in the course. By encouraging learners to apply their existing knowledge to new examples, we hoped to elucidate common themes underlying the manufacturing of all cell therapies, not just the case studies we chose to highlight in the course. The skill drills and problem sets were weighted at 25% and 75% of the final grade respectively, and learners had to achieve >80% overall to pass the course and receive formal certification.

Learner demographics

As of September 2023, we have offered the course four times, with a course enrollment of 2825 (Spring 2021), 2575 (Fall 2021) 2462 (Spring 2022), and 3468 (Spring 2023). To understand our learner demographics and motivations for taking the course, we distributed an optional entrance survey, which consisted of standardized, validated questions common across all MOOC surveys at MIT (**Fig. 2**). The number of entrance survey respondents was 272 (Spring 2021), 633 (Fall 2021), 373 (Spring 2022), and 571 (Spring 2023). Since the entrance survey is optional (as is standard across edX-hosted MOOCs), the response rate was low (9.6% - 24.6%), and we cannot verify that the population of survey respondents is necessarily representative of the course learners as a whole. Here, we draw conclusions about the population of survey respondents. We aggregated responses across all four offerings since there were no significant differences in the response distributions between offerings.

Figure 2A shows the self-reported highest education level of respondents across the four course offerings. The majority of our respondents (86%) had graduated from college, with 32% having also obtained a master's degree and 20% having obtained a doctoral degree. We also asked learners to indicate what barriers to education this course helped them to overcome (**Fig. 2B**). Learners were allowed to select multiple answers. The most common barrier to education was scheduling, with 63% of respondents selecting "I could not make time for regular classes". The second-most common was financial, with 46% of respondents selecting "I could not easily afford it otherwise". Other less-common barriers were geography ("The nearest school is too far away") and confidence ("I would not feel confident in an in-

person class"). Finally, we asked learners about their general motivations for enrolling (**Fig. 2C**). Learners were presented seven potential sources of motivation and asked to indicate whether each was applicable to a great extent, to some extent, to a small extent, or not at all. The most common motivation for enrolling was "to learn or develop a skill", with 75% of respondents agreeing with this to a great extent. The next most common was "to advance my career", with 54% of respondents agreeing with this to a great extent. Collectively, these results speak to the high number of survey respondents who were taking the course while also holding full-time jobs, who sought out this online course as a more time-flexible path for professional development and career advancement.

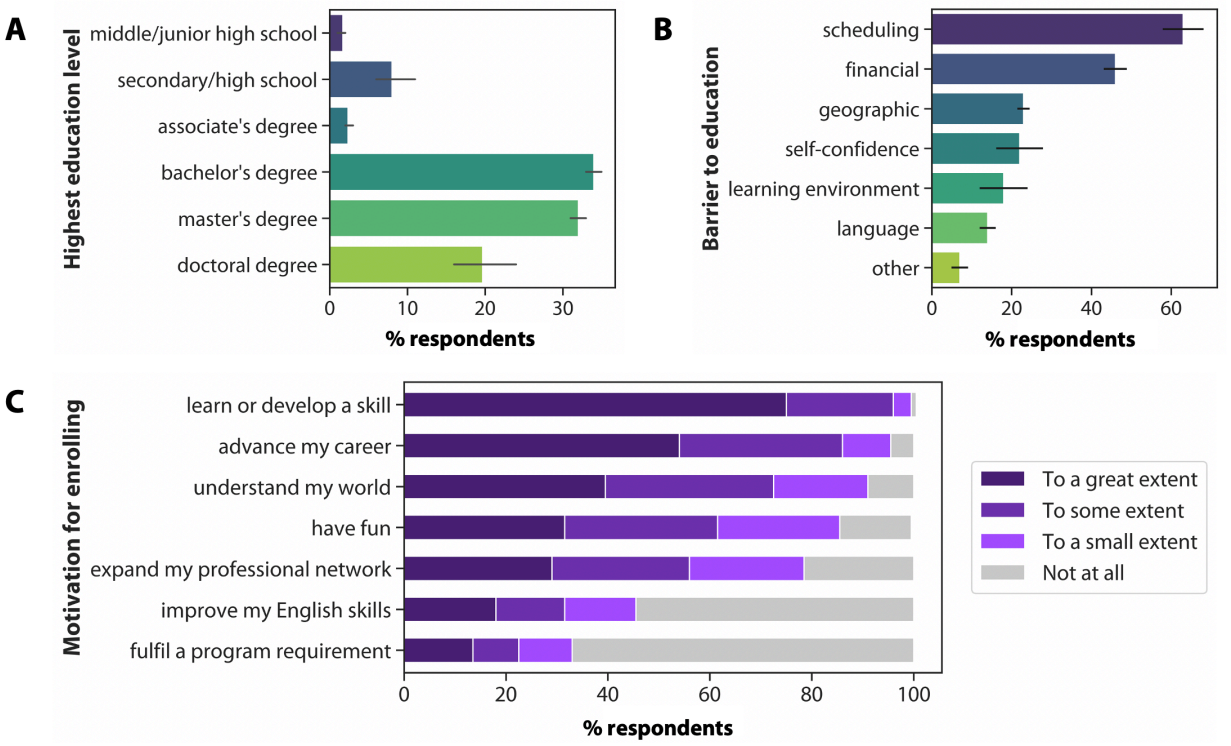

Figure 2. Summary of entrance survey results, including (A) highest education level of respondents, (B) barriers to education that taking this course helped learners to overcome, (C) learner motivations for enrolling in the course.

Learner feedback

At the end of each cycle of the course, we emailed an optional exit survey to collect feedback from all learners (**Fig. 3**). This included learners who simply registered and did not complete the course as well as those who did complete the course for either a passing or failing grade. Because we delivered this course through MIT on the edX platform, the exit survey tools and policies were required to be those available through MIT at the time. As a result, the exit survey tool was administered through an MIT platform that was not

integrated within edX, and addressed learner privacy by making the learner identity and learner status (passing vs. failing) anonymous. We thus could not establish correlations between the exit survey responses and course performance or duration of participation. We can speculate that the exit survey respondents were more likely to be those who completed the course.

Our process for evaluating the efficacy and impact of our course is similar to Kirkpatrick's four-level evaluation model, which focuses on four levels of program evaluation. Contextualized to our study, those four levels are learner satisfaction, knowledge gained, changes to learner behavior in their workplace context, and broader impact[11]. The number of exit survey respondents was 114 (Spring 2021), 186 (Fall 2021), 85 (Spring 2022), and 116 (Spring 2023). We asked learners Likert-scale questions including "Did the course meet your expectations?" and "How likely are you to recommend the course?", and learners indicated their answer on a five-point scale **(Fig. 3A)**. Across the four course offerings, on average 69% respondents indicated that the course either 'far exceeded' or 'exceeded' expectations. 91% of respondents indicated that they were either 'very likely' or 'likely' to recommend the course to someone else. We further disaggregated the responses based on course offering to identify whether changes made to the course structure (outlined below) influenced learner satisfaction. We performed a Kruskal-Wallis H-test and found no significant differences between offerings in both learner expectations ($p = 0.46$) and likelihood of recommending the course ($p = 0.50$). In addition, we asked learners to rank the helpfulness of the different course components on a Likert scale from 'very helpful' to 'very unhelpful' (**Fig. 3B**). All course components were generally evaluated favorably, with more than 60% of respondents rating each component as 'very helpful' or 'helpful'. Both of the primary modes of content delivery (text & figures, lectures with the professor) were highly rated with >90% respondents rating them as 'very helpful' or 'helpful'. The course component that respondents found least useful was the discussion forum, with 16% of respondents indicating this was 'unhelpful' or 'very unhelpful', and 15% of respondents not using the forum at all.

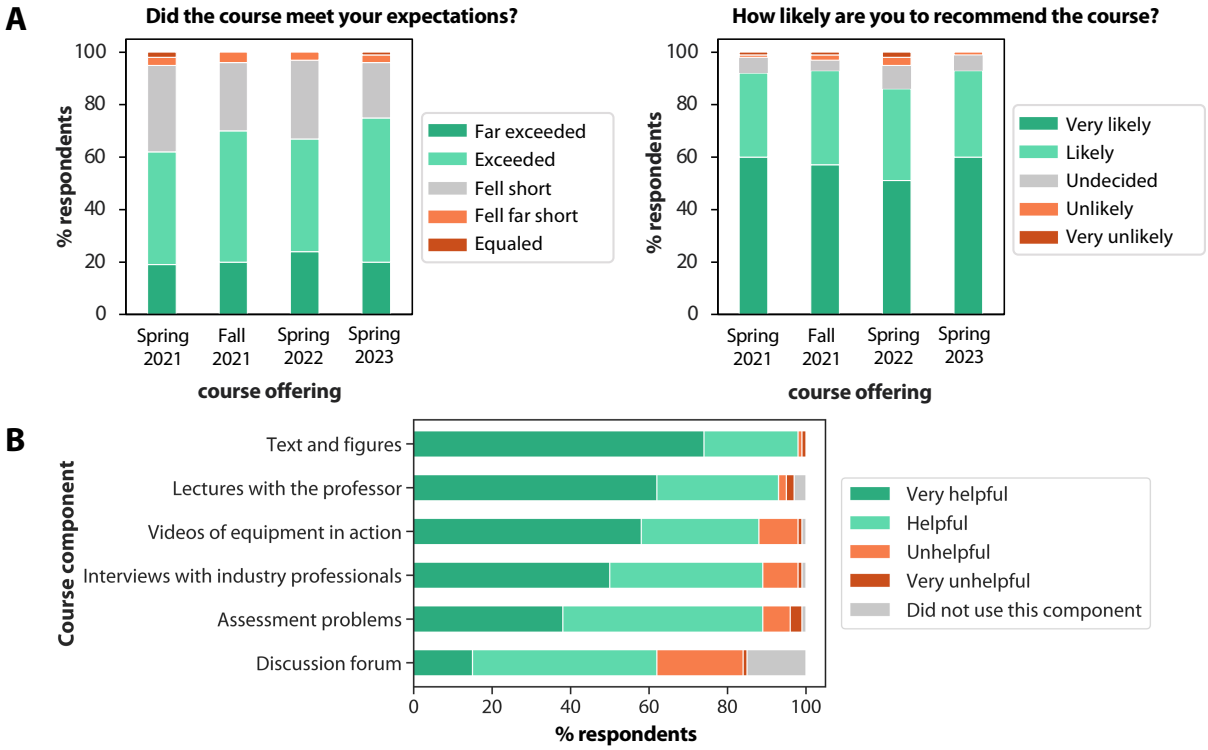

Figure 3. Summary of exit survey responses across all four course offerings, including (A) responses to "Did the course meet your expectations?" and "How likely are you to recommend the course?", (B) ratings of the perceived helpfulness of each course component.

To gather more detailed feedback about how to improve each course component, we collected qualitative data from an open-ended survey question "What could be improved about the course?". Two co-authors (MY and FJK) read through the survey responses from the Spring 2021 course offering and used an inductive coding approach to identify emergent themes in the responses[12]. Then, MY and FJK independently coded the remaining survey responses according to those themes. The inter-reliability[13] between MY and FJK was 93%. The most common feedback categories aggregated across all four course offerings are summarized in **Table 3**.

Table 3. Summary of learner responses to "What could be improved about the course?"

Theme	Example(s)	% of respondents
Clearer assessment questions	*"Ensure that the skill drill questions align more closely with the material in the section."*	23

	"Math problems were an important part of some of the problem sets, yet the math was given only a cursory notice in the text."	
More technical details about the equipment and/or manufacturing process	*"Include more details about instruments, interfaces, and data flows"* *"Add more technical content on what aspects of the manufacturing process could affect the efficacy (of the therapy)"*	16
More videos instead of text	*"The final unit was too textual and abstract for me. It would have helped if the team gave more videos/animations."* *"Animation to demonstrate the internal flow of work (of the equipment)"*	15
Greater use of discussion forum	*"Give more incentives for students to actively participate in discussion forums."*	8
Provide repository of downloadable media (slides/figures/text)	*"Provide the slide decks and diagrams used within the presentations for viewers."*	8

The most common suggestion for how to improve the course was to increase the clarity of the assessment questions, highlighted by 23% of survey respondents. Of these, 21% of the respondents highlighted the math problems as being particular sources of difficulty, with one learner stating *"Math problems were an important part of some of the problem sets, yet the math was given only a cursory notice in the text."* In future offerings of the course, we will endeavor to provide more worked examples of math-intensive problems, in addition to increasing the scaffolding provided in the questions themselves.

The second most common suggestion was to provide more technical details about the equipment and manufacturing process. For example, one learner suggested including more specific details about how unit operations were automated. Another stated "*I would have liked to have seen more process equipment in operation larger than the product development scale.*" Since one of the distinguishing factors of our course is the direct insight into the manufacturing process, it was reassuring that respondents in fact requested more technical details and videos of equipment in action.

The third most common suggestion was to provide more video resources instead of text. Even though respondents indicated that text resources were helpful (**Fig. 3B**), one

learner stated *"I would like to see more actual lecture sessions with a speaker discussing the diagrams."* Other respondents echoed this feedback, specifically pointing towards the final unit of the course (regulation of cell therapy manufacturing) as potentially benefiting from more videos. One learner wrote *"As someone with dyslexia, it's sometimes really hard for me to read crammed up paragraph after paragraph. In Unit 6, for instance, the last 2 chapters felt so rushed due to the much more crowded writings."* These results speak to the importance of balancing the ratio of text to video resources in the course.

Finally, in the first offering of the course, we received feedback that the course timeline was too inflexible. For example, one learner stated *"Don't make this course so time bound. Provide more flexibility, especially to working adults with families/other commitments."* Therefore, we increased the duration of subsequent course offerings from 6 weeks to 9 weeks, and we also changed the course to self-paced. We made this change starting with the second offering, in Fall 2021, of the course. As shown previously in **Fig. 3**, introducing this change did not lead to significant changes in learner satisfaction as measured by the exit survey. Furthermore, changing to a self-paced structure did not significantly change course completion rates. **Table 4** shows the total number of enrolled learners per course offering, the number of verified learners (learners who pay a fee for formal certification of course completion), and certified learners (subset of verified learners who actually completed the course and passed with an >80% grade). We measured completion rate as the number of verified learners who were certified; this calculation deliberately excluded non-verified learners, because they did not have access to the final problem set and therefore could not attain a passing grade. In all four offerings, there was a bimodal grade distribution for verified learners, where the majority of learners attained the passing grade (>80%), and a minority of learners interacted minimally with the course assignments and scored near zero (**Supplemental Fig. 1**). Notably, we did observe a change in qualitative survey responses after changing the course from instructor-paced to self-paced. Starting with the Fall 2021 course onwards, we no longer received requests from learners for more time or flexibility, suggesting they were satisfied with the course timeline.

Table 4. Number of enrolled, verified, and certified learners per course offering

Course offering	Enrolled learners	Verified learners (% of total enrolled)	Learner completion rate (% of verified learners who are certified)
Spring 2021	2,825	153 (5.4%)	107 (69.9%)
Fall 2021	2,575	309 (12.0%)	232 (75.1%)
Spring 2022	2,462	177 (7.2%)	108 (61.0%)
Spring 2023	3,468	229 (6.6%)	150 (65.5%)

Finally, we asked learners an open-ended question "How will this course impact your future?". As before, MY and FJK read through the Spring 2021 responses, identified common themes, and independently coded the 2021 and 2022 survey responses according to those themes. The inter-reliability between MY and FJK was 94%. The responses fell into two major categories, summarized in **Table 5**. 40% of respondents indicated that the course would help them transition into the cell therapy industry and broaden their career opportunities. One stated "*Thanks to this course, I could choose the area I want to follow. Before, although I knew what I wanted to do, I did not know how to reach that goal. So, now I know what I have to do.*" In addition, 29% of respondents indicated that the course helped them gain knowledge that was directly relevant to their current job positions. For example, one learner stated "*I'm a professional validation engineer who works for clients on their projects. I understand the equipment more than the microbiology. This course gave me a better appreciation for the products for some of my clients. It was also meaningful to understand the science in this time of COVID vaccines, cancer treatments and tissue generation.*" Another learner said *"I am a manufacturing finance director… I will now be able to engage in conversation with the manufacturing and quality functions at a higher degree of technical understanding."* This sentiment was echoed by several learners who were working in non-R&D roles who felt that they now had greater fluency to communicate with their R&D colleagues. Finally, a minority of respondents specifically described how the course would be helpful for onboarding new employees in their workplace. Several respondents mentioned that they worked in companies that were opening cell therapy manufacturing facilities in the near future, and that the course would be helpful for training and collaborating with future colleagues.

Table 5. Summary of learner responses to "How will this course impact your future?"

Theme	Example(s)	% of respondents
Help enter the cell therapy industry and broaden access to career opportunities	*"Thanks to this course, I could choose the area I want to follow. Before, although I knew what I wanted to do, I did not know how to reach that goal. So, now I know what I have to do."* *"I am interviewing for a position directly related to the course material… so I feel more comfortable seeing the position as a way to begin a career in manufacturing."*	40
Gain new knowledge that is relevant to existing job	*"My company is making a cell therapy product. My team will conduct process validation for it. This course directly informed work I will do in the next 12-24 months."*	29

	"The course allowed me to be conversant with Process Development colleagues on a current cell therapy project we are working on."	
Help onboard new employees in current workplace	*"Help onboard new employees with no cell therapy experience"* *"My company is working to start a cell therapy manufacturing facility… I will be able to have intellectual conversations with future colleagues in the cell therapy workgroup."*	5

Conclusion

We designed and implemented an online course on the principles and practice of cell therapy manufacturing, collectively reaching over 10,000 learners as of September 2023. Survey respondents were generally satisfied that the course met their learning goals, and 90% of exit survey respondents indicated that they were 'very likely' or 'likely' to recommend the class to a peer. Many respondents indicated that this course would support their career goals of pivoting into the cell therapy industry, or support their existing job in the cell therapy space.

One of the key lessons learned from running the course was to provide space for student feedback, interwoven throughout the technical content. This allowed us to adapt the course structure and content in response to feedback. For example, we added a discussion forum link to every content page (text and video), and included a feedback forum page at the end of each unit for learners to highlight their 'muddiest points' (most confusing segments). When learners highlighted a text section as being confusing or ambiguously worded, we edited the text and/or illustrations to increase clarity for subsequent iterations. For example, in the first course offering, some learners expressed confusion about viral vectors, in particular the difference between recombinant viral vectors and wildtype viruses. Therefore, we adapted the text in subsequent offerings to explicitly delineate sections that described wildtype viruses from sections that explained recombinant vectors. We are continuing to review and iteratively hone the course in response to current feedback, including increasing the clarity of assessment questions and providing even more technical details about the manufacturing process and equipment used.

Finally, this course development experience highlighted the value of collaboration between universities and industry in developing training programs. For readers considering establishing a similar partnership, there are some important practical considerations for creating educational materials while protecting company proprietary information. For example, we solicited permission to film onsite at each company, and all video footage underwent legal review before being published. Ultimately, this collaboration proved

fruitful, and survey respondents appreciated the industry perspectives that were interwoven throughout the course. In conclusion, we believe that this course can serve as a model for how collaboration between industry and academia can enable the creation of scalable courses to support the training of industry professionals and meet modern healthcare needs.

Acknowledgements

The authors gratefully acknowledge partial funding from National Institute for Innovation in Manufacturing Biopharmaceuticals (NIIMBL), the Hugh Hampton Young Memorial Fellowship (MY), the Michael (1949) and Sonja Koerner Professorship (KJVV). The authors sincerely appreciate contributions by the 66 beta-testers of early versions of this material, including Chris Bellerive and Floyd Brownewell, cell therapy manufacturing experts interviewed within the video content of the course, including Greg Russotti, Chesney Michels, Geoff Hodge, Rachel Yao, Chris Parrish, and Mike Halpin. KJVV and PB also acknowledge the undergraduate student researchers who contributed to the early drafting of the course concept: Brian Williams while a student at MIT and Claire Siege as a summer research assistant at MIT while enrolled at Wellesley College; Talia Wolfson as a summer research assistant at MIT while enrolled at Oberlin College and then as an MIT post-bachelor's research assistant. Finally, the authors are grateful to the many learners who participated in the course and completed the pre- and post-course surveys.

References

1. Huang, R. *et al.* Recent advances in CAR-T cell engineering. *J. Hematol. Oncol.* **13**, 1–19 (2020).
2. Hulme, C. H. *et al.* Cell therapy for cartilage repair. *Emerg. Top. Life Sci.* **5**, 575–589 (2021).
3. Leclerc, T. *et al.* Cell therapy of burns. *Cell Prolif.* **44**, 48–54 (2011).
4. Mount, N. M., Ward, S. J., Kefalas, P. & Hyllner, J. Cell-based therapy technology classifications and translational challenges. *Philos. Trans. R. Soc. B Biol. Sci.* **370**, 20150017 (2015).
5. Gottipamula, S., Bhat, S. & Seetharam, R. N. Mesenchymal Stromal Cells: Basics, Classification, and Clinical Applications. *J. Stem Cells* **13**, (2018).
6. Wang, L. L. W. *et al.* Cell therapies in the clinic. *Bioeng. Transl. Med.* **6**, (2021).
7. Ho, L. D., Robbins, H. L. & Levine, A. D. Assessing workforce needs for the emerging CAR-T cell therapy industry. *Nat. Biotechnol.* **40**, 275–280 (2022).
8. De Freitas, S. I., Morgan, J. & Gibson, D. Will MOOCs transform learning and teaching in higher education? Engagement and course retention in online learning provision. *Br. J. Educ. Technol.* **46**, 455–471 (2015).
9. Bloom, B., Engelhart, M. D., Furst, E. J., Hill, W. H. & Krathwohl, D. R. *Taxonomy of Educational Objectives*. *Longmans* (1956). doi:10.1300/J104v03n01_03.
10. Anderson, L. W. *et al. A Taxonomy For Learning, Teaching, And Assessing: A Revision of Bloom's Taxonomy of Educational Objectives*. (2001).
11. Frye, A. W. & Hemmer, P. A. Program evaluation models and related theories: AMEE

Guide No. 67. *Med. Teach.* **34**, (2012).
12. Thomas, D. R. A General Inductive Approach for Analyzing Qualitative Evaluation Data. *Am. J. Eval.* **27**, 237–246 (2006).
13. Stemler, S. E. A comparison of consensus, consistency, and measurement approaches to estimating interrater reliability. *Pract. Assessment, Res. Eval.* **9**, (2004).